University of Bergen

Department of Physics and Technology

Master thesis in

Ocean Technology

Bending moments and collision loads between a floating offshore wind turbine and a supporting barge

Thomas Skinlo Høyven

June 2019

Preface and acknowledgements

This thesis is submitted as partial fulfilment of the requirements for the master's degree in Ocean Technology. The work was carried out at the Department of Physics and Technology at the University of Bergen, and at the Department of Mechanical and Marine Engineering at the Western Norway University of Applied Sciences. The work was done in collaboration with Equinor.

My sincere thanks to my supervisor, David Roger Lande-Sudall, for guidance and support throughout the project. I would also like to express my gratitude to my external supervisor from Equinor, Gudmund Per Olsen, for the constructive meetings, input and time devoted to the project.

Thanks to professor Bjørn Tore Hjertaker and Irlin Nyland, at the University of Bergen, for help and support throughout the master's degree.

Thanks to Thore Clifford Thuestad, Kjell Agnar Herfjord and Gloria Stenfelt. I am truly grateful for their guidance and expertise in hydrodynamics, mechanics and the maritime industry.

Thanks to Bernt Hustad Hembre, Kjetil Gravelsæter, Harald Moen, Nafez Ardenstani, Frode Weber Jansen and Sergio Victor Martinez Castro for their assistance and support during the building of the experimental models.

Thanks to Western Norway University of Applied Sciences for the access to material resources, machinery and the MarinLab.

Thanks to Equinor for having financially supported the master project generously.

Finally, thanks to my fellow students for help and support, to my family and friends for support and encouragement, and to my son, Trym Ørjansen Skinlo, for his patience throughout my studies.

This page is intentionally left blank.

Abstract

A challenge with an offshore wind turbine using a floating spar-buoy foundation is the availability of a suitable inshore assembly location as the spar-buoy is constrained by its deep draft. The purpose of this thesis is to investigate a method which reduces the spar-buoy draft by using a barge to support and maintain the stability of the floating offshore wind turbine during the installation. Critical aspects such as the bending moment and collision loads after separation between the two floating bodies are measured in a model scale experiment performed in a wave-tank.

The two models are designed and constructed in a 1:72 scale to represent the full-scale structures. A load cell rig, consisting of two load cells, is constructed to measure the loads caused by wave loading between the two models. The load cell rig also includes two electromagnets programed to release the floating offshore wind turbine in specified phases in the wave profile.

Three main experiments are executed, where the first two are performed with the two models connected to investigate the bending moment between the bodies in a fully drafted and a reduced draft case. This is done using a JONSWAP wave spectra with two different wave heights and four different wave periods, allowing for a comparison of the load magnitudes in the different sea-states and for the two cases. The third experiment is performed with a release of the floating offshore wind turbine to investigate the collision loads after separation. This experiment is performed using regular waves with one wave height and three different wave periods, allowing an investigation of the difference in impact magnitude and time of occurrence due to the release in the different phases.

The bending moments and the largest impact loads are scaled up to full-scale magnitudes using the relevant Froude scaling relationship, giving an indication of the magnitude the full-scale structures may be exposed due to the wave loads in the investigated sea-states.

The results from the first two experiments shows an increasing bending moment when both wave period and wave height are increased. Further, that the fully drafted case is more exposed at the shortest and longest wave period and the reduced draft case is most exposed in the wave periods in between. From the collision experiment, the results show that the impact loads also increase with increased wave periods and that there is no matching release phase which correspond as the best suited for all wave periods tested.

The results are presented in representable plots and tables before they are discussed and compared between relevant experiments. The thesis closes with a conclusion and suggestions for further work.

This page is intentionally left blank.

Sammendrag

En utfordring med en offshore vind turbin som bruker et flytende sparbøyefundament, er tilgjengeligheten av egnede innaskjærs sammensettings lokasjoner ettersom sparbøyefundamentet har begrensninger på grunn av den store dypgangen. Formålet med denne oppgaven er å undersøke en metode som reduserer fundamentets dypgang ved a benytte en lekter til å støtte og opprettholde stabiliteten til den flytende vind turbinen under installasjonen. Kritiske aspekter som bøyemoment og kollisjonslaster etter seperasjon mellom de to flytende legemene blir målt i et modellskala eksperiment i en bølgetank.

Modellene er modellert og bygget i en 1:72 skala for å representere de fullskala konstruksjonene. En lastcelle rigg, bestående av to lastceller, er bygget for å måle kreftene forårsaket av bølgelastene mellom de to modellene. Lastcelle riggen inkluderer også to elektromagneter som er programmert til å slippe den flytende turbin modellen i en gitt bølgefase.

Tre hoved eksperimenter er utført, hvor de første to er utført med de to modellene sammenkoblet, for å undersøke bøyemomentet som oppstår mellom disse når turbinen har sin opprinnelige dypgang og når dypgangen er redusert. Dette er gjort i bølger med et JONSWAP bølgespekter med to forskjellige bølgehøyder og fire forskjellige bølgeperioder, noe som gjør det mulig å sammenligne last størrelsene i de forskjellige sjøtilstandene for de to situasjonene. Det tredje eksperimentet er utført med et slipp av turbinen for å undersøke kollisjonslastene etter seperasjonen. Dette eksperimentet er utført i regulære sinusbølger med en bølgehøyde og tre bølgeperioder, slik at en undersøkelse av forskjellen i slagstyrke og kollisjonstidspunktet grunnet slippet i de forskjellige fasene kan undersøkes.

Bøyemomentene og de største kollisjonslastene er skalert opp til fullskala størrelser ved hjelp av de relevante Froude skaleringsforholdene, noe som gir en indikasjon på last størrelsene en fullskala konstruksjon kan bli utsatt for på grunn av bølgelastene i de undersøkte sjøtilstandene.

Resultatene fra de to første eksperimentene viser at bøyemomentet øker når både bølgeperioden og bølgehøyden øker. Videre, at forsøket med den opprinnelige dypgangen er mer utsatt i bølger med de korteste og lengste bølgeperiodene, og at forsøket hvor dypgangen er redusert blir mest utsatt i bølgeperiodene imellom. Fra kollisjonseksperimentet viser resultatene at kollisjonslastene også øker når bølgeperioden øker, og at det ikke er noen slipp faser som er like og som korresponderer som den best passende slippfasen for de forskjellige forsøkene.

Resultatene er presentert i representative grafer og tabeller før de blir diskutert og sammenlignet mellom de relevante forsøkene. Avhandlingen avslutter med en konklusjon og forsag for videre arbeid.

This page is intentionally left blank.

List of Contents

List of Tables

List of Figures

List of Abbreviations

Symbols	Description
FOWTs	Floating Offshore Wind Turbines
FOWT	Floating Offshore Wind Turbine
RAO	Response Amplitude Operators
DOF	Degrees of Freedom
6DOF	Six Degrees of Freedom
COG	Centre of Gravity
COB	Centre of Buoyancy
PM	Pierson-Moskowitz
JONSWAP	Joint North Sea Wave Project
ULC	Upper Load Cell
LLC	Lower Load Cell
SST	Total Sum of Squares
SSE	Sum of Squares Error
RMSE	Root Mean Square Error

1. Introduction

1.1. Background and motivation

Offshore wind has recently become one of the fastest growing forms of renewable energy installed globally. The remarkable growth has led to a global installed capacity of more than 19 GW by 2017, up from 1 GW in 2006 [1]. This shows that the renewable offshore wind industry plays an important role as a sustainable energy production system.

Many interesting wind harnessing concepts have been and are being tried out offshore, e.g. airborne kites or vertical-axis turbines [2]. The majority of the installed wind generators however, are the conventional horizontal-axis bottom fixed wind turbines. These turbines are constrained by the water depth and are typical limited to depths up to 50 meters [3]. This limits the locations suitable for bottom fixed constructions as close to 80 percent of the global offshore wind resource potential is in deeper waters [4]. Floating Offshore Wind Turbines (FOWTs) may be a game changer, opening up significant new markets in deep waters.

As of 2019, there is only one existing offshore wind farm using FOWTs; Equinor's, Hywind Scotland Pilot Park, located at Buchan Deep at the east coast of Scotland and installed late 2017. The park consists of five 6 MW Siemens wind turbines, installed upon floating spar-buoy substructures which are anchored to the sea bed. A spar-buoy uses a simple design, consisting of a deep drafted cylinder with a low water plane area which is ballasted to keep the center of gravity (COG) bellow the center of buoyancy (COB) for stability.

One of the biggest advantages with a Floating Offshore Wind Turbine (FOWT) is the possibility for inshore, onshore or quayside assembly of the complete construction. This may lead to a less expensive installation cost compared with the bottom fixed wind turbines, which are assembled and installed offshore at their production site. Of the different FOWT designs, there are three main concepts for floating foundations which are the spar-buoy, the semi-submersible and the tension leg platform. The two latter allows for quayside assembly, which are a big advantage as onshore cranes can be used. The spar-buoy however, is constrained by its deep draft and may, due to this, only be assembled at locations with deep enough waters. The transit route to the production site also needs to be deep enough. This is one of the big challenges when using a spar-buoy substructure as the floating foundation, as illustrated in Figure 1.

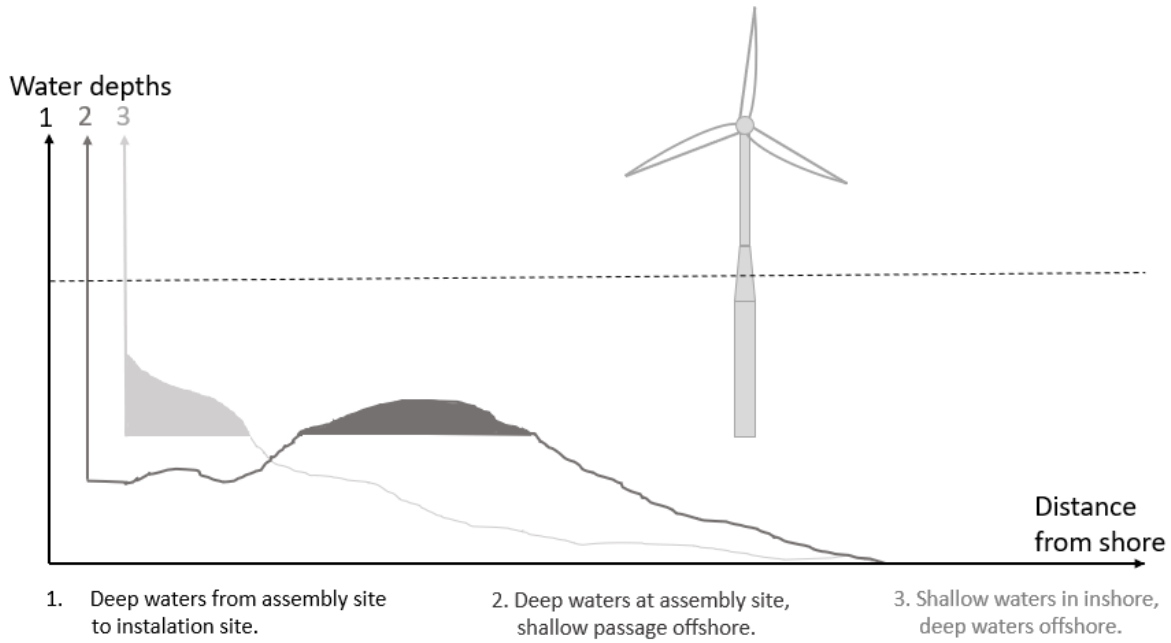

Figure 1 - Illustration of the different challenges regarding water depth at different locations.

If FOWTs are going to be widely used in the offshore wind industry, the need for industrialized installation and assembly methods are needed. Different methods for installation and assembly of FOWTs on spar-buoy foundations have been proposed. One of these methods is the Atkins transportation frame concept [5]. A concept that uses a reusable transportation frame where four FOWTs are attached and transported simultaneously as shown in Figure 2.

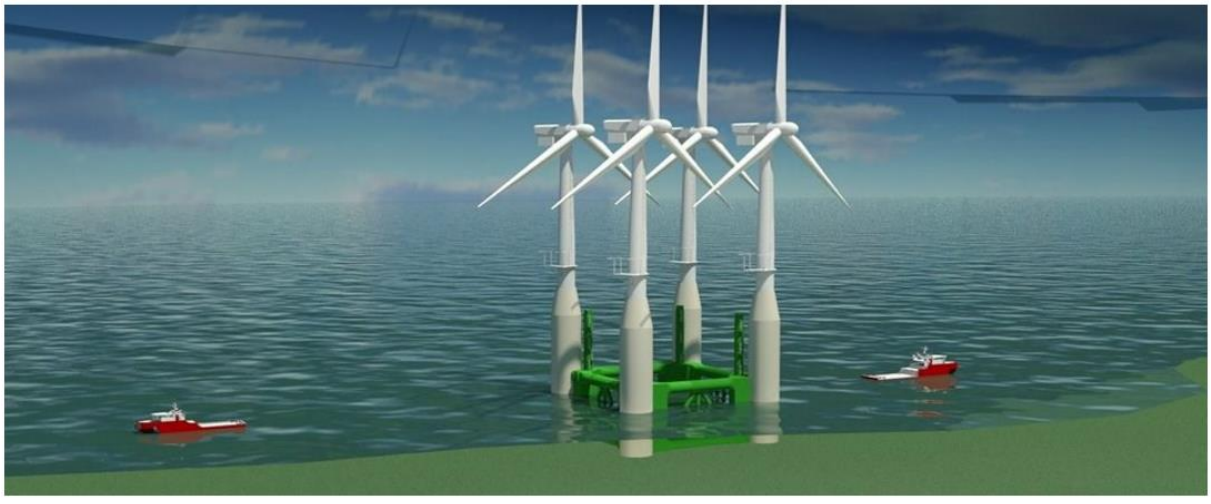

Figure 2 - The Atkins reusable transportation frame, allowing for multiple turbine transportation at reduced draft [5].

This method has the potential to reduce the spar-buoy draft as stability is increased when the four FOWTs are attached to the transport frame and together function as a semi-submersible vessel.

Inspired by the above-mentioned concept, this thesis will investigate a similar method as illustrated in Figure 3, but where a barge is used to support the spar-buoy foundation at a reduced draft when the turbine is being installed upon it. This project will be restricted to a case where only one FOWT is used, as illustrated to the left in Figure 3, to reduce the complexity of the experiment. The draft reduction advantage will still be present however, the stability may be reduced compared to when multiple turbines are used.

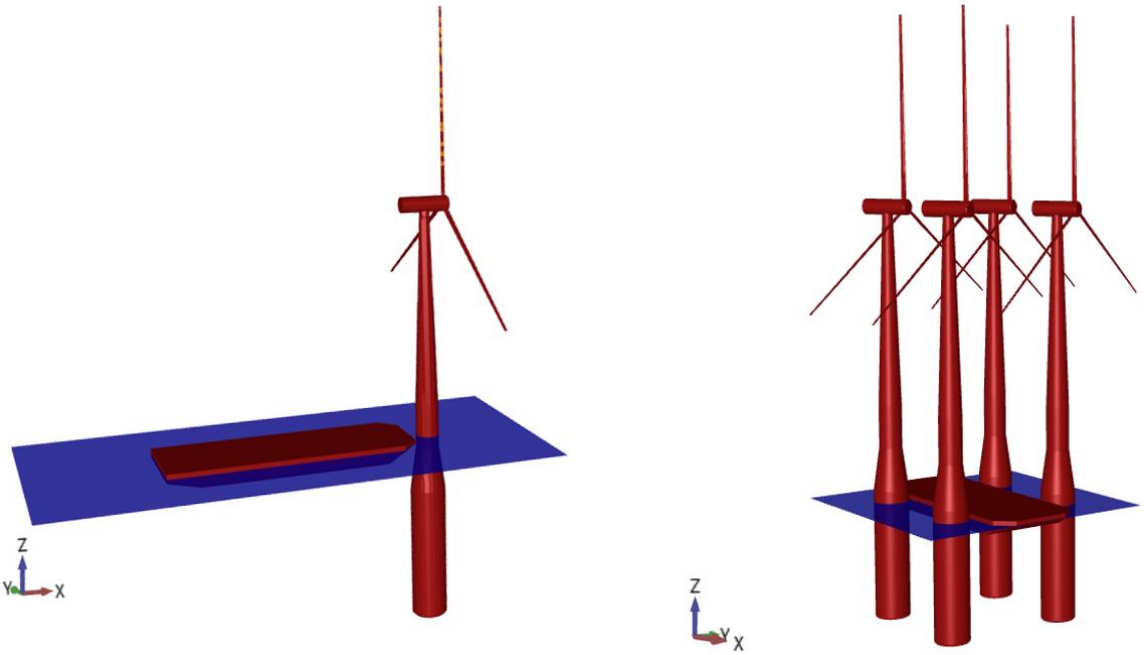

Figure 3 - Screen shot from HydroD, showing a barge being used as a support for one FOWT to the left in the figure and for four FOWTs to the right in the figure, giving an illustration of the method. The interface between the two bodies is not included in the illustration as the thesis only focus on the loads between the bodies and not the design of the support structure.

By ballasting the substructure with liquid ballast later, a potential of approximately 30 percent draft reduction is calculated, opening up for assembly at locations with more shallow waters and maybe even quayside assembly.

A qualitative risk assessment of the procedures of this method was executed with the conclusion that the biggest uncertainties and the most significant risks with this method are:

- The loads between the FOWT and the barge in a connected state, due to the hydrodynamic forces in the given sea-states, when the FOWT is at reduced draft and when it is fully drafted.
- The possible collision loads between the FOWT and the vessel in the instances before/after attaching/detaching of the two.

Hence, the motivation and aims for this master project is to investigate the bending moments between a model scaled FOWT and a model scaled barge at reduced draft and fully drafted when the two

floating bodies are in a connected state and exposed to waves. Further, to investigate the possible impact loads between the two constructions in the instance after separation. This may give an indication as to which loads might be expected between the two floating bodies, and whether this method for installation may be a suitable solution for future FOWTs assemblies where a spar-buoy is used as foundation.

1.2. Existing installation methods

The conventional installation methods used by the offshore wind industry today, for bottom fixed offshore wind turbines, usually includes a jack-up vessel or a floating crane vessel. The foundation is first driven into the seabed by a hydraulic hammer, or by using pressure difference and weight as with a suction bucket. Further, a transition piece is either grouted or bolted onto the foundation before the tower, nacelle, hub and the blades are installed. The different installation vessels may have the capacity to carry and install multiple turbines each trip if the foundations are already installed.

The bottom fixed turbines are, as mentioned above, partly assembled and installed offshore at the wind farm site and hence, the installation processes are significantly influenced by the environmental conditions. The installation vessels have restrictions concerning wave heights, wind speed and ocean currents which may influence offshore operations. However, when a jack-up rig has its legs firmly down, and the foundation is in place, hydrodynamic forces are of a less concern compared to when it is floating.

With the FOWTs, only a few installations have yet been performed globally. This includes a couple of prototypes, such as the 2.3 MW Hywind Demo and the 2.0 MW WindFloat prototype in addition to the installation of the five, 6 MW Hywind Scotland wind turbines.

The Hywind demo was assembled at an inshore location where the spar-buoy substructure first was towed in a horizontal position before it was upended and ballasted using a small barge with a crane. Further, another slightly bigger barge with a crane, installed the tower in segments before it installed the nacelle, the hub and the blades. Finally, the complete FOWT was towed, in a vertical position, to the installation site and hooked up to the moorings [6].

The WindFloat prototype was completely assembled and commissioned at quayside before it was towed about 400 kilometers and hooked up to its moorings at the installation site [7]. The assembly was performed in a drydock and with the use of onshore cranes, making it much more accessible than the Hywind solution. This could be done mainly because of its relatively shallow drafted semi-submersible foundation. It should be noted that even though the assembly and installation is less

complicated when using the semi-submersible foundation, the foundation itself is a much more complex structure than the spar-buoy foundation.

The larger Hywind Scotland FOWTs were also assembled at an inshore location. The spar-buoy substructures were transported in a horizontal position in pairs with an offshore heavy transport ship before they were upended and ballasted. The turbines were fully assembled and commissioned onshore using a mobile onshore crane before they were picked up by the semi-submersible crane vessel, Saipem 7000. The semi-submersible crane vessel then carried the fully assembled turbines over to the substructures before they were connected, as shown in Figure 4. The fully assembled FOWTs were then towed to the installation site and hooked up to their moorings.

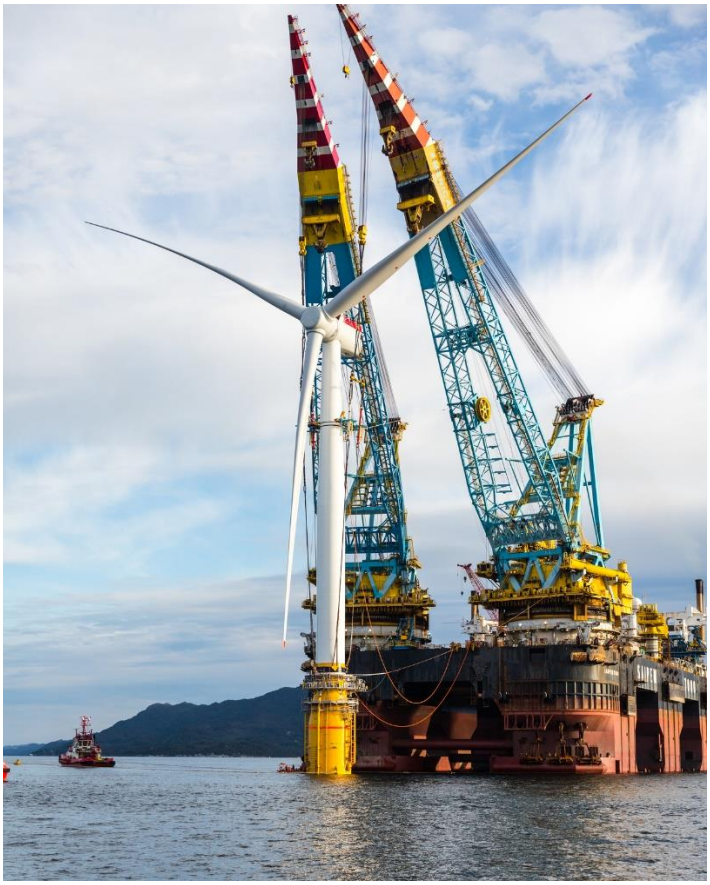

Figure 4 - Mating of Hywind Scotland wind turbine. Photo by Ørjan Richardsen / Woldcam - Equinor [8]

The use of the semi-submersible crane vessels such as Saipem 7000, or similar vessels, may be a challenge for assembly of the FOWT if the floating turbine concept is to be industrialized. When a great number of FOWTs are to be assembled, these large crane vessels will become even less accessible and their already high rates would increase even further, without new equivalent vessels being manufactured to meet this demand.

The proposed method may prove to be a solution to the challenge at hand, and especially if it opens for quayside assembly.

Even though the presented method and the experiments performed in this thesis focus on the installation aspects of a FOWT using a spar buoy floater, the method may also be considered for both maintenance and decommissioning operations. For the maintenance aspect, the barge could be used as a platform for equipment, parts and tools with a close accessibility if the two were connected. For the decommissioning aspect, the method could also be considered when bottom fixed wind turbines using monopile foundations are being decommissioned. When the monopile foundation is cut at the sea bottom, it has much the same geometry as the FOWT with the spar buoy substructure and hence, might act similar as in the experiment performed in this paper.

1.3. Objectives

The objective of this thesis is to design, build and perform an experiment in the wave tank of the MarinLab at the Western University of Applied Sciences, where bending moments and collision loads between a model scaled FOWT and a model scaled barge are investigated.

First, the scaled models for the experiment will be designed, modeled and built to represent the full-scale structures as far as possible. The modeling will be done in the 3D software tools SESAM and Creo Parametric which will help obtaining important parameters such as COG of the scaled models as similar to the full-scale structures as possible, and which will help getting the physical models ballasted and stabilised correctly. In SESAM, the RAO's of the combined system will also be investigated in the relevant degrees of freedom.

Further, a load cell rig will be built where two load cells will measure the bending moments and the collision loads between the two floating objects in fully developed waves in different sea-states. In the collision experiment, the model scaled FOWT will be released in different phases in a sea-state using regular sine waves to investigate the impact differences and if there is an indication as to which phase is better suited for release.

Different MATLAB scripts will be developed to present the measured data in representable plots to illustrate their magnitudes. The magnitudes of the loads will finally be scaled up to full-scale magnitudes, using relevant scaling laws, to give an indication of which magnitudes are to be expected in a full-scale situation.

1.4. Outline

The thesis starts with a brief introduction of the offshore wind industry, about the existing installation methods and the challenges ahead concerning installations of floating offshore wind turbines before the objective of the thesis is presented.

Chapter 2 follows up with the theories used in the project for building the experimental models and measurement system and the background for the mathematical simulations and calculations performed. Chapter 3 presents the facility and the apparatus used to perform the experiment and the numerical calculations and analysis.

In Chapter 4, the method for modeling and building the experimental models and the measurement system used to measure the loads are presented. Further, the experimental setup and the calibration of the systems are presented before the experimental execution procedures are described.

Chapter 5 follows up with a presentation of the experimental results obtained from the experiments plotted in graphs and tables before each experiment is discussed. Further, the corresponding experiments are compared and discussed.

Chapter 6 summarises and presents the conclusion from the achievements of the thesis.

Finally, Chapter 7 and Chapter 8 describes suggestions for further work and the error sources found respectively.

2. Theory

In this chapter different theories which are used in the experiments and the calculations performed are presented. This includes laws of scaling, hydrodynamics, system response and statistics, amongst other.

2.1. Scaling

Dimensionless numbers, such as the Froude number or Reynolds number, can be used to correlate measurements made on small physical models to equivalent values for full-scale structures, allowing experiments to be carried out relatively inexpensive on small scale models [9].

Experiments performed with physical models requires some form of similarity between the full-scale structure and the model, such as:

- Geometric similarity: The model must have physical dimensions which are uniformly proportional to those of the full-scale structure.
- Kinematic similarity: Velocities in the model must be proportional to those used for the full-scale structure.
- Dynamic similarity: Forces and accelerations in the model must be proportional to those of the full-scale structure.

These similarities require that all location vectors, velocity vectors and force vectors in the coincident coordinates of the scaled model and the full-scale structure have the same directions and that the magnitude of these vectors must relate to each other in a constant proportion.

When a free surface of a liquid is involved, gravity forces becomes important, which is true whenever a water surface or waves are present. Inertia forces and pressure forces are nearly universally important, making it appropriate to keep the ratio of inertia or pressure forces divided by gravity forces the same in the scaled model as in the full-scale structure. The square root of this ratio gives the Froude scaling, or the Froude number given as Eqn. (1):

$$F_n = \sqrt{\frac{F_I}{F_G}} = \sqrt{\frac{\rho \cdot l^2 \cdot v^2}{\rho \cdot g \cdot l^3}} = \frac{v}{\sqrt{g \cdot l}} \tag{1}$$

where F_n is the dimensionless Froude number, F_I and F_G are the inertia forces and the gravity forces respectively, ρ is the fluid density, l is the length of the vessel, v is the relative velocity between the vessel and the fluid, and g is the gravity. Keeping the F_n value equal for both the full-scale structure (subscript F) and the scaled model (subscript M), leads to the Froude scaling law as shown in Eqn. (2):

$$\frac{v_F}{\sqrt{g \cdot l_F}} = \frac{v_M}{\sqrt{g \cdot l_M}} => v_F = v_M \cdot \sqrt{\frac{l_F}{l_M}} = v_M \cdot \sqrt{\lambda} \tag{2}$$

where $\frac{l_F}{l_M}$ is the ratio between the length of the scaled model and the length of the full-scaled structure giving the dimensionless scaling factor λ.

The Reynolds number is the ratio between the inertia force and the viscous force as shown in Eqn. (3):

$$R_n = \frac{F_I}{F_V} = \frac{\rho \cdot l^2 \cdot v^2}{\mu \cdot v \cdot l} = \frac{\rho \cdot l \cdot v}{\mu} \tag{3}$$

where R_n is the dimensionless Reynolds number, F_V is the viscous force and μ is the dynamic viscosity. Keeping the R_n value equal for both the full-scale structure and the scaled model leads to the Reynolds scaling law as shown in Eqn. (4):

$$\frac{\rho_F \cdot l_F \cdot v_F}{\mu_F} = \frac{\rho_M \cdot l_M \cdot v_M}{\mu_M} => v_F = v_M \cdot \frac{l_M}{l_F} \cdot \frac{\rho_M}{\rho_F} \cdot \frac{\mu_F}{\mu_M} = v_M \cdot \frac{1}{\lambda} \cdot \frac{\rho_M}{\rho_F} \cdot \frac{\mu_F}{\mu_M} \tag{4}$$

Eqn. (2) and Eqn. (4) cannot simultaneously be satisfied, hence a model test with proper relationship between inertia, gravity and viscous forces are impossible to accomplish [10]. Due to this, using the Froude scaling law as is done in this project, might not give the accurate effect from the viscous forces.

Table 1 shows the Froude scale relationship for different parameters between the full-scale structure and the scaled model derived from Eqn. (2), where λ is the scaling factor.

Table 1 - Froude scaling relationship between full-scale structure and the scaled model with λ used as the scaling factor.

Parameter	Unit	Relationship
Length	[m]	$l_F = \lambda \cdot l_M$
Area	[m^2]	$A_F = \lambda^2 \cdot A_M$
Volume	[m^3]	$\nabla_F = \lambda^3 \cdot \nabla_M$
Structural mass	[kg]	$m_F = \lambda^3 \cdot m_M \cdot \frac{\rho_F}{\rho_M}$
Time	[s]	$t_F = \sqrt{\lambda} \cdot t_M$
Velocity	[m/s]	$v_F = \sqrt{\lambda} \cdot v_M$
Acceleration	[m/s^2]	$a_F = a_M$
Force	[N]	$F_F = \lambda^3 \cdot F_M \cdot \frac{\rho_F}{\rho_M}$
Energy	[J]	$E_F = \lambda^4 \cdot E_M \cdot \frac{\rho_F}{\rho_M}$

It should be noted that it is challenging to scale down all the full-scale structure properties, e.g. wall thickness, as manufacturing and strength requirements of the scaled model must be taken into consideration. Also, different materials are often used in the scaled models, hence, it is almost impossible to fulfil all scaling requirements when a model scale structure is built.

2.2. Linear wave theory and regular waves

The simplest wave theory is obtained by taking the wave height to be much smaller than both the wave length and the water depth. This theory is referred to as linear wave theory. For regular linear waves the wave crest height is equal to the wave trough height and is denoted the wave amplitude, hence $H = 2\zeta_a$ [11], where H is the wave height and ζ_a is the amplitude.

A regular, or harmonic wave may be described as a continuous sine wave with constant periodic oscillations as illustrated in Figure 5.

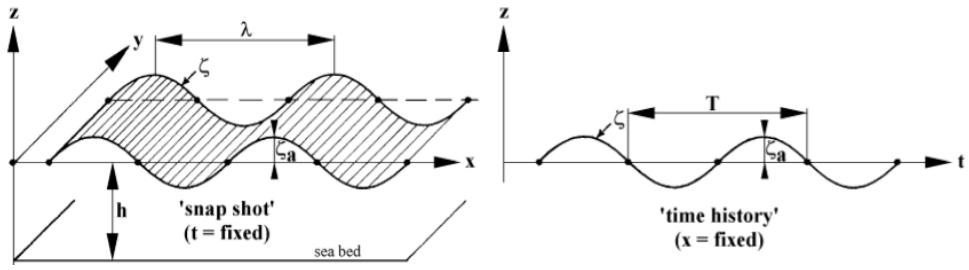

Figure 5 - Illustration of a regular wave from two different perspectives. The left side shows the wave profile as a function of distance at a fixed instant in time. The right side shows a wave profile as a function of time at where the wave propagation distance x is fixed [9].

Moving in the positive x-direction, a regular wave has a wave profile which can be expressed as shown in Eqn. (5):

$$\zeta = \zeta_a \sin(\omega t - kx) \tag{5}$$

where $\zeta_a = \frac{H}{2}$ is the wave amplitude given and H is the wave height, $\omega = \frac{2\pi}{T}$ is the wave frequency in $[\mathrm{rad/s}]$ where T is the period, t is the time investigated, $k = \frac{2\pi}{\lambda_W}$ is the wave number in $[\mathrm{rad/m}]$ where λ_W is the wave length and x is the distance along the x-axis.

From the linear wave theory, the velocity potential Φ of a regular wave in a general water depth can be described as shown in Eqn. (6):

$$\Phi = \frac{\zeta_a g}{\omega} \cdot \frac{\cosh k(h+z)}{\cosh kh} \cdot \cos(\omega t - kx) \tag{6}$$

where g is the gravity, h is the water depth, z is the elevation (+ is upward) from still water level and x is the distance from the z-axis.

From the derivative of the velocity potential, the kinematics of a water particle in a regular wave is found from the velocity component in the x-direction and in the z-direction. The velocity in the x- and in the z-direction can be written as shown in Eqn. (7) and Eqn. (8) respectively:

$$u = \omega\zeta_a \cdot \frac{\cosh k(h+z)}{\sinh kh} \cdot \sin(\omega t - kx) \tag{7}$$

$$w = \omega\zeta_a \cdot \frac{\sinh k(h+z)}{\sinh kh} \cdot \cos(\omega t - kx) \tag{8}$$

where h is the water depth, z is the elevation (+ is upward) from still water level and x is the distance from the z-axis.

2.3. Irregular waves and wave spectrum

Waves can be generated in many ways, e.g. by winds or tides. Wind waves, especially, are very irregular. Even so, they can be seen as a superposition of many simple, regular harmonic wave components, each with its own amplitude, length, period or frequency and direction of propagation. Such a concept is useful as it allows one to predict very complex irregular behaviour in terms of much simpler theory of regular waves [9]. This principle is illustrated in Figure 6.

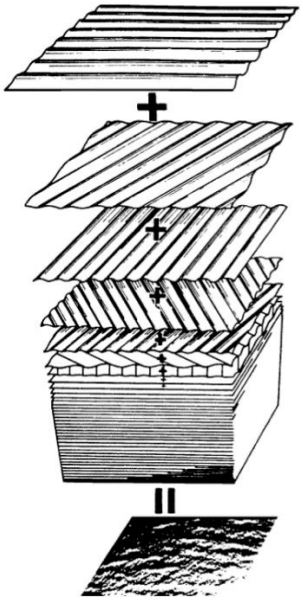

Figure 6 - Superposition principle. A sum of many simple sine waves, each with its own amplitude, length, period or frequency and direction of propagation, makes an irregular sea [9].

Short term stationary irregular sea states may be described by a wave spectrum, that is, the power spectral density function of the vertical sea surface displacement [11]. Figure 7 illustrates how the wave spectrum relates to the waves.

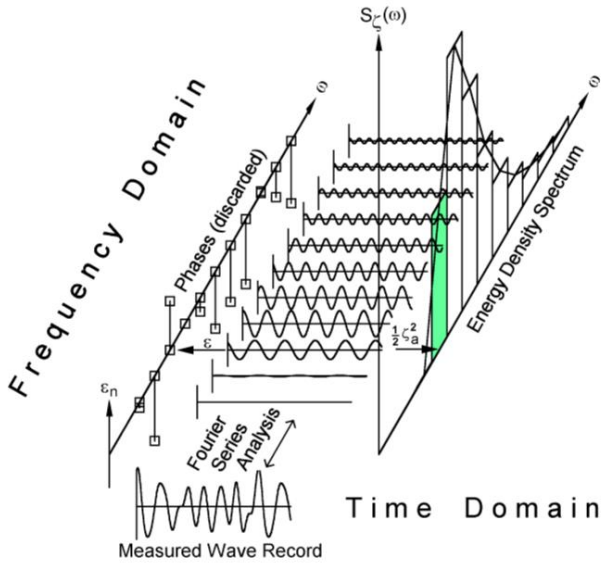

Figure 7 - Wave record analysis. The relation between the wave spectrum and the waves [9].

The most appropriate wave spectrum depends on the geographical area with local bathymetry and the severity of the sea state. The Pierson-Moskowitz (PM) and Joint North Sea Wave Project (JONSWAP) spectrum are frequently applied for wind-generated seas. The PM-spectrum was originally proposed for fully-developed sea, while the JONSWAP spectrum extends the PM-spectrum to include fetch limited seas, describing developing sea-states. Both spectra describe wind sea conditions that often occur for the most severe sea-states [11]. Figure 8 illustrates the comparison between the Pierson-Moskowitz and JONSWAP spectra. The PM-spectrum can be described as shown in Eqn. (9):

$$S_{PM}(\omega) = \frac{5}{16} H_s^2 \omega_p^4 \omega^{-5} \exp\left(-\frac{5}{4}\left(\frac{\omega}{\omega_p}\right)^{-4}\right) \tag{9}$$

where H_s is the significant wave height, the average of the 1/3 of the largest wave heights, and $\omega_p = 2\pi/Tp$ is the angular spectral peak frequency with T_p as the peak period (i.e. the time-period between two following wave peaks). The JONSWAP-spectrum is formulated as a modification of the PM-spectrum for a developing sea state in a fetch limited situation, as shown in Eqn. (10):

$$S_J(\omega) = A_\gamma S_{PM}(\omega) \gamma^{\exp\left(-0.5\left(\frac{\omega-\omega_p}{\sigma\omega_p}\right)^2\right)} \tag{10}$$

where γ is a non-dimensional peak shape parameter, σ is a spectral width parameter and $A_\gamma = 1 - 0.287\ln(\gamma)$ is a normalising factor [11].

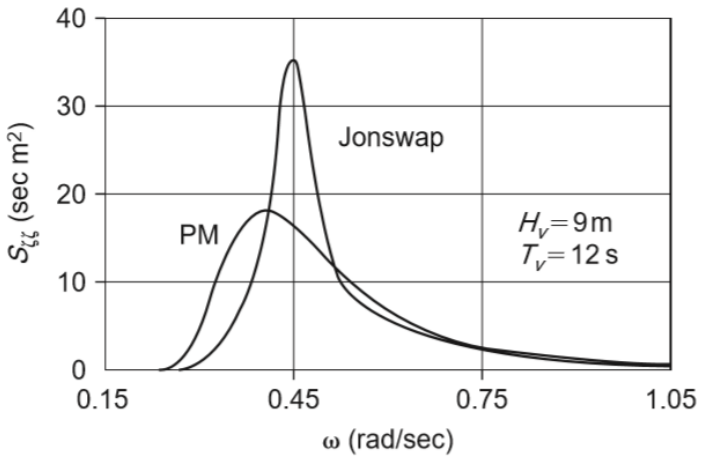

Figure 8 - Comparison of the Pierson-Moskowitz and the higher peaked JONSWAP spectra [12].

2.4. Six degrees of freedom

A floating body can have six independent motions and can be described as a dynamic system with six degrees of freedom, often expressed as 6DOF. This means that it can move in three directions, known as translations, and rotates in three directions as illustrated in Figure 9. The motions are defined as movements of the centre of gravity of the ship and rotations about a set of orthogonal axes through the centre of gravity, G [12]. The three translations are described as surge, sway and heave, and which are motions in the x, y and z-directions respectively. The three rotations are described as roll, pitch and yaw and, which are rotations around the x, y and z-axes respectively.

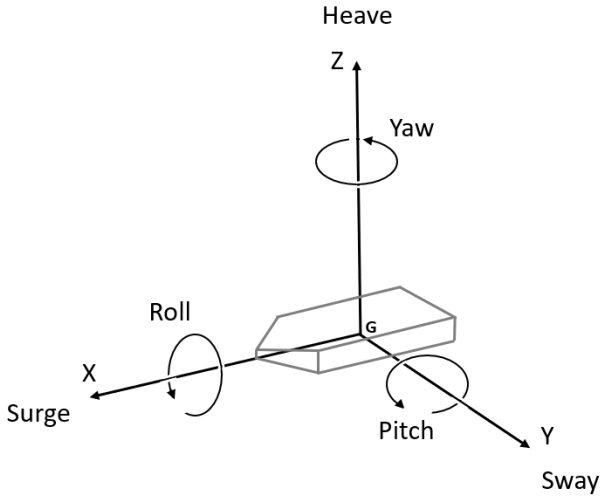

Figure 9 - Six degrees of freedom (6DOF). Three translations and three rotations around the centre of gravity G.

2.5. Response amplitude operators and response spectrum

A response amplitude operator (RAO), also referred to as a response variable or, a squared transfer function, can be defined as the ratio between the system output and the system input. It is used to determine the effect that a sea-state will have upon the motions of a vessel through the water. The RAO can be described in the frequency domain as shown in Eqn. (11):

$$|H(\omega)|^2 = \left(\frac{Y(\omega)}{X(\omega)}\right)^2 \tag{11}$$

where $H(\omega)$ is transfer function and where $Y(\omega)$ and $X(\omega)$ are the output and input values respectively.

The response spectrum of a system exposed to wave loads in a random sea, is a widely applied method for estimating the short-term response statistics of the system in the given sea state. The response spectrum can be described as the product of the of the wave spectrum and the system RAO as shown in Eqn. (12):

$$S_R(\omega) = S_w(\omega) \cdot |H(\omega)|^2 \tag{12}$$

The response spectrum can also be illustrated as in Figure 10 where the product of the magnitude of the sea spectrum in point A and the magnitude of the RAO in point B gives the magnitude of the response spectrum in point C for the given frequency.

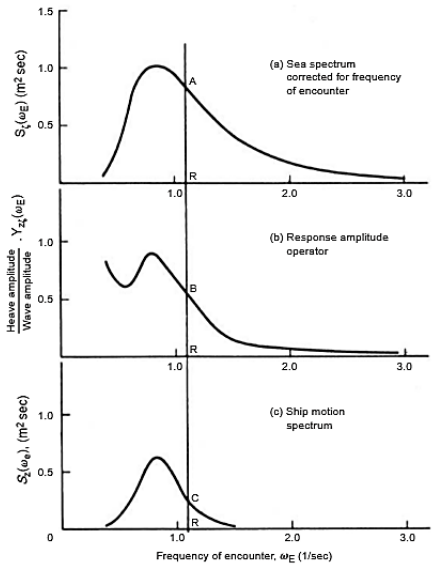

Figure 10 - Energy spectra and response of a ship in an irregular sea state (illustrated for the heave translation) [12].

2.6. Identification of the dynamics of an element

In order to identify the transfer function $G(s)$ of an element, standard input signals e.g. a step input or a sine wave should be used. The transfer function is defined as the ratio of the Laplace transform of the output to the Laplace transform of the input, provided the initial condition is zero [13]. This means the transfer function of the output signal is simply the product of the element transfer function and the transfer function of the input signal, as shown in Eqn. (13):

$$G(s) = \frac{\bar{f}_o(s)}{\bar{f}_i(s)} => \bar{f}_o(s) = G(s) \cdot \bar{f}_i(s) \tag{13}$$

This relation can also be illustrated using a block diagram representation as in Figure 11.

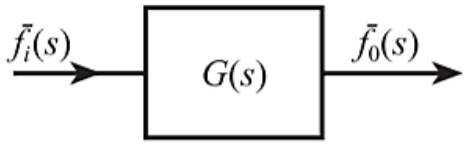

Figure 11 - General transfer function block diagram representation [13].

An elastic sensor, which converts a force input into a displacement output, can be used to describe such an element. The elastic sensor is illustrated in Figure 12 for a first-order element to the left in the figure, and a second-order element to the right in the figure.

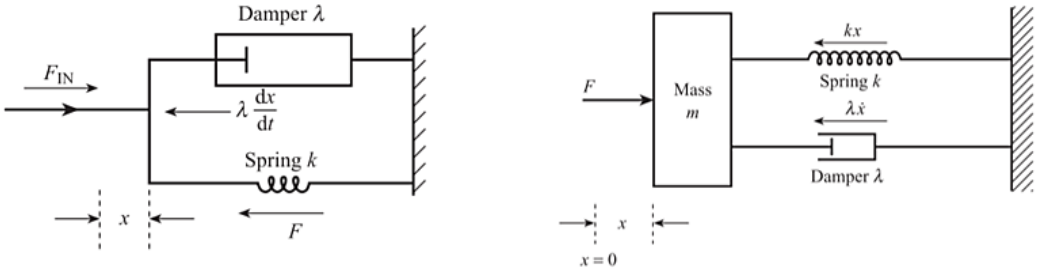

Figure 12 - Elastic force sensors illustrated with a spring-damper for the first-order element, and with a mass-spring-damper for the second-order element.

The first-order element can be described as shown in Eqn. (14):

$$G(s) = \frac{1}{1 + \tau s} \tag{14}$$

where τ is the time constant for the system and $s = j\omega$ is the complex variable. The response of a first-order element to a unit step is illustrated in Figure 13.

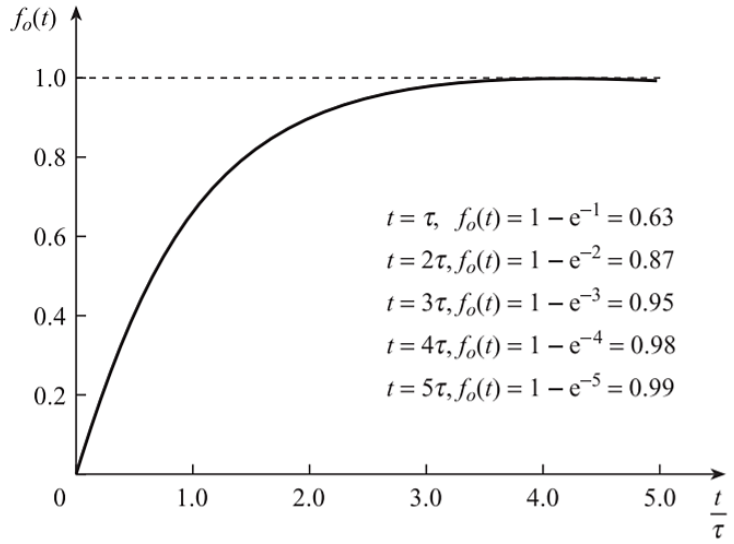

Figure 13 - Response of a first-order element to a unit step [13].

The second-order element can be described as shown in Eqn. (15):

$$G(s) = \frac{1}{\frac{1}{\omega_n^2}s^2 + \frac{2\xi}{\omega_n}s + 1} \tag{15}$$

where the undamped natural frequency is $\omega_n = \sqrt{\frac{k}{m}}$ is given in $[\mathrm{rad/s}]$ where k is the spring stiffness and m is the mass, and the damping ratio $\xi = \frac{\lambda_D}{2\sqrt{km}}$ where λ_D is the damping constant. The response of a second-order element to a unit step is illustrated in Figure 14.

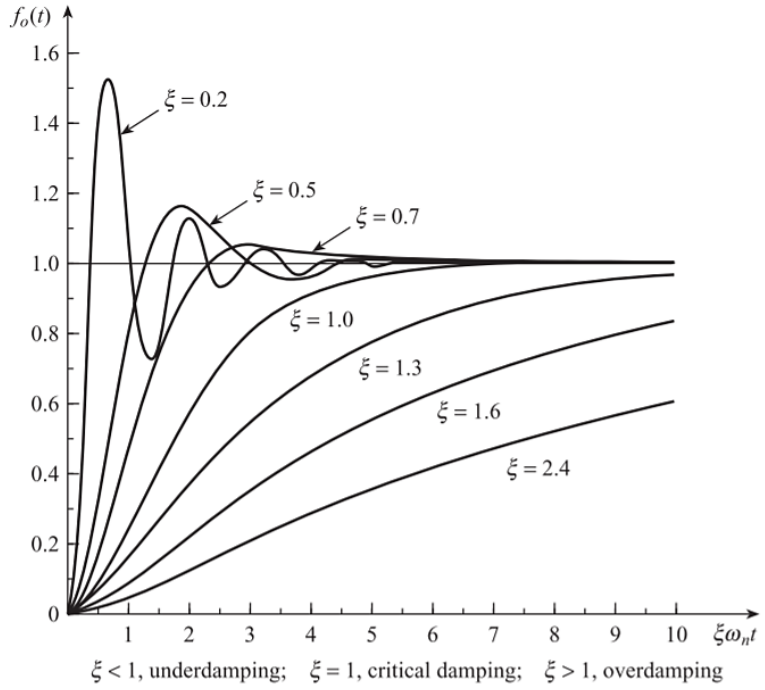

Figure 14 - Response of a second-order element to a unit step [13].

2.7. The normal distribution and confidence interval

During experimental testing, the force measured between the two connected bodies will vary. For linear systems, this variation would be expected to be normally distributed about a mean average. A continuous random variable x has a normal distribution if its probability density function is bell-shaped and symmetric about its mean value. The normal probability distribution is completely determined once its mean and standard deviation values, given as μ and σ respectively, are known. The normal probability density function is constructed so that the total area under the curve is 1. In this regard, the empirical rule where there is a 68% probability that the total area under the curve lies in the interval of $\pm 1\ \sigma$ of the mean, a 95% probability that the total area lies within the interval of $\pm 2\ \sigma$ of the mean, and a 99.7% probability that the total area lies within the interval of $\pm 3\ \sigma$ of the mean, as illustrated in Figure 15, holds [14].

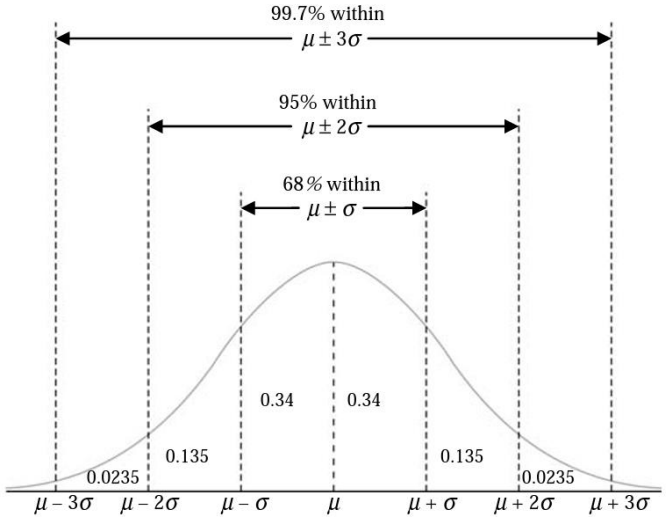

Figure 15 - The empirical rule shows that about 68% of the total area under the probability density function curve lies within the interval of ± 1 standard deviation of the mean, about 95% of the total area lies within the interval of ± 2 standard deviation of the mean, and 99.7% of the total area lies within the interval of ± 3 standard deviation of the mean [14].

A confidence interval indicates how precisely a parameter, e.g., the mean or standard deviation, has been estimated from a random sample. Most commonly the 95% confidence interval is being used, but the 90% and the 99% intervals are also often used. The narrower the interval is, the more precise the estimate will be. A 95% confidence interval determined from a particular sample may or may not contain the investigated parameter, however, if the process is repeated a large number of times, 95% of the calculated intervals would contain the investigated parameter and 5% would not [14].

2.9. Evaluating goodness of fit

A theoretical distribution can be used to test if sample data fits a distribution from a certain population. Goodness of fit tests provide statistical evidence to test hypotheses about the nature of the

distribution [15]. Some commonly used goodness-of-fit tests are the Chi-square test, the R-squared test and the root mean square error (RMSE) test which are described as shown in Eqn. (16), Eqn. (17) and Eqn. (18) respectively:

$$\chi^2 = \sum_{i=1}^{n} \frac{(y_i - f_i)^2}{f_i} \tag{16}$$

where χ^2 is the chi-squared value, y_i is the observed value and f_i is the expected value. As can be observed from the equation, a small chi-squared means that the observed value is close to the expected value and hence, a good fit.

$$R^2 = 1 - \frac{SSE}{SST} = 1 - \sum_{i=1}^{n} \frac{(y_i - f_i)^2}{(y_i - \bar{y})^2} \tag{17}$$

where R^2 is the R-squared value, $SSE = (y_i - f_i)^2$ is the sum of squared errors, also known as sum of squared residuals, and $SST = (y_i - \bar{y})^2$ is the total sum of squares with $\bar{y}$ as the mean of the observed value. As can be observed from the equation, an R-squared close to 1 means that the sum of squared errors is small (the observed value is close to the expected value), compared to the total sum of squares and hence, a good fit.

$$RMSE = \sqrt{\frac{\sum_{i=1}^{n}(y_i - f_i)^2}{n}} \tag{18}$$

where $RMSE$ is the root mean square error and n is the number of sample values. As can be observed from the equation, a small RMSE means that the observed value is close to the expected value and hence, a good fit.

Note, the units of chi-square and RMSE are in the units of the measured values whilst the R-squared are a dimensionless quantity.

2.10 Bending stress

A bending moment at any location along a beam can be used to calculate the bending stress over the beams cross-section. The bending stress can be described as shown in Eqn. (19):

$$\sigma_b = \frac{M}{I} \cdot z \tag{19}$$

where σ_b is the bending stress, M is the bending moment, z is the distance from the beam's neutral axis (often also denoted by c), to the point of interest along the cross-section height and I is the centroidal moment of inertia.

The bending stresses are linearly distributed in the z-direction as shown in Figure 16.

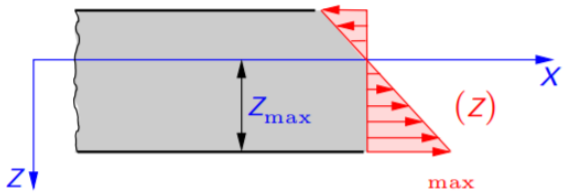

Figure 16 - Linearly distributed bending stress. If bending moment M is positive, the bending stress is positive (tensile stress) for $z > 0$, and negative (compressive stress) for $z < 0$. For $z = 0$ i.e., in the $x, y - plane$, $\sigma_b = 0$ [16].

The maximum tensile or compressive stress can be described as shown in Eqn. (20):

$$\sigma_{b_{max}} = \frac{M}{W} \tag{20}$$

where $\sigma_{b_{max}}$ is the maximum bending stress and $W = \frac{I}{|z|_{max}}$ is the section modulus. For a rectangular cross-section, the section modulus $W = \frac{b \cdot h^2}{6}$ [16].

2.11 Impulse load and impact force

An impulse load is defined as a change in momentum and can be described as an applied force for a duration of time, or as the product of an object's mass and the change in its velocity, as shown in Eqn. (21):

$$I = F \cdot \Delta t = m \cdot \Delta v \tag{21}$$

where I is the impulse load, F is the applied force and Δt is the duration of the force applied, m is the mass of the object and Δv is the change in velocity.

Deriving Eqn. (21) for the impact force gives Eqn. (22):

$$F = m \cdot \frac{\Delta v}{\Delta t} \tag{22}$$

Expected impact loads may be used in the design of a structure. In [17], when specific loads are not given, the contact area exposed to collision loads may be designed by assuming an impact force given in Eqn. (23):

$$F' = 2.5 \cdot \Delta' \tag{23}$$

where F' is the impact force in units of kN and Δ' is the fully loaded displacement of the maximum authorized supply vessel in units of tons. This is based on an assumption of boat impacts against hard structures. When a damper or spring devise such as a fender is provided in the area subjected to the impact, a lower impact force can be used.

3. Facilities and apparatus

3.1. MarinLab

The MarinLab [18] is a research and educational facility at the Department of Mechanical and Marine engineering, at Western Norway University of Applied Sciences situated in Bergen, Norway. The tank, as illustrated in Figure 17, has a length, width and water depth of $50\ \mathrm{m}$, $3\ \mathrm{m}$ and $2.2\ \mathrm{m}$ respectively. The fluid used in the tank is freshwater with a temperature at around $6°\ \mathrm{C} - 14°\ \mathrm{C}$ (depending on how recently it is changed), hence a fluid density of approximately $1000\ \mathrm{kg/m^3}$. The wave generator is installed by Edinburgh Designs and consists of six flaps with force-based feedback. The wave generator can operate with a maximum wave height at $0.5\ \mathrm{m}$, and a wave period between $0.7\ \mathrm{s} - 3\ \mathrm{s}$. At the opposite side of the wave generator is a perforated wave absorbing beach in order to damp out unwanted wave reflections from the end of the wave tank. Further, the MarinLab is equipped with resistance-type wave gauges, a Qualisys motion capture camera system and computers to operate the complete system.

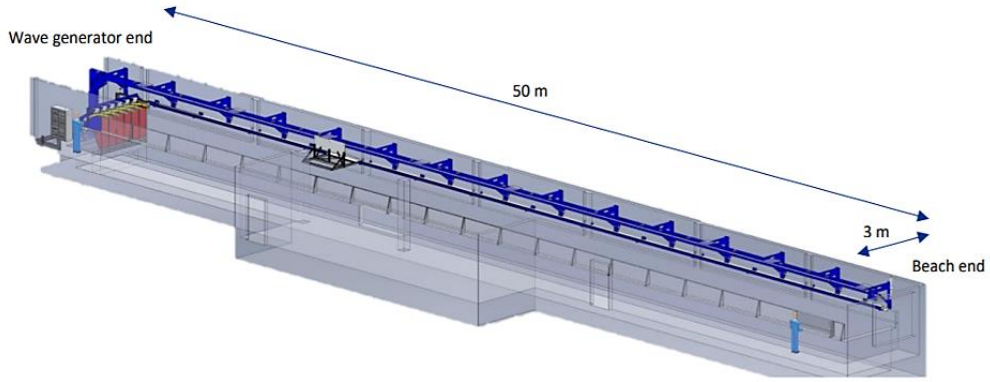

Figure 17 - MarinLab facility overview [18].

3.2. Software tools

Beneath, some of the software tools used in this project are presented.

SESAM

SESAM is an offshore structural engineering software tool developed by DNV-GL and used for design, optimisation, simulations and analysis of a variety of offshore constructions and operations. The software package consists of multiple subprograms which are used for different analysis. The modelling is done in GeniE, while HydroD is used for hydrostatic and hydrodynamic analysis where Wadam is used for the frequency domain wave loads analysis. Postresp is further used for the presentation of the statistical responses [19].

Creo Parametric

Creo Parametric is a 3D modeling software which allows the user to create, analyse, view and share designs using 2D CAD, 3D CAD, parametric and direct modeling capabilities [20].

Njord Wave Synthesis

Edinburgh Design develops software tools specifically for running experiments in a wave tank. The wave synthesizer allows the user to specify, using a graphic interface, the waves to be used in an experiment. The software then outputs the wave data in an open XML-based file format optimized for loading into the Edinburgh Designs Wave Runtime, from where it can be run in a wave tank [21].

Qualisys

Qualisys is a motion capture and 3D position tracking system. The optical tracking technology makes it possible to measure the position of fast-moving objects. The system consists of motion capturing cameras, reflectors and software which allows for 6DOF tracking [22].

LabVIEW

LabVIEW is a data acquisition and hardware control software used for collection sampled data from the experiments [23].

MATLAB

MATLAB is a programming platform used for computations and plotting of functions from the measured data collected in the experiments [24].

4. Method

In this chapter, presentations of the methods used for the modeling and building of the models, experimental setup, calibrations and how the experiments are executed are presented.

4.1 Modelling for the experiment

The models used in the experiments are downscaled and simplified models of the full-scale structures. To get the models as accurate as possible and with the correct mass distribution, the full-scale FOWT and barge are modelled using the software tool SESAM. Simplifications are made as details of internal and external geometries are unknown and which are assumed to be irrelevant for the experiment. The load cell rig is modelled in Creo Parametric

4.1.1. Modelling of the full-scale FOWT and barge in SESAM

First, the floating offshore wind turbine is modelled in the subprogram GeniE using the technical drawing of the Hywind Buchan Deep turbine [25] as a reference and shown in Figure 18,. Simplifications have been made which are explained underway.

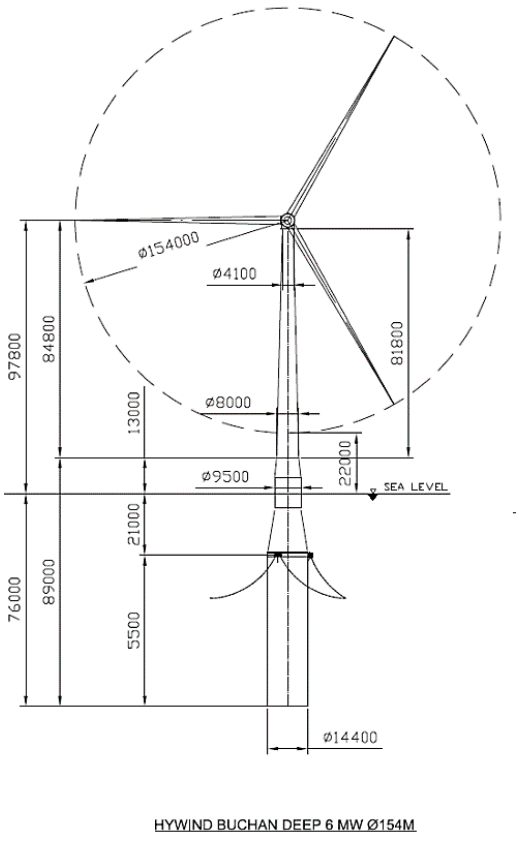

Figure 18 - Technical drawings of the 6 MW Hywind Scotland Buchan Deep turbine [25].

The coordinate system is set in the centre of the bottom of the structure where the x- and y-axis gives the horizontal plane and the z-axis, the vertical direction.

To get the mass distribution for the substructure, it is modelled with an equivalent plate thickness as the internal geometries are unknown. The mass of the substructure is given as 2300 tonnes [26] and hence the equivalent thickness is found using GeniE for the geometry given in Figure 18. The thickness is found to be approximately $77.1\ \mathrm{mm}$ when using mild steel with density $7850\ \mathrm{kg/m^3}$ as material. This gives a COG for the substructure at approximately $39.45\ \mathrm{m}$.

The tower is simplified and modelled as a cone in one piece from the substructure top to the bottom of the nacelle with a bottom diameter of $9.5\ \mathrm{m}$, a top diameter of $4.1\ \mathrm{m}$ and a height of $81.8\ \mathrm{m}$. The tower is also modelled using equivalent plate thickness as internal geometries are unknown. The mass of the tower section is close to 670 tonnes as given in [26]. The thickness is found to be approximately $48.2\ \mathrm{mm}$ when using mild steel with density $7850\ \mathrm{kg/m^3}$. This gives a COG for the tower at approximately $124.81\ \mathrm{m}$.

The geometries of the head of the turbine, consisting of the nacelle, hub and blades, are made with geometric simplifications and are only meant as an illustration. To further simplify the modelling, the tower head mass, given as 360 tonnes in [27], is set as a point load at the centre of the nacelle with coordinates at [0 m, 0 m, 173.8 m].

The mass of the displaced seawater is found in a hydrostatic table in HydroD when the substructure is submerged $76\ \mathrm{m}$. The mass is 11496 tonnes, which is quite accurate when compared with the total mass of the FOWT as given in [26].

The mass of the ballast is then found by subtracting the mass of the substructure, the tower, and the tower head mass from the mass of the displaced water. The ballast mass is found to be 8166 tonnes.

The ballast includes solid and liquid ballasts. The solid ballast is 5000 tonnes iron ore as given in [25]. It is assumed to consist a high-density aggregate with a density of $5000\ \mathrm{kg/m^3}$. The liquid ballast is assumed to be the rest and to consist of seawater with a density of $1025\ \mathrm{kg/m^3}$ with a mass of 3166 tonnes.

The height of the ballast volume is calculated using Eqn. (24) as the cross-section area of the lower part of the cylinder is constant.

$$V_i = A_i \cdot h \Rightarrow h = \frac{V_i}{A_i} = \frac{V_i}{\frac{\pi \cdot d_i^2}{4}} \tag{24}$$

where V_i is the volume of the inner cylinder, A_i is the inner cylinder cross section area, h is the height and d_i is the inner cylinder diameter.

The centre height of the solid ballast is found using Eqn. (24). When the wall thickness of the substructure bottom of $77.1\ \mathrm{mm}$ is included, the point load of the solid ballast is set in the centre of the height at $3.21\ \mathrm{m}$ with the coordinates [0 m, 0 m, 3.21 m], based on the calculation as shown in Eqn. (25):

$$h_{C_{SB}} = \frac{1}{2} \cdot h_{SB} = \frac{1}{2} \cdot \frac{\frac{5000000\ \mathrm{kg}}{5000\ \frac{\mathrm{kg}}{\mathrm{m}^3}}}{\frac{\pi \cdot (14.4\ \mathrm{m} - 2 \cdot 0.0771\ \mathrm{m})^2}{4}} \approx 3.13\ \mathrm{m} \tag{25}$$

where $h_{C_{SB}}$ is the centre height of the solid ballast and h_{SB} is the total height of the solid ballast.

The centre height of the liquid ballast point mass is also calculated using Eqn. (24) as shown in Eqn. (26):

$$h_{C_{LB}} = \frac{1}{2} \cdot h_{LB} = \frac{1}{2} \cdot \frac{\frac{3166000\ \mathrm{kg}}{1025\ \frac{\mathrm{kg}}{\mathrm{m}^3}}}{\frac{\pi \cdot (14.4\ \mathrm{m} - 2 \cdot 0.0771\ \mathrm{m})^2}{4}} \approx 9.69\ \mathrm{m} \tag{26}$$

where $h_{C_{LB}}$ is the centre height of the liquid ballast and h_{LB} is the total height of the liquid ballast.

The liquid ballast is placed above the solid ballast and hence, when the wall thickness of the substructure bottom and the total height of the solid ballast is included, the coordinates of the liquid ballast point mass is [0 m, 0 m, 16.03 m].

When all point masses are included, the global mass distribution of the full-scale FOWT is found using GeniE as shown in Figure 19.

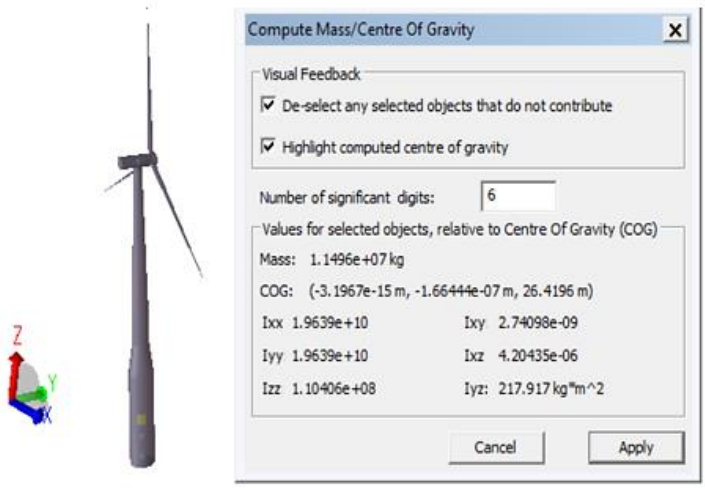

Figure 19 - Screenshot from GeniE of the SESAM software tool showing the full-scale FOWT and its global mass distribution.

The barge has also been modelled in GeniE and based on the design of the barge Goliat17 [28], as shown in Figure 20. Also here, simplifications have been made which are explained underway.

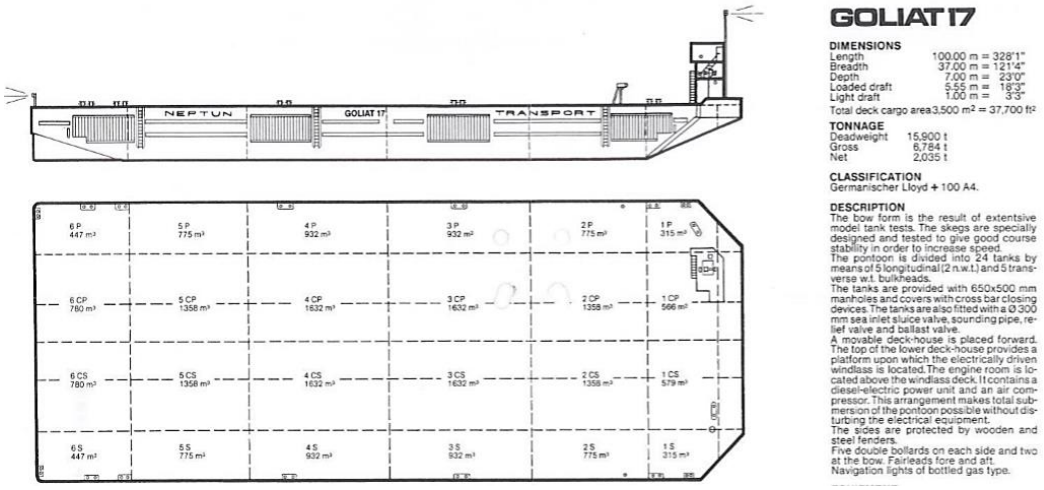

Figure 20 - Technical drawing and specifications of the barge Goliat17 which is used as a reference for the barge in this project [28].

The coordinate system is set in the centre of the bottom of the structure with the same axis directions as described for the FOWT.

Similar to the FOWT, in order to find the COG for the barge, it is modelled with an equivalent plate thickness as the internal geometrics are unknown. For simplicity, the barge is modelled with eight transverse and five longitudinal bulkheads, including the hull. Also, the machinery and the deck-house are not included in the modelling.

The mass of the displaced seawater is found in a hydrostatic table in HydroD, when the barge is submerged $1\ \mathrm{m}$ as is its light draft. The mass is 2841.6 tonnes which is used as the reference for the lightship mass of the barge.

The plate thickness of the bulkheads and the hull is then found to be approximately $30.03\ \mathrm{mm}$ when using mild steel with density $7850\ \mathrm{kg/m^3}$ as material, and which gives approximately correct lightship mass. This gives a global mass distribution for the barge as shown in Figure 21.

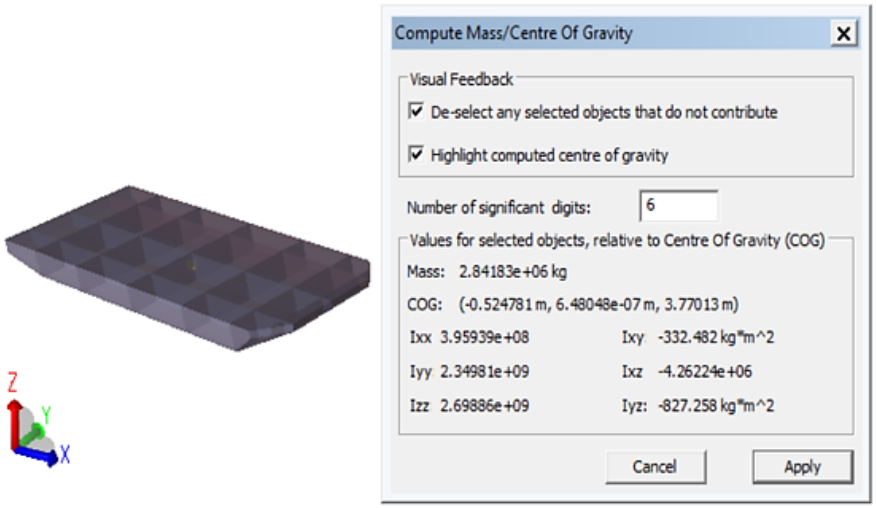

Figure 21 - Screenshot from GeniE of the SESAM software tool showing full-scale barge and its global mass distribution.

4.1.2. Scaling, modeling and manufacturing of the scaled FOWT and barge.

The forces involved in the experiment are dominated by hydrostatic, hydrodynamic, gravitational, inertial and contact forces, hence the scaling is done by the Froude scaling law with the relationship between the scaled model and the full-scale structure as shown in Table 1. The experiments are executed with a 1:72 scaling factor. By using this scaling factor, the scaled models are within an acceptable limit for the wave-tank without having to worry about the blockage effect due to reflections from the wave-tank walls.

The physical scaled model of the FOWT was built in aluminum and with dimensions as shown in Table 2, found using the Froude scaling relationship shown in Table 1. It was decided to simplify the model where the coned parts of the structure are left out. The model is rather built with a constant diameter of 0.2 m through the waterline. The tower was also built with a constant diameter. The simplifications do not correspond with the scaling laws concerning geometric similarity however, it is assumed that the influence of these does not affect the result to a significant degree.

Table 2 - Dimensions for the model scaled FOWT, based on [25] and the Froude scaling relationships from Table 1.

Parameter	Full-scale FOWT	Model scaled FOWT
Total mass	$m_{\mathrm{F}} = 1.15\mathrm{E}+07$ kg	$m_M = 30.06$ kg
Tower head mass	$m_{\mathrm{THM}_F} = 3.6\mathrm{E}+05$ kg	$m_{THM_M} = 0.94$ kg
Height, tower head mass	$h_{THM_F} = 173.8$ m	$h_{THM_M} = 2.41$ m
Height, center of gravity	$h_{COG_F} = 26.42$ m	$h_{COG_M} = 0.367$ m
Diameter, substructure	$D_F = 14.4$ m	$D_M = 0.2$ m
Draft	$T_F = 76$ m	$T_F = 1.056$ m

Using these parameters and the above-mentioned simplifications, the scaled FOWT is modelled as seen in Figure 22. It should be noted that because a cylinder with a constant cross-section is used for the substructure, the draft of the scaled model will not agree for both the model scaled draft and the model scaled total mass. It was decided upon using the model scaled draft, which resulted in an increased total mass of $33.175\ \mathrm{kg}$. This helped to reduce the height of the COG.

Ballasting was performed to get the COG as low as possible. It should be noted however, that the COG is $49.0\ \mathrm{mm}$ higher than wanted, as the restrictions in the thickness of the materials available would not allow for it to go lower. However, the COG is lower than the COB and hence, the properties of the spar-buoy are kept, and the effect is assumed to be small. A small steel plate is also included in the scaled model. This plate will allow for the scaled FOWT and the scaled barge to be connected by using electromagnets and is the cause for the small off-balance in the COG in the x-direction.

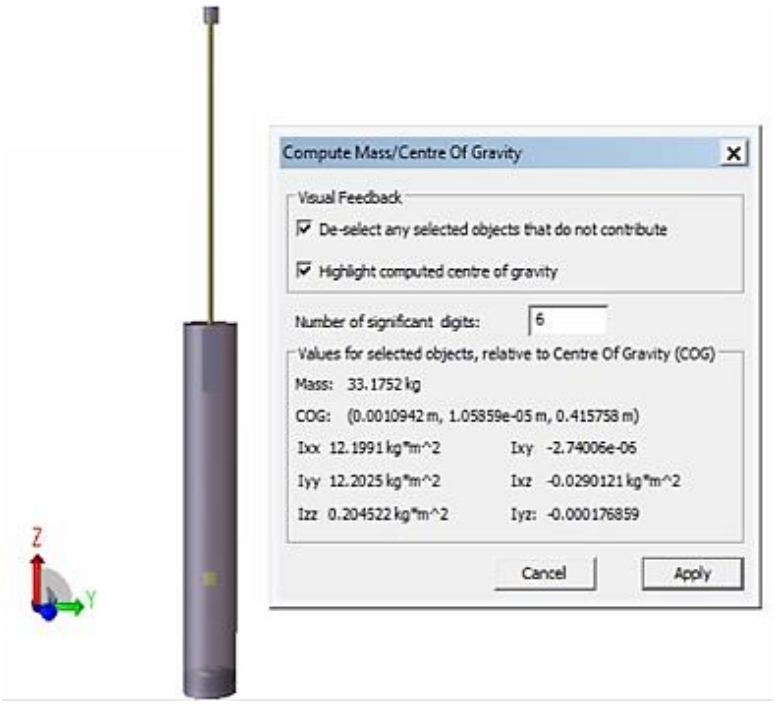

Figure 22 - Screenshot from GeniE of the SESAM software tool showing the simplified scaled FOWT and its global mass distribution.

The physical scaled model of the barge was machined from Divinycell isoporous foam. It was first modelled in Creo Parametric with dimensions as shown in Table 3, found using the Froude scaling relationship shown in Table 1, before it was sent to a four-axis CNC machine to be machined. Divinycell is a very light material with a density of $60\ \mathrm{kg/m^3}$, and with a low water absorption, thus it has the necessary properties for a floating body. The machined Divinycell parts were then applied with a two-component mortar, ground down and coated before a plywood plate, used as the top deck, was attached. This stiffened the construction and allowed for the loadcell rig to be attached firmly. The scaled barge was ballasted internally and externally to compensate for the loadcell rig and to get it to

the wanted operational draft of $55.6\ \mathrm{mm}$. HydroD was used to get the model ballasted correctly for equilibrium and stability.

Table 3 - Dimensions for the model scaled barge, based on [28] and the Froude scaling relationships from Table 1.

Parameter	Full-scale barge	Model scaled barge
Length	$l_F = 100\ \mathrm{m}$	$l_M = 1.389\ \mathrm{m}$
Breadth	$b_F = 37\ \mathrm{m}$	$b_M = 0.514\ \mathrm{m}$
Depth	$d_F = 7\ \mathrm{m}$	$d_M = 0.097\ \mathrm{m}$
Draft	$T_F = 4\ \mathrm{m}$	$\mathrm{T_M} = 0.056\ \mathrm{m}$
Displacement at draft	$m_F = 1.295 \cdot 10^7\ \mathrm{kg}$	$m_M = 33.85\ \mathrm{kg}$

Using these parameters and the above-mentioned ballasting configurations, the scaled barge is modeled and stabilised as seen in Figure 23.

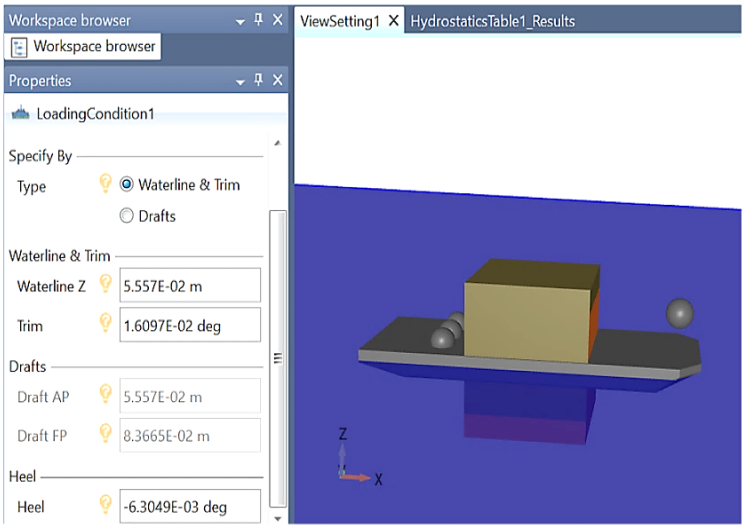

Figure 23 - Screenshot from HydroD of the SESAM software tool showing the scaled barge, its external ballast and equilibrium configuration. The two cubes in the centre is the COG and COB where the first is the top one and the latter is the bottom one, (the graphic in HydroD is not optimal for a model scale and hence, the size of the cubes).

4.1.3. Modeling and manufacturing of the load cell rig

In the experiment performed, two different load cells are used to measure the applied forces between the scaled FOWT and the scaled barge in the different sea states. These have a capacity to measure loads up to $250\ \mathrm{N}$ and $500\ \mathrm{N}$, both in tension and compression, and are designed to measure loads axially. Any angular loads, or loads parallel to their cross-section, might damage or destroy the load cells. To prevent this, a load cell rig is designed and built with the purpose to limit off-axis loading. The load cell rig is built in aluminum and with four spring steel beam elements, each with a thickness of $1.0\ \mathrm{mm}$, and which allows for the distribution of the loads correctly onto the load cells. Two electromagnets are also included in the rig. The purpose of the electromagnets is to connect the scaled models together and to release them at the intended instance in the collision experiment.

The load cell rig is first modeled in Creo Parametric as shown in Figure 24. From the software tool, the mass and the COG for the load cell rig is given as $6.86\ \mathrm{kg}$ and with the coordinates [0.425 m, 0.000 m, 0.141 m], when the coordinate system is as shown on the figure below. It should be noted that the load cell rig is modeled without any bolts and hence, the final mass is $7.2\ \mathrm{kg}$. It is assumed however, that the coordinates for the COG is the same as given above. The mass and the COG coordinates are used in HydroD to get the scaled barge ballasted to equilibrium.

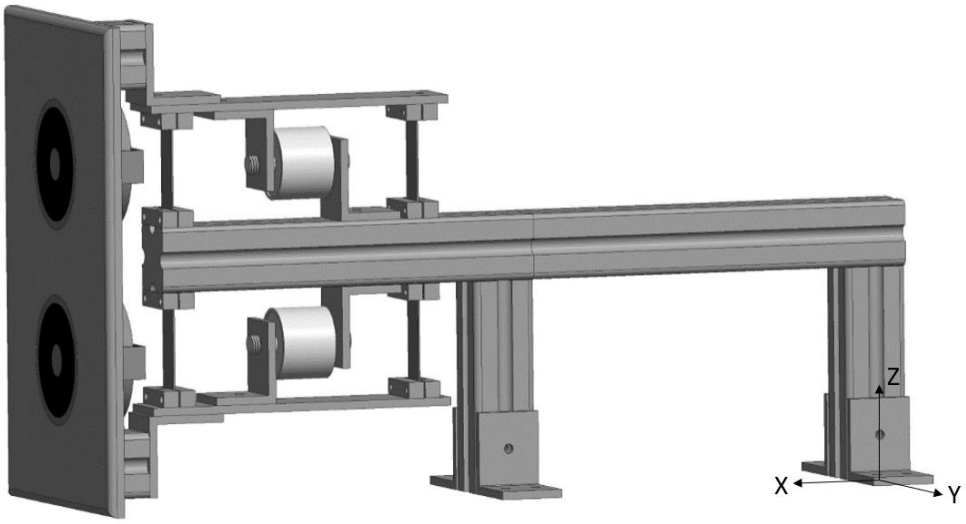

Figure 24 - The load cell rig modeled in Creo Parametric. The two load cells, shown with white colour, are attached with two brackets which are framed in between two spring steel beam elements each. This to distribute the loads correctly onto the load cells. Two electro magnets are placed in the front on the contact plate to the left in the figure. The coordinate system is placed in the bottom centre of the right leg.

4.2. Experimental setup and calibration

In this chapter the experiment setup and the calibration of the wave gauges, wave spectra's and load cell rig are presented.

4.2.1. Experimental setup

To prevent the model scaled FOWT and barge to drift away from the measuring area, they are both moored to the sides of the wave tank. Two mooring lines for the FOWT, across the tank, and four for the barge with configuration as shown below in Figure 25. Each mooring line is equipped with two springs, with a combined spring stiffness of approximately $6.57\ \mathrm{N/m}$, to allow for a natural response. The moorings are pre-tensioned to the point just before the springs start to act.

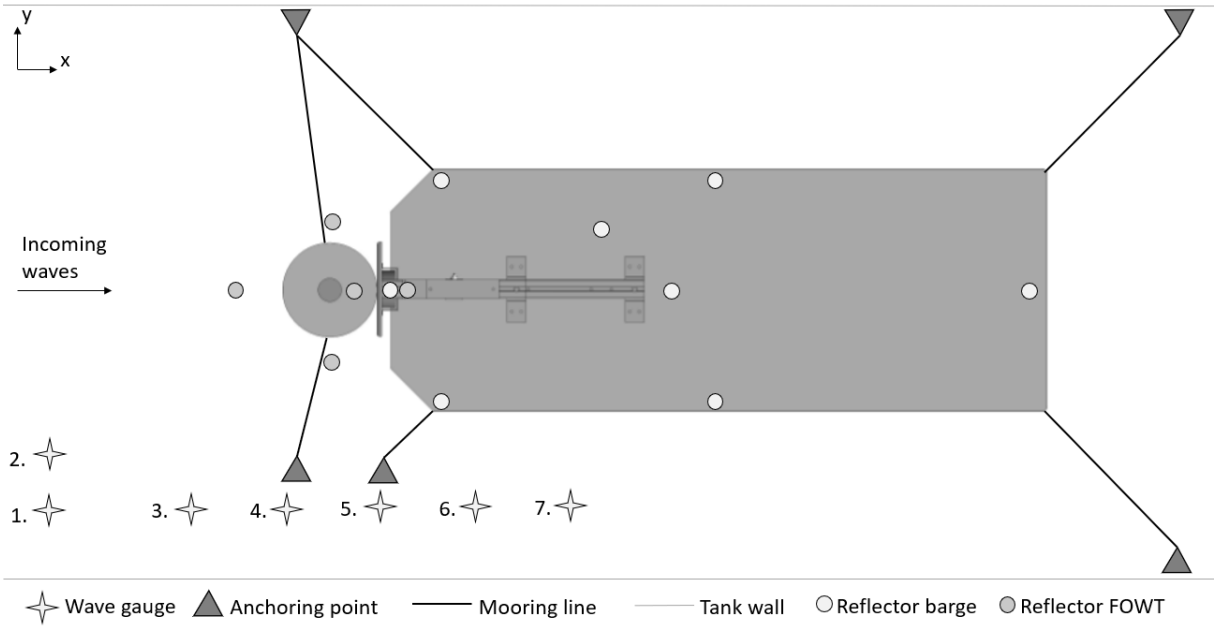

Figure 25 - Experimental setup of the FOWT and barge in the wave-tank, with moorings, reflectors and wave gauges. The distance between wave gauge one and three is 0.51 m*. The distance between the wave gauges three to seven are* 0.20 m*, which is the same as the model scaled FOWT cylinder diameter. To prevent the bottom left mooring lines to interfere with the wave gauges, their connection points have been moved from the tank wall to a location between the wave gauges and the scaled models. The figure is not in scale.*

The real time experimental setup with the physical models is illustrated in Figure 26.

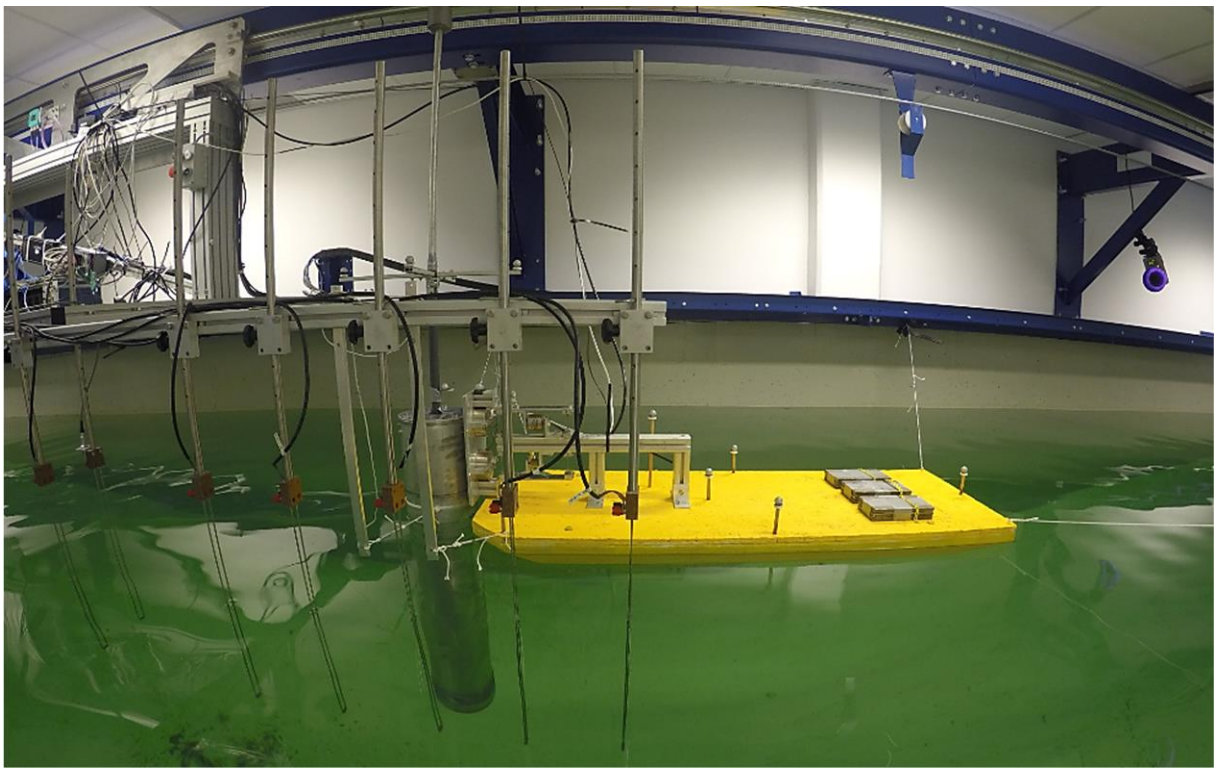

Figure 26 - Photo of the real time experimental setup with the physical models in the wave-tank.

4.2.2. Decay test

The mooring lines are only meant to keep the two bodies in place and are not intended to prevent them from their natural behavior. To investigate if the moorings affect any natural responses, a decay test is performed for the two models separately, and when they are attached and act as a single body. These tests are performed for the heave translation, and the pitch and roll rotations only, as these are the degrees of freedom which are relevant and comparable with and without moorings. The tests are first performed for the moored case, then for the case without the mooring. The models are oscillated with an applied force, or a step input, before it is released. It should be noted that the forces are applied manually and hence, might not have the exact same magnitude for the different cases. The motion capturing system Qualisys is used to capture the responses, with a sampling rate of 100 per second, and a MATLAB script with a curve fitting tool is later used to calculate the natural period of the damped oscillations, the frequency and the damping ratio. The results from the decay tests are presented in Table 4 to Table 6 and shown with plots in Figure 27 to Figure 32.

The decay test of the FOWT, with and without moorings, shows a good similarity for the heave and pitch response as can be seen in Table 4, Figure 27 and Figure 28. For the roll response however, there is a slight difference. It was observed during the tests, that the FOWT wanted to rotate in the yaw rotation as well as in the intended roll rotation. This is because the steel plate, which interface with the electromagnets, makes the FOWT model's COG slightly off balance and causes it to yaw. For the case with moorings, this response is hindered by the moorings which causes it to yaw back and forth as can be seen in Figure 27. For the case without the moorings, this does not affect the natural response of the model, shown in Figure 28 as it turns only in one direction. When comparing the damping ratio from Table 4 and the graphs in Figure 27 and Figure 28 with the damping ratios shown in Figure 14, the decay tests indicate that the FOWT model act as an underdamped system.

Table 4 - Comparing the results of the decay test of the FOWT with and without moorings.

Decay test FOWT with moorings			
Translation/Rotation	**Period [s]**	**Frequency [Hz]**	**Damping [Ns/m]**
Heave	2.13	0.47	0.047
Pitch	4.18	0.24	0.048
Roll	3.42	0.29	0.047
Decay test FOWT without moorings			
Heave	2.14	0.47	0.045
Pitch	4.23	0.24	0.053
Roll	4.26	0.23	0.038

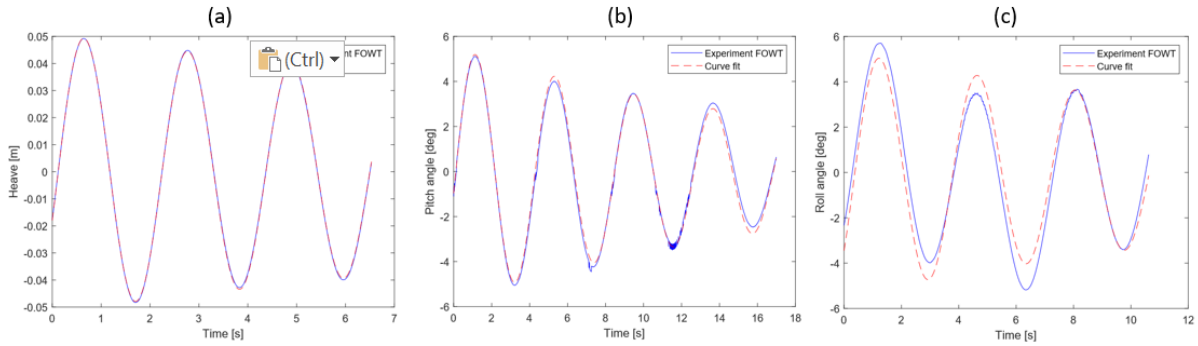

Figure 27 - Decay plot of (a) heave, (b) pitch and (c) roll for the FOWT with moorings.

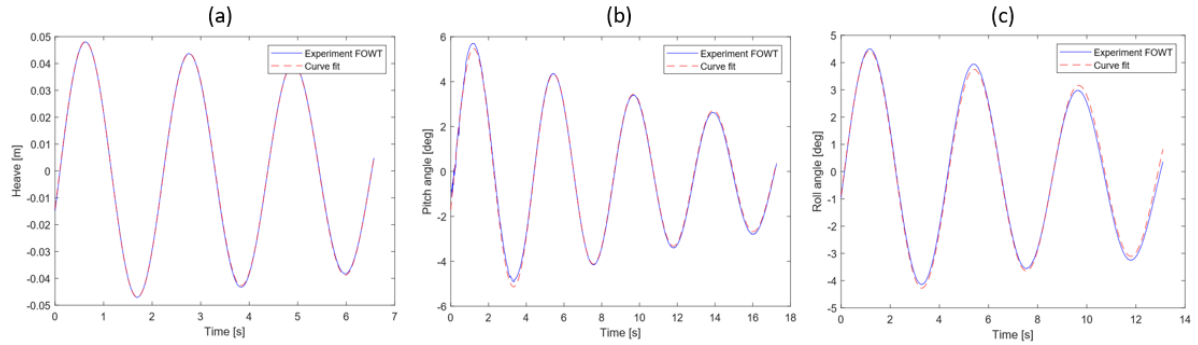

Figure 28 - Decay plot of (a) heave, (b) pitch and (c) roll for the FOWT without moorings.

The decay test of the barge, with and without moorings, shows a good similarity for the tested translation and rotations as is shown in Table 5, Figure 29 and Figure 30. It is assumed that the moorings do not affect the natural response of the barge to any significant degree. It should be noted that since the barge have a quite large waterline area, it is difficult to force it into a heave and pitch motion. This is a typical behavior of an overdamped system which seems reasonable when comparing the magnitude of the damping ratio in heave and pitch from Table 5 with the damping ratios in Figure 14. For the roll rotation however, it acts as an underdamped system when compared with the damping ratios in Figure 14.

Table 5 - Comparing the results of the decay test of the barge with and without moorings.

Decay test barge with moorings			
Translation/Rotation	**Period [s]**	**Frequency [Hz]**	**Damping [Ns/m]**
Heave	0.93	1.07	1.694
Pitch	0.98	1.02	2.024
Roll	0.77	1.30	0.560
Decay test barge without moorings			
Heave	1.04	0.96	1.921
Pitch	0.98	1.03	1.616
Roll	0.79	1.27	0.722

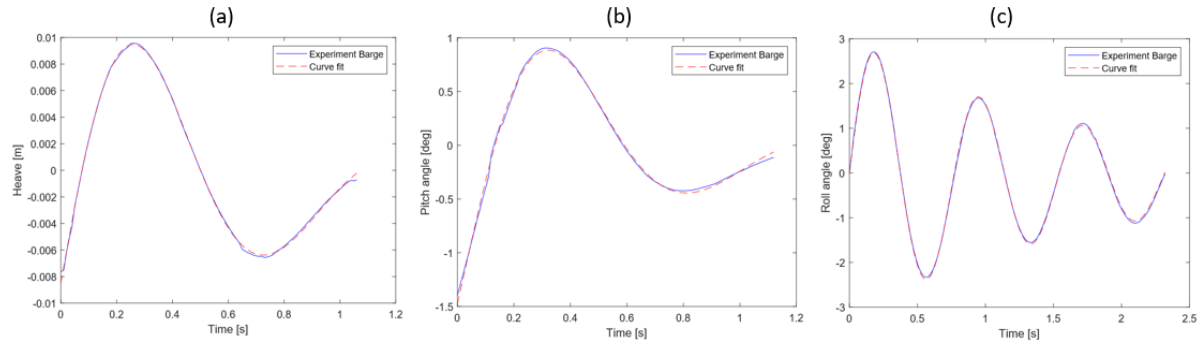

Figure 29 - Decay plot of (a) heave, (b) pitch and (c) roll for the barge with moorings.

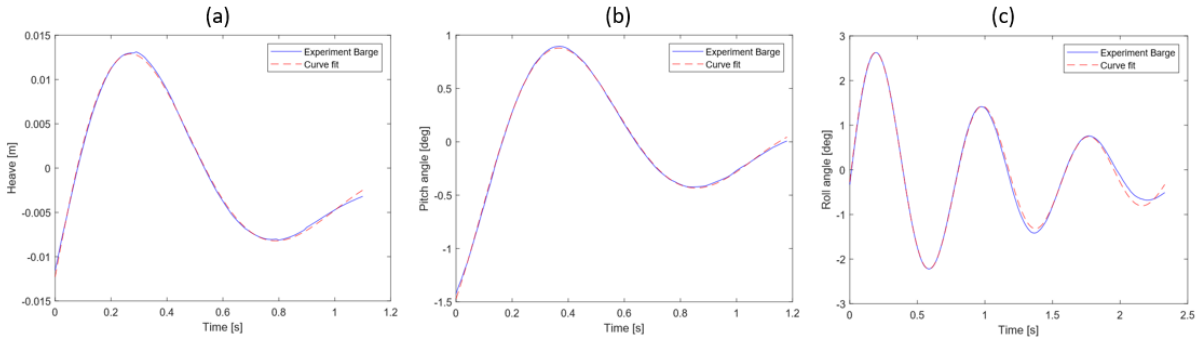

Figure 30 - Decay plot of (a) heave, (b) pitch and (c) roll for the barge without moorings.

When the two different systems are connected and act as a single system, their characteristics are changed to a response somewhere in between the two single system responses. The decay test with and without moorings, shows a good similarity in pitch and roll, and it can be assumed that the moorings does not interfere with the combined system's natural response to any significant degree in these rotations. However, as can be observed for the heave response, there is a difference. The heave response without moorings is clearly exposed to two frequencies which may be assumed to be the two separate systems acting against each other as shown in Figure 32. When the system is moored, this is slightly cancelled out as can be observed in Figure 31. This may affect the results to an uncertain degree, however, the plots show that there still is a correlation between the two cases, and hence, the effect is not assumed to be significant.

It should be noted that the MATLAB script does not manage to find the natural period of the damped oscillations, the frequency and the damping ratio in the heave translation due to the double frequencies, and so it is done manually for the moored case by finding the period from the time difference between the peaks in the plot and the damping by using Eqn. (27):

$$y_n = e^{-\xi \cdot t} \tag{27}$$

where y_n is the n-peak value, t is the time along the x-axis and ξ is the damping ratio. For the heave case without mooring however, this proved to be more difficult.

When comparing the damping ratio from Table 6 and the graphs in Figure 31 and Figure 32 with the damping ratios shown in Figure 14, the decay tests indicate that the connected bodies model act as an underdamped system.

Table 6 - Comparing the results of the decay test of the FOWT and the barge connected, with and without moorings.

Decay test of the connected FOWT and barge with moorings			
Translation/Rotation	**Period [s]**	**Frequency [Hz]**	**Damping [Ns/m]**
Heave	1.96	0.51	0.449
Pitch	1.76	0.57	0.103
Roll	2.21	0.45	0.068
Decay test of the connected FOWT and barge without moorings			
Heave	x	x	x
Pitch	1.76	0.57	0.103
Roll	2.45	0.41	0.032

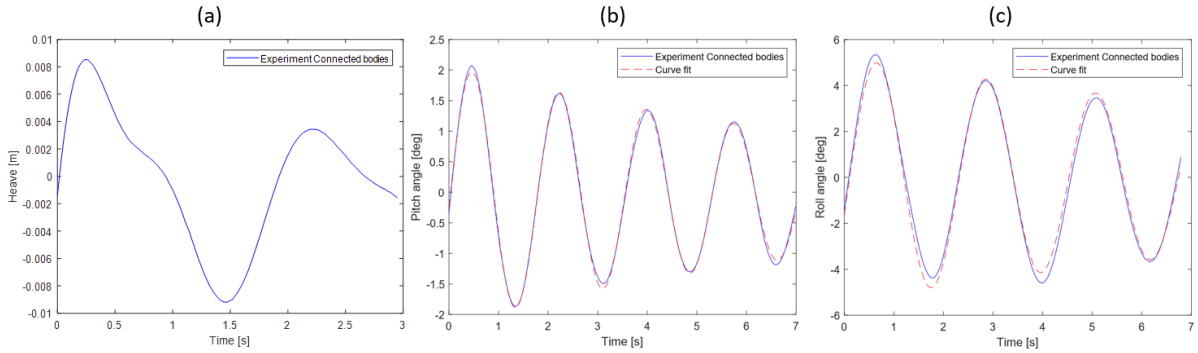

Figure 31 - Decay plot of (a) heave, (b) pitch and (c) roll for the two connected bodies, with moorings.

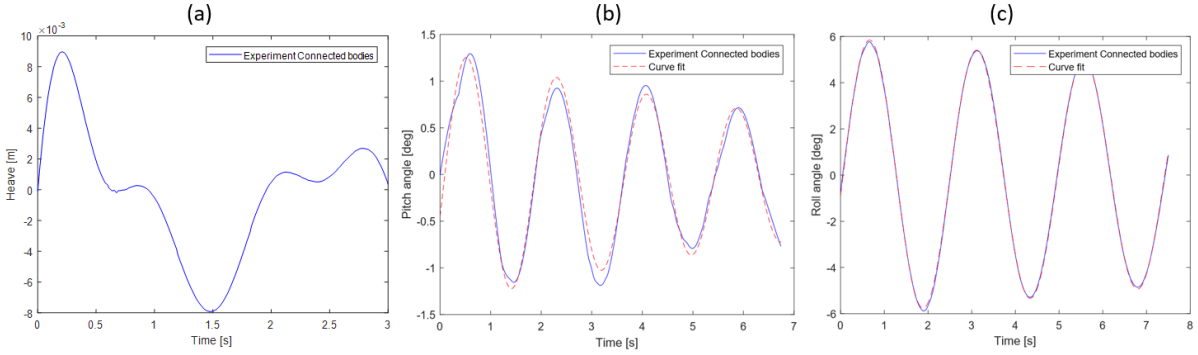

Figure 32 - Decay plot of (a) heave, (b) pitch and (c) roll for the two connected bodies, without moorings.

4.2.3. Response amplitude operators for the connected models

The scaled barge and the scaled FOWT are modeled together as a connected system in SESAM to investigate the connected systems RAO's in heave and pitch. The incoming waves are set from zero degrees so that the simulations simulate the response of the system using the same configuration as in the experiments. The motion reference point is moved from its global origin, placed in the center of the barge's xy-plane and with the z-axis in zero at the water level, to the connected system's COG for the fully drafted and reduced draft case with the coordinates given as [0.38 m, 0 m, -0.22 m] and [0.34

m, 0 m, -0.13 m] respectively. The result from the RAO's are shown in Figure 33. As observed in the figure, the maximum response from the heave and pitch occurs at $t = 1.4$ s for the fully drafted case and $t = 1.3$ s for the reduced draft case. Further, the pitch responses fall towards zero and crosses the heave responses at approximately $t = 2.0$ s, where the heave responses converge towards 1. This applies for both the fully drafted and the reduced draft case. The simulations illustrate that there is a small difference in the pitch and heave responses which is assumed will increase more if the draft reduction is increased further, leading to a maximum response for the reduced draft case at an even lower wave period.

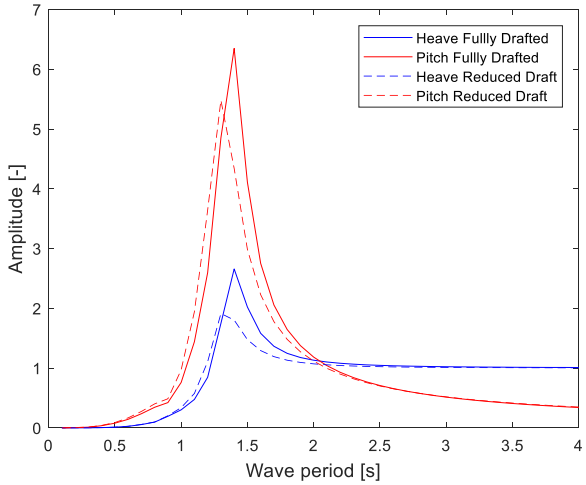

Figure 33 - Response amplitude operators (RAO) for the connected models fully drafted and at a reduced draft, in the heave translation and the pitch rotation. The plotted data are obtained from simulations performed in SESAM.

4.2.4. Wave parameters used in the experiments

The experiments are executed in different sea-states. The connected experiments use a JONSWAP wave spectra and the collision experiments use regular sine waves. The JONSWAP wave spectra data was chosen based on the Buchan Deep metocean data given in [29] and as shown in Figure 34.

H_S (m)	Spectral peak period (T_p) - (s)																					
	2-3	3-4	4-5	5-6	6-7	7-8	8-9	9-10	10-11	11-12	12-13	13-14	14-15	15-16	16-17	17-18	18-19	19-20	20-21	21-22	22-23	Sum
0-1	177	3746	10423	9068	7551	4984	2983	2033	1142	626	309	167	63	38	12	3	4					43329
1-2		57	5281	13966	12849	10034	7653	5074	3720	2476	1254	571	245	109	36	9	3					63337
2-3			32	1413	7085	7423	4826	3338	1985	1397	1132	582	228	125	31	12	7					29616
3-4				4	599	2588	3559	2404	1332	553	388	204	141	63	20	5	2	1	1			11864
4-5					15	168	1046	1398	993	445	152	94	50	22	14	4			1			4402
5-6						5	113	429	497	358	114	57	12	10	5							1600
6-7							3	55	132	166	103	43	13	3	2							520
7-8								2	18	42	57	16	10	4	4							153
8-9									1	6	14	7	7	2	1							38
9-10												1	2									3
10-11											1											1
Sum	177	3803	15736	24451	28099	25202	20183	14733	9820	6069	3524	1742	771	376	125	33	16	1	2	0	0	154863

Figure 34 - JONSWAP wave spectra metocean data from the Buchan Deep [29].

Two significant wave height were chosen, which include a wave height at 3.5 m, and a lower wave height of 1.5 m. Different peak periods were also chosen for each significant wave heights. Table 7

shows the wave parameters used in the experiment for the JONSWAP spectra, both in full-scale and when scaled down to model scale using the relevant Froude scaling relationship as shown in Table 1. The first three wave peak periods for each wave height have a reasonable likelihood of occurring, where the third is approximately at the peak of the simulated heave and pitch response for both the fully drafted and the reduced draft systems. The fourth peak period is approximately where the simulated heave responses converges towards 1. This peak period has a lower likelihood of occurring but will give an indication of the loads between the structures in an extremal case.

Table 7 - Table of the wave parameters for the experiments using a JONSWAP wave spectra.

JONSWAP wave spectra $(\boldsymbol{\gamma = 3.3})$					
Experiment no.	**Full Scale**	**Model Scale**	**Experiment no.**	**Full Scale**	**Model Scale**
	$\boldsymbol{H_s = 1.5\ \mathrm{m}}$	$\boldsymbol{H_s = 0.02\ \mathrm{m}}$		$\boldsymbol{H_s = 3.5\ \mathrm{m}}$	$\boldsymbol{H_s = 0.05\ \mathrm{m}}$
1	$T_P = 6.5$ s	$T_P = 0.77$ s	**5**	$T_P = 6.5$ s	$T_P = 0.77$ s
2	$T_P = 8.5$ s	$T_P = 1.00$ s	**6**	$T_P = 8.5$ s	$T_P = 1.00$ s
3	$T_P = 10.5$ s	$T_P = 1.24$ s	**7**	$T_P = 10.5$ s	$T_P = 1.24$ s
4	$T_P = 16.5$ s	$T_P = 1.94$ s	**8**	$T_P = 16.5$ s	$T_P = 1.94$ s

The collision experiment uses regular sine waves. This is because collisions from releases in different phases are investigated which are not possible when using a wave spectrum. The regular wave parameters are presented Table 8.

Table 8 - Table of the wave parameters for the experiments using regular sine waves

Regular Sine Waves		
Experiment no.	**Full Scale**	**Model Scale**
	$\boldsymbol{H_s = 2.88\ \mathrm{m}}$	$\boldsymbol{H_s = 0.04\ \mathrm{m}}$
9	$T_P = 6.5$ s	$T_P = 0.77$ s
10	$T_P = 8.5$ s	$T_P = 1.00$ s
11	$T_P = 10.5$ s	$T_P = 1.24$ s

It should be noted that the MarinLab wave tank has a limitation of a minimum peak period of 0.7 s as given in [18], hence, the lowest period in the experiments are set to 0.77 s which correlate to a full-scale period of 6.5 s.

4.2.5. Calibration of the wave gauges

As illustrated in the experimental setup in Figure 25, there are seven wave gauges. Wave gauge one and two are in parallel and are connected to different software tools. Wave gauge two are connected to the LabVIEW software and gives the output value in voltage based on the change in resistance in the wave gauge due to the wave oscillations. Wave gauge one, three, four, five, six and seven are

connected to the wave generator and gives the output directly in meter wave amplitude around the zero-crossing.

Due to this configuration, wave gauge two needs to be calibrated to get the output values in the same unit as the other six. This is done by first, running sine waves with wave heights set in the wave generator, then measuring the output values given in voltage. The given input and measured output values are presented in Table 9 and plotted in Figure 35.

Table 9 - Input and output values for the wave gauge calibration

Wave gauge calibration									
Wave amplitude input [m]	0.10	0.15	0.20	0.25	0.30	0.35	0.40	0.45	0.50
Measured output [V]	3.33	2.85	3.36	1.87	1.38	0.89	0.41	-0.07	-0.55

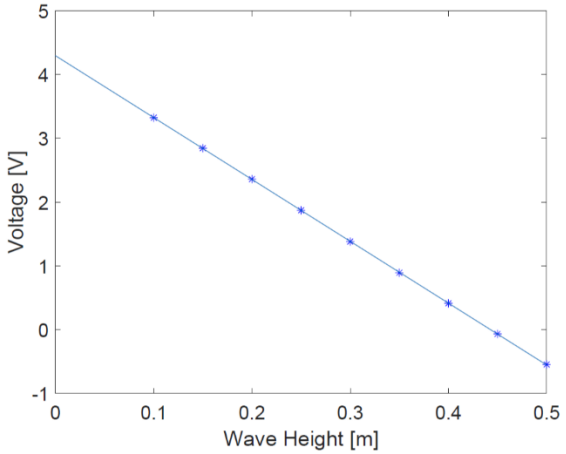

Figure 35 - Wave gauge calibration plot with values as shown in Table 9.

Assuming a linear system, the ideal straight-line slope gradient K is found by using the ideal straight-line formula as shown in Eqn. (28):

$$K = \frac{O_{Max} - O_{MIN}}{I_{MAX} - I_{MIN}} = \frac{3.33\ \mathrm{V} - (-0.55\ \mathrm{V})}{0.10\ \mathrm{m} - 0.50\ \mathrm{m}} = -9.7\ \mathrm{V/m} \tag{28}$$

where O is the measured output and I is the input value. To present the output values from wave gauge two in wave amplitude height, the line-slope intercept, a, is found by taking the mean value of the given measurement. This will then act as the wave oscillation center.

The other six wave gauges are calibrated using the embedded calibration program in the wave generator.

4.2.6. Wave calibration

Each of the waves using the JONSWAP wave specter are calibrated before the experiments are executed. The waves are first made in the software tool, Njord Wave Synthesis, using the wave parameters from experiment 1-8, as shown in Table 7. The wave spectral parameters made also includes a random phase modifier and a repeat time of 25 minutes. The waves are first run for 40 minutes with a result as shown in Figure 36.

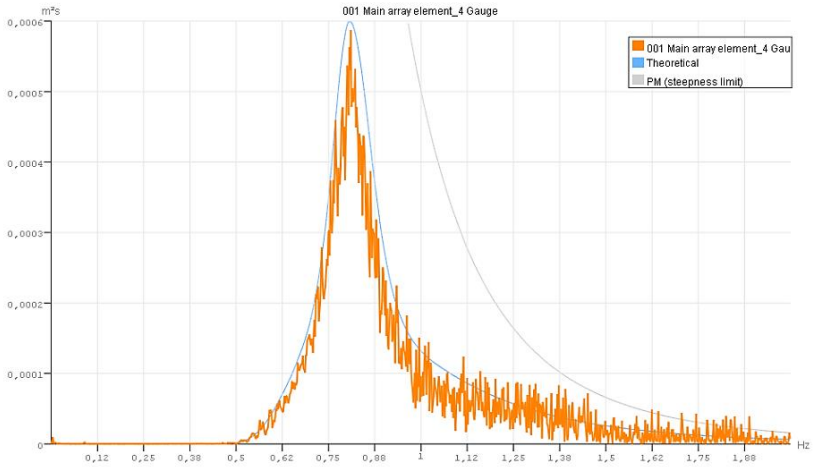

Figure 36 - Screenshot from the software tool Njord Wave Synthesis showing a JONSWAP wave spectrum with $H_s = 0.05\ m$ and $T_p = 1.24\ s$ before calibration with the theoretical curve in blue and the measured energy curve in orange.

After a gain correction is implemented the measured energy spectrum data curve is lifted with a mean value around the theoretical curve as shown in Figure 37.

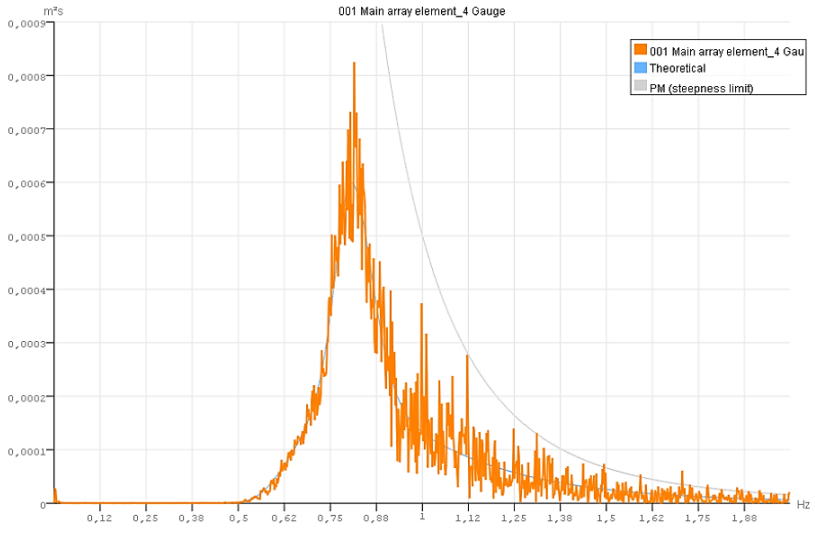

Figure 37 - Screenshot from the software tool Njord Wave Synthesis showing a JONSWAP wave spectrum with $H_s = 0.05\ m$ and $T_p = 1.24\ s$ after calibration with the theoretical curve in blue now beneath the measured energy curve in orange.

4.2.7. Calibration of the load cell rig

The load cell rig is calibrated, both in a hanging and standing position as illustrated in Figure 38. This allows for measuring forces in both tension and compression. Calibration loads of 100 N and 200 N are prepared using a Precisa 24000D SCS scale and applied at different locations on the loading plate, as shown in the figure. In addition to the point loads, the rig is also measured without any applied loads in both positions to get the zero points. The theoretical loads are calculated using the basic static equations for forces and moments. The calibration data are based on an average of data points over a one-minute sampling period with a sampling rate of 2000 per second.

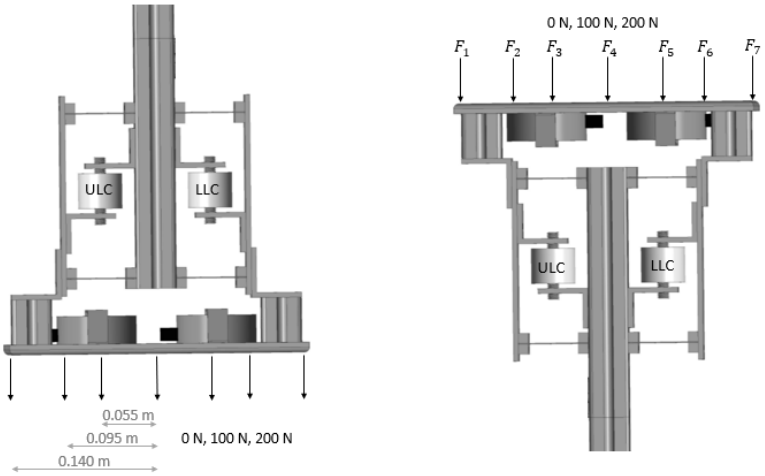

Figure 38 - The load cell rig is calibrated both "hanging" and "standing" as shown in the figure. This allows for measuring forces in both tension and compression. Point loads of 100 N *and 200* N *are measured at different locations in addition to measurements without loads. The upper load cell is given as ULC and the lower load cell as LLC.*

Assuming a linear system, the load cells straight-line slope gradient K is found using a single-degree polynomial function operation in MATLAB. This gives the linear least-squares best fit between the given data points. The line-slope intercept, a at the y-axis, is found as the zero line, (or the oscillation center), when the load cell rig is in an operational position, i.e. when it is in a horizontal position and with the model scaled FOWT attached to it and before the loads from the waves are included. This value may differ slightly as the placement of the scaled FOWT is not completely reproduceable between the different experiments. Especially in the collision experiments.

The first calibration case is for the upper load cell (ULC), as shown in Figure 39, which gives output data in voltage. The ideal straight-line slope gradient is calculated to $\mathrm{K_{UPL_C}} = -0.0165\ \mathrm{V/N}$ and $\mathrm{K_{ULC_T}} = -0.0166\ \mathrm{V/N}$ for the compression and tension cases respectively. This shows a good similarity between the compression and tension cases and a mean straight-line slope gradient of $\mathrm{K_{ULC}} = -0.01655\ \mathrm{V/N}$ is used in the calculations. A goodness of fit test for the polynomial fit gives a RMSE and R-squared for the compression and tension case of $RMSE_{ULC_C} = 0.102\ \mathrm{V/N}$, $RMSE_{ULC_T} =$

0.099 V/N, $R^2_{ULC_C} = 0.996$ and $R^2_{ULC_T} = 0.995$ respectively. This shows that the polynomial fit is good for both tests.

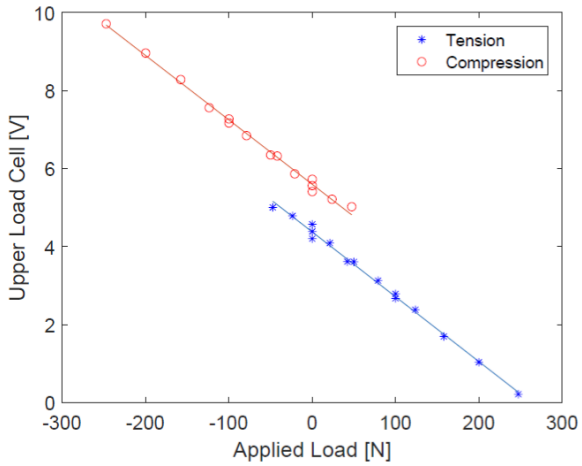

Figure 39 - Upper load cell calibration. The polynomial function calculates the best linear fit between the data points for the calibration when the applied load is placed in the centre and both in tension and compression. The ideal straight-line slope constants are calculated to $K = -0.0165\ V/N$ for the compression case and $K = -0.0166\ V/N$ for the tension case.

Secondly, the lower load cell (LLC) is calibrated as shown in Figure 40. Due to a small mistake in the data collection script in LabVIEW, the output signal is given in pounds. This is converted into Newton by the same procedure as above.

The ideal straight-line slope gradient is calculated to $\mathrm{K_{LLC_C}} = -0.1828\ \mathrm{lbf/N}$ and $\mathrm{K_{LLC_T}} = -0.1855\ \mathrm{lbf/N}$ for the compression and tension cases respectively. This shows a good similarity between the compression and tension cases and a mean straight-line slope gradient of $\mathrm{K_{LLC}} = -0.18415\ \mathrm{lbf/N}$ is used in the calculations. A goodness of fit test for the polynomial fit gives a RMSE and R-squared for the compression and tension case of $RMSE_{ULC_C} = 1.053\ \mathrm{lbf/N}$, $RMSE_{LLC_T} = 1.042\ \mathrm{lbf/N}$, $R^2_{LLC_C} = 0.996$ and $R^2_{LLC_T} = 0.996$ respectively. This shows that this polynomial fit is less accurate, compared to the ULC. The high RMSE indicates that the fit is less good but the R-squared close to 1 indicates that it is a good fit. The reason for these contradictions is uncertain.

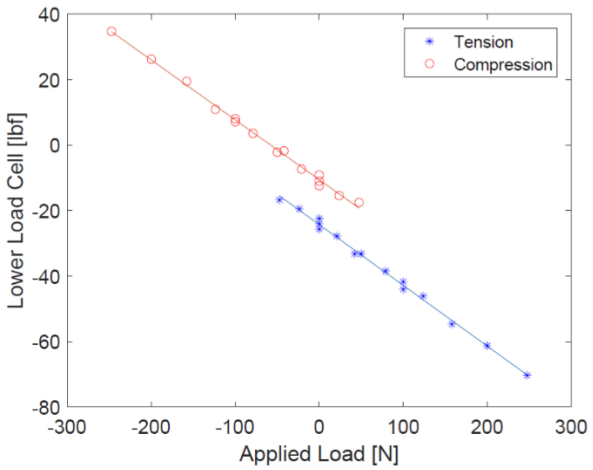

Figure 40 - Lower load cell calibration. The polynomial function calculates the best linear fit between the data points for the calibration when the applied load is placed in the centre and both in tension and compression. The ideal straight-line slope constants are calculated to $K = -0.1828\ lbf/N$ for the compression case and $K = -0.1855\ lbf/N$ for the tension case.

4.3. Experiment execution procedures

In this chapter, the procedures of how the experiments are executed are described.

4.3.1. Connected experiment procedures with the scaled FOWT fully drafted

The experiments where the scaled FOWT is fully drafted and connected to the scaled barge are performed for the sea-states in experiment 1-8 with the given JONSWAP wave parameters as shown in Table 7. Each experiment is run for approximately 20 minutes to develop a full wave spectrum. The first minute of the data, before the waves reach the models, is excluded from the analysis. A few of the test are performed multiple times to investigate the repeatability whilst others were only performed once due to time restrictions in the MarinLab. The load cells in the load cell rig, measure the loads caused by the waves and calculations are preformed convert the signals to newton. Further, the bending moments are calculated around a point P on the barge as shown in Figure 41.

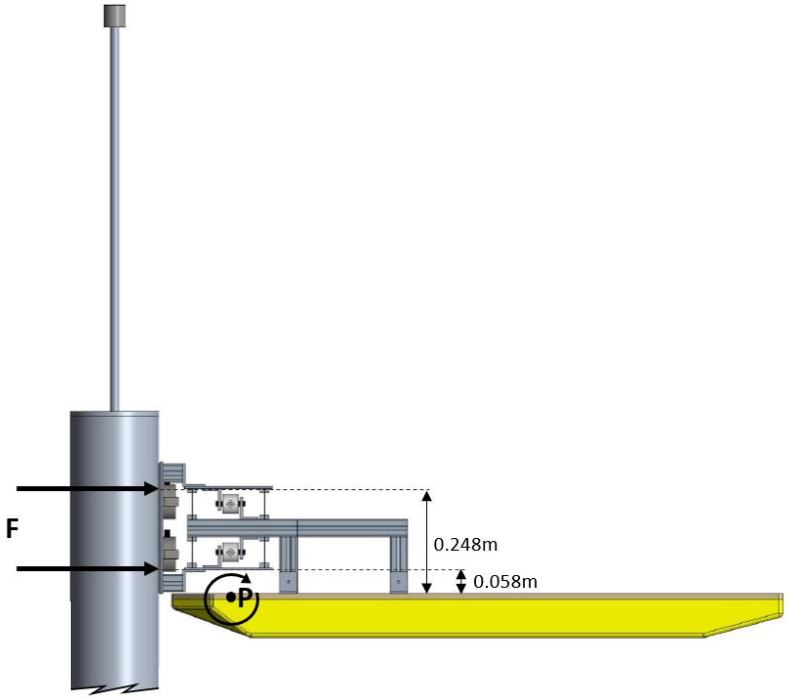

Figure 41 - Bending moments calculated around point P on the barge deck.

The results are presented in a probability density histogram, using 40 bins, and plotted against a normal distribution fit for each sea-state examined. The goodness of the fit is investigated by the chi-squared and RMSE from Eqn. (16) and Eqn. (18) respectively, before the statistical data from the normal fit is presented in tables with their respective mean values, standard deviations and their 95% confidence intervals. Further, the calculated loads are presented for their 99.7% probability interval before the ratio between these are compared between the experiments, and with the reduced draft experiments. This is done by taking the mean of the ratio of the extremities for the respective experiments as shown in Eqn. (29):

$$\lambda_{r_{i-i+1}} = \frac{\frac{Exp_{i+1_{MIN}}}{Exp_{i_{MIN}}} + \frac{Exp_{i+1_{MAX}}}{Exp_{i_{MAX}}}}{2} \tag{29}$$

where $\lambda_{r_{i-i+1}}$ is the ratio between the investigated experiments, $Exp_{i_{MIN}}$ and $Exp_{i+1_{MIN}}$ is experiment i and experiment $i+1$ lower extremities respectively, and $Exp_{i_{MAX}}$ and $Exp_{i+1_{MAX}}$ is experiment i and experiment $i+1$ upper extremities respectively.

Finally, the 99.7% probability interval for each experiment are scaled up to full-scale magnitude using the relevant Froude scale relationship given in Table 1. This is to get an indication of which magnitudes

might be expected from the bending moment in a full-scale case, and which bending moments a full-size support structure may need to compensate for, due to the wave loads in the examined sea states.

4.3.2. Connected experiment procedures with the scaled FOWT at a reduced draft

Before the experiment where the scaled FOWT is connected to the scaled barge at a reduced draft is performed, some of the scaled FOWT mass have to be removed. A total of $6.05\ \mathrm{kg}$ was removed which reduced the draft to approximately $0.86\ \mathrm{m}$ which is approximately an 18% draft reduction. The reason for this particular mass removal was the ballasting configuration of the scaled FOWT. After the draft reduction, the scaled FOWT has a new COG at $0.507\ \mathrm{m}$, which is above the new COB of half the draft, hence, it needs to be connected to the barge to stay upright as the spar-buoy criteria is no longer kept. This gives the load cell rig a new equilibrium offset which is used in the calculations. Both, the new draft and the new COG reduces the distance for the force moments to act. The reduced draft also leads to a proportional increase in height for the top head mass, however, the effect of this change is not investigated further in this project.

As with the fully drafted experiments, also these experiments are performed and calculated with the same conditions as mentioned in section 4.3.1. and compared with the fully drafted results.

4.3.3. Collision experiment

Before the collision experiments are executed the moorings for the scaled FOWT are slightly adjusted so that they are normal to the tank walls. This allows for an equilibrium position close to the scaled barge when the electromagnets on the load cell rig are switched off and prevents the scaled FOWT being pulled away by the moorings after release. It is assumed that this does not affect the connected bodies natural behavior significantly. The electromagnets are programed to release in a specified phase in the wave profile, and after the experiment is executed, they are automatically switched back on and connects to the FOWT at the wanted position. The release occurs after a fully developed wave train has passed, but in due time for the load cell rig to measure the collision forces before the reflecting waves returns from the perforated beach in the wave tank.

The experiments are performed with regular sine waves, given in Table 8, and the release are set at various phases to see if there are significant differences in the measured forces and which phase causes the largest impact forces. Eight phases are investigated for each experiment with a 45 degrees step, starting at the zero up-crossing.

The load cells in the load cell rig, measure the loads caused by the collisions. The net forces from the two load cells are calculated and the impulse peaks are integrated over a time interval varying between $dt = 0.01\ \mathrm{s} - 0.04\ \mathrm{s}$, depending on the duration of the impact, (the width of the peak's curve at the

zero-crossing). The integrations are performed using a trapz function in MATLAB which returns the approximated integral of the impulse peak via the trapezoidal method with unit spacings. An example of the integration is illustrated in Figure 42. The load cells act in compression when exposed to the collision impacts, hence the negative force value. It should be noted that the data points do not necessarily land on the zero line and hence, the magnitude of the impulse loads may differ slightly from their actual value.

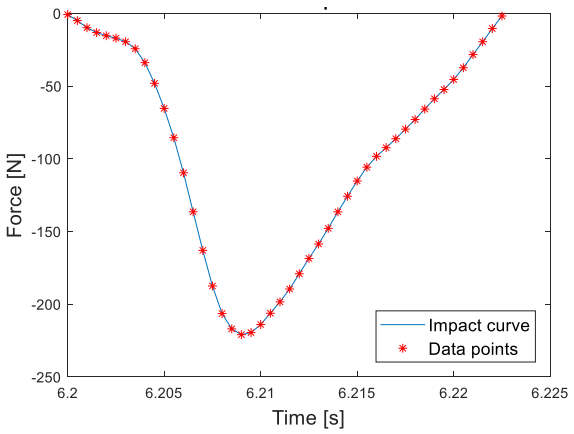

Figure 42 - Example of the integration of the impact force over impact time to find the impulse load. The area under the curve is found using the trapz function in MATLAB, which returns the approximated integral of the impulse peak via the trapezoidal method with unit spacings. The data points are collected from a LabVIEW script with a sampling rate of 2000 measurements per second.

The results are presented in a force vs. time plot which includes the release signal and the absolute values of the integrated impulse loads from the impacts given in $[\mathrm{kg} \cdot \mathrm{m/s}]$. The time from release to impact is calculated and presented in tables next to their respective impulse loads. Further, the results are compared between the experiments different release phases to investigate the differences. Some of the experiments are also performed multiple times, with the same release phase, to investigate the repeatability of the experiments.

5. Results and discussion

In this chapter, the result from the performed experiments are presented with a following discussion. This includes the connected experiments with the scaled FOWT fully drafted, the connected experiments with the scaled FOWT at a reduced draft and the collision experiments.

5.1. Connected experiment with the scaled FOWT fully drafted

The results from the connected experiment with the scaled floating offshore wind turbine fully drafted are presented here. This includes the experiments from experiment 1-8, all which uses a JONSWAP wave spectra with wave parameters as given in Table 7. All values presented before the results are discussed.

5.1.1. Fully drafted experiment 1-4

The measurements from the connected, fully drafted experiments using a JONSWAP wave spectra with wave height $H_S = 0.02\ \mathrm{m}$ and wave periods $T_P = 0.77\ \mathrm{s}, 1.0\ \mathrm{s}, 1.24\ \mathrm{s}, 1.94\ \mathrm{s}$ are calculated and plotted as shown in Figure 43.

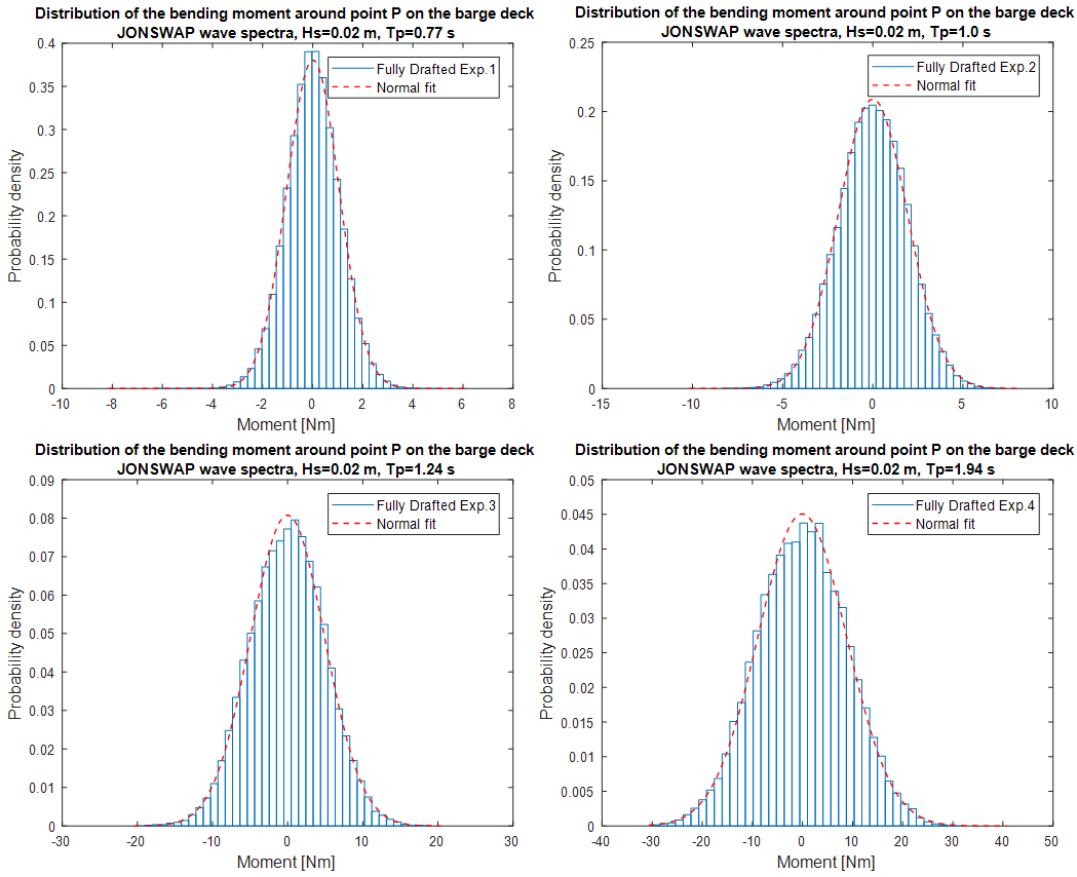

Figure 43 - Bending moment distribution plot from the connected, fully drafted experiment 1-4. The experimental data is plotted in a 40-bin histogram and fitted with a normal distribution curve.

A normal distribution curve is fitted the experimental data which gives a mean value and a standard deviation as presented in Table 10 next to their respective standard errors and confidence interval boundaries. The goodness of the normal distribution fit is also presented in the table as RMSE and chi-squared.

Table 10 - Statistical parameters from the normal distribution curve fit from the connected, fully drafted experiment 1-4.

Statistical parameters from the normal distribution fits from the connected, fully drafted experiment 1-4				
Exp. 1 Hs=0.02 m, Tp=0.77 s			**95% confidence interval boundaries**	
$RMSE = 4.4e-03\ (\mathrm{Nm})^{-1}$	$\chi^2 = 2.3e-04\ (\mathrm{Nm})^{-1}$		**Lower**	**Upper**
Mean [Nm]	$\mu = 0.0079$	$std.error = 0.0007$	0.0065	0.0092
Standard Deviation [Nm]	$\sigma = 1.0474$	$std.error = 0.0005$	1.0465	1.0484
Exp. 2 Hs=0.02 m, Tp=1.0 s			**95% confidence interval boundaries**	
$RMSE = 2.7e-03\ (\mathrm{Nm})^{-1}$	$\chi^2 = 1.1e-04\ (\mathrm{Nm})^{-1}$		**Lower**	**Upper**
Mean [Nm]	$\mu = 0.0030$	$std.error = 0.0013$	0.0005	0.0054
Standard Deviation [Nm]	$\sigma = 1.9081$	$std.error = 0.0009$	1.9064	1.9099
Exp. 3 Hs=0.02 m, Tp=1.24 s			**95% confidence interval boundaries**	
$RMSE = 1.6e-03\ (\mathrm{Nm})^{-1}$	$\chi^2 = 1.1e-04\ (\mathrm{Nm})^{-1}$		**Lower**	**Upper**
Mean [Nm]	$\mu = -0.0211$	$std.error = 0.0033$	-0.0275	-0.0148
Standard Deviation [Nm]	$\sigma = 4.9366$	$std.error = 0.0023$	4.9321	4.9411
Exp. 4 Hs=0.02 m, Tp=1.94 s			**95% confidence interval boundaries**	
$RMSE = 1.0e-03\ (\mathrm{Nm})^{-1}$	$\chi^2 = 7.3e-05\ (\mathrm{Nm})^{-1}$		**Lower**	**Upper**
Mean [Nm]	$\mu = -0.0592$	$std.error = 0.0058$	-0.0706	-0.0477
Standard Deviation [Nm]	$\sigma = 8.8523$	$std.error = 0.0041$	8.8442	8.8604

A comparison of the normal fit for the four experiments is shown in Figure 44.

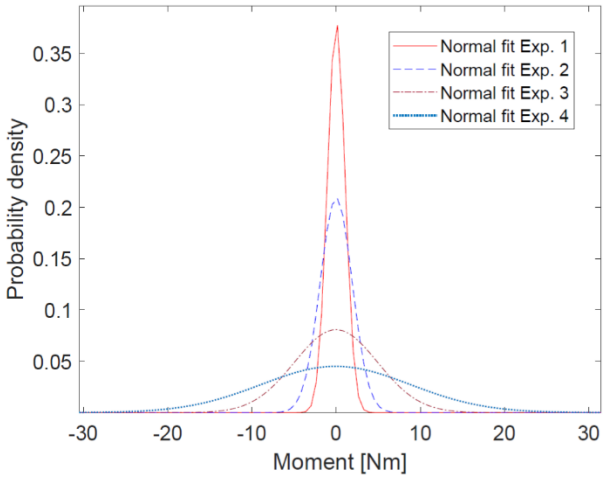

Figure 44 - Comparison of the normal distribution fit from the fully drafted experiment 1-4.

The 99.7% probability intervals are calculated using the empirical rule shown in Figure 15. The results from these calculations are shown in Table 11.

Table 11 - The 99.7% probability intervals from the connected, fully drafted experiment 1-4.

The 99.7% probability load intervals from the fully drafted experiment 1-4	
Experiment	**Probability interval [Nm]** $\boldsymbol{\mu \pm 3\sigma}$
Exp. 1 Hs=0.02 m, Tp=0.77 s	$[-3.13\,, 3.15]$
Exp. 2 Hs=0.02 m, Tp=1.0 s	$[-5.72\,, 5.73]$
Exp. 3 Hs=0.02 m, Tp=1.24 s	$[-14.83\,, 14.79]$
Exp. 4 Hs=0.02 m, Tp=1.94 s	$[-26.62\,, 26.50]$

From the 99.7% probability interval in Table 11, the results are scaled up to full-scale magnitude using the relevant Froude scaling relationship as given in Table 1. The full-scale 99.7% probability intervals are presented in Table 12.

Table 12 - The full-scale 99.7% probability intervals from the connected, fully drafted experiment 1-4. The magnitudes are scaled up using the relevant Froude scaling relationship given in Table 1.

The full-scale 99.7% probability load intervals from the fully drafted experiment 1-4	
Experiment	**Probability interval [Nm]** $\boldsymbol{\mu \pm 3\sigma}$
Exp. 1	$[-8.63e+07\,, 8.68e+07]$
Exp. 2	$[-1.58e+08\,, 1.58e+08]$
Exp. 3	$[-4.09e+08\,, 4.07e+08]$
Exp. 4	$[-7.32e+08\,, 7.31e+08]$

The needed thickness of a single solid squared cross-sectional support beam to withstand the full-scale bending moments is calculated for Exp. 1 and Exp. 4, using the Eqn. (20), derived for the cross-sectional height h when $h = w$ and $\sigma = \sigma_{yield}$, assuming a steel with yield strength of $350\ \mathrm{MPa}$. The results from these calculations are shown in Eqn. (30) and Eqn. (31) for Exp. 1 and Exp. 4 respectively:

$$h = \sqrt[3]{\frac{|M| \cdot 6}{\sigma_{yield}}} = \sqrt[3]{\frac{8.68 \cdot 10^7\ \mathrm{Nm} \cdot 6}{350 \cdot 10^6\ \mathrm{Pa}}} = 1.14\ \mathrm{m} \tag{30}$$

$$h = \sqrt[3]{\frac{|M| \cdot 6}{\sigma_{yield}}} = \sqrt[3]{\frac{7.32 \cdot 10^8\ \mathrm{Nm} \cdot 6}{350 \cdot 10^6\ \mathrm{Pa}}} = 2.32\ \mathrm{m} \tag{31}$$

Experiment 3 is executed three times to investigate the repeatability in the experiments. The two latter executions are performed at a later time. The results show good similarity between the three experiments as can be observed when comparing Exp. 3 from Figure 43 and Exp. 3_2 and Exp. 3_3 from Figure 45.

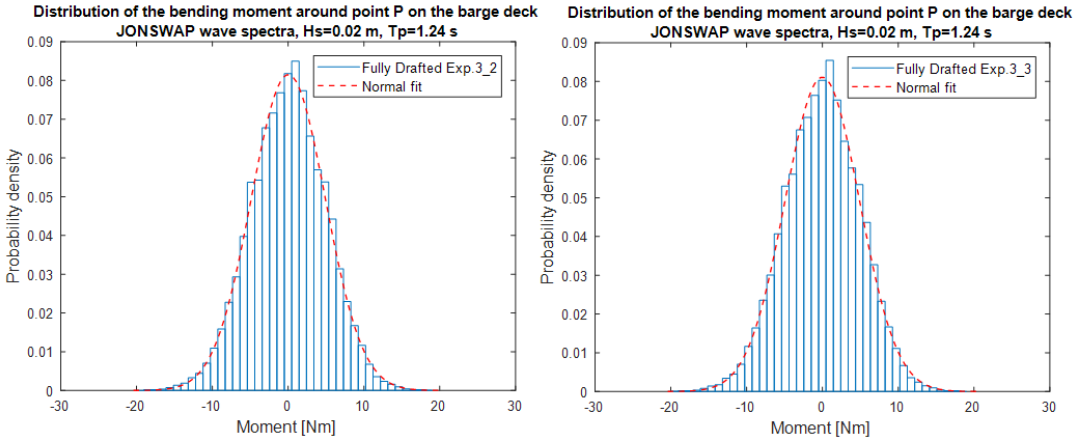

Figure 45 - Bending moment distribution plot from the connected, fully drafted repeatability experiment 3_2 and 3_3. The experimental data is plotted in a histogram and fitted with a normal distribution curve. The two plots show good similarity when compared with each other, and when compared with the first experiment 3 plot.

The same is seen when comparing the standard deviation from the statistical data between the experiments in Table 11 and Table 13. The 99.7% probability intervals are calculated to $[-14.66\ \text{Nm}, 14.70\ \text{Nm}]$ and $[-14.77\ \text{Nm}, 14.74\ \text{Nm}]$ for experiment 3_2 and 3_3 respectively.

Table 13 - Statistical parameters from the normal distribution curve fit from the connected, fully drafted experiment 3_2 and 3_3. The statistical data show good similarity when comparing the standard deviation with each other, and when compared with the standard deviation from the first experiment 3 statistical data.

Statistical parameters from the normal distribution of the connected, fully drafted experiment 3_2 and 3_3. Repeatability check.				
Exp. 3_2 Hs=0.02 m, Tp=1.24 s			**95% confidence interval boundaries**	
$RMSE = 1.8e-03\ (\text{Nm})^{-1}$	$\chi^2 = 1.3e-04\ (\text{Nm})^{-1}$		**Lower**	**Upper**
Mean [Nm] Exp. 3_2	$\mu = 0.0208$	$std.error = 0.0032$	0.0145	0.0271
Standard Deviation [Nm]	$\sigma = 4.8947$	$std.error = 0.0023$	4.8902	4.8992
Exp. 3_3 Hs=0.02 m, Tp=1.24 s			**95% confidence interval boundaries**	
$RMSE = 1.9e-03\ (\text{Nm})^{-1}$	$\chi^2 = 1.5e-04\ (\text{Nm})^{-1}$		**Lower**	**Upper**
Mean [Nm]	$\mu = -0.0155$	$std.error = 0.0032$	-0.0218	-0.0091
Standard Deviation [Nm]	$\sigma = 4.9194$	$std.error = 0.0023$	4.9149	4.9239

5.1.2. Fully drafted experiment 5-8

The measurements from the connected, fully drafted experiments using a JONSWAP wave spectra with wave height $H_S = 0.05\ \text{m}$ and wave periods $T_P = 0.77\ \text{s}, 1.0\ \text{s}, 1.24\ \text{s}, 1.94\ \text{s}$ are calculated and plotted as shown in Figure 46. It should be noted that the data from experiment 8 contain less samples the rest of the experiments. This experiment was aborted due to safety reasons as the measured loads were close to one of the load cells maximum. The data contains around a 5 minutes sampling which is approximately 75% less than the other experiments.

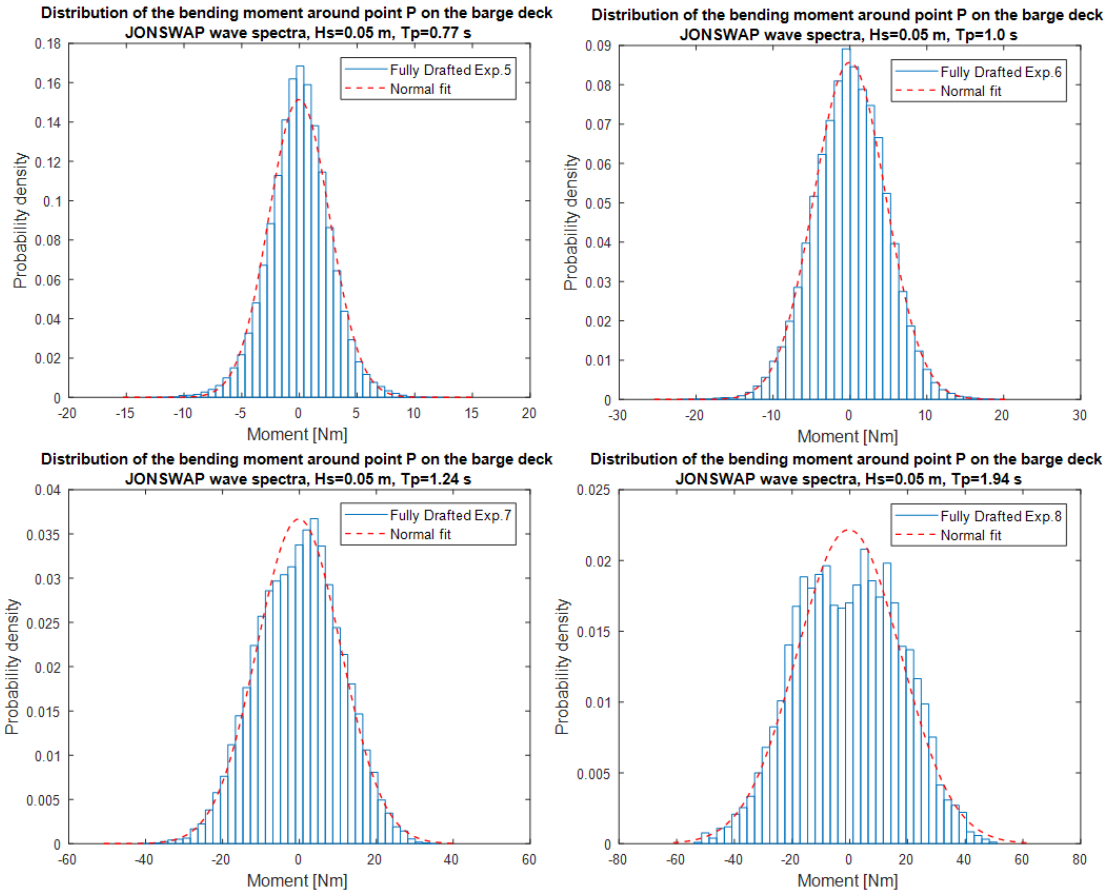

Figure 46 - Bending moment distribution plot from the connected, fully drafted experiment 5-8. The experimental data is plotted in a 40-bin histogram and fitted with a normal distribution curve.

A normal distribution curve is fitted the experimental data which gives a mean value and a standard deviation as presented in Table 14 next to their respective standard errors and confidence interval boundaries. The goodness of the normal distribution fit is also presented in the table as RMSE and chi-squared.

‘

Table 14 - Statistical parameters from the normal distribution curve fit from the connected, fully drafted experiment 5-8.

Statistical parameters from the normal distribution fits from the connected, fully drafted experiment 5-8				
Exp. 5 Hs=0.05 m, Tp=0.77 s			**95% confidence interval boundaries**	
$RMSE = 5.4e-03\ (\mathrm{Nm})^{-1}$	$\chi^2 = 7.9e-04\ (\mathrm{Nm})^{-1}$		**Lower**	**Upper**
Mean [Nm]	$\mu = -0.0179$	$std.error = 0.0017$	-0.0213	-0.0144
Standard Deviation [Nm]	$\sigma = 2.6321$	$std.error = 0.0012$	2.6297	2.6345
Exp. 6 Hs=0.05 m, Tp=1.0 s			**95% confidence interval boundaries**	
$RMSE = 1.3\,e-03(\mathrm{Nm})^{-1}$	$\chi^2 = 7.2e-05\ (\mathrm{Nm})^{-1}$		**Lower**	**Upper**
Mean [Nm]	$\mu = -0.0166$	$std.error = 0.0031$	-0.0227	-0.0106
Standard Deviation [Nm]	$\sigma = 4.6522$	$std.error = 0.0022$	4.6479	4.6564
Exp. 7 Hs=0.05 m, Tp=1.24 s			**95% confidence interval boundaries**	
$RMSE = 1.4e-03\ (\mathrm{Nm})^{-1}$	$\chi^2 = 1.9e-04\ (\mathrm{Nm})^{-1}$		**Lower**	**Upper**
Mean [Nm]	$\mu = -0.1464$	$std.error = 0.0071$	-0.1604	-0.1324
Standard Deviation [Nm]	$\sigma = 10.8717$	$std.error = 0.0051$	10.8618	10.8816
Exp. 8 Hs=0.05 m, Tp=1.94 s			**95% confidence interval boundaries**	
$RMSE = 2.0e-03\ (\mathrm{Nm})^{-1}$	$\chi^2 = 4.8e-04\ (\mathrm{Nm})^{-1}$		**Lower**	**Upper**
Mean [Nm]	$\mu = -0.3546$	$std.error = 0.0224$	-0.3985	-0.3108
Standard Deviation [Nm]	$\sigma = 17.9865$	$std.error = 0.0158$	17.9556	18.0176

A comparison of the normal fit for the four experiments is shown in Figure 47.

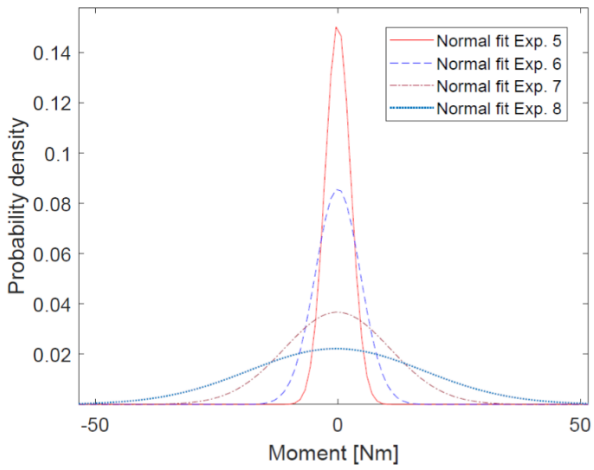

Figure 47 - Comparison of the normal distribution fit from the fully drafted experiment 5-8.

The 99.7% probability intervals are calculated using the empirical rule shown in Figure 15. The results from these calculations are shown in Table 15.

Table 15 - The 99.7% probability intervals from the connected, fully drafted experiment 5-8.

The 99.7% probability load intervals from the fully drafted experiment 5-8	
Experiment	**Probability interval [Nm]** $\boldsymbol{\mu \pm 3\sigma}$
Exp. 5 Hs=0.05 m, Tp=0.77 s	$[-7.91\,, 7.88]$
Exp. 6 Hs=0.05 m, Tp=1.0 s	$[-13.97\,, 13.94]$
Exp. 7 Hs=0.05 m, Tp=1.24 s	$[-32.76\,, 32.47]$
Exp. 8 Hs=0.05 m, Tp=1.94 s	$[-54.31\,, 53.61]$

From the 99.7% probability interval in Table 15, the results are scaled up to full-scale magnitude using the relevant Froude scaling relationship as given in Table 1. The full-scale 99.7% probability intervals are presented in Table 16.

Table 16 - The full-scale 99.7% probability intervals from the connected, fully drafted experiment 5-8. The magnitudes are scaled up using the relevant Froude scaling relationship given in Table 1.

The full-scale 99.7% probability load intervals from the fully drafted experiment 5-8	
Experiment	**Probability interval [Nm]** $\boldsymbol{\mu \pm 3\sigma}$
Exp. 5	$[-2.18e+08\,, 2.17e+08]$
Exp. 6	$[-3.85e+08\,, 3.84e+08]$
Exp. 7	$[-9.02e+08\,, 8.94e+08]$
Exp. 8	$[-1.50e+09\,, 1.48e+09]$

The needed thickness of a single solid squared cross-sectional support beam to withstand the full-scale force moments is calculated for Exp. 5 and Exp. 8, using the Eqn. (20), derived for the cross-sectional height h when $h = w$ and $\sigma = \sigma_{yield}$, assuming a steel with yield strength of $350\ \mathrm{MPa}$. The results from these calculations are shown in Eqn. (32) and Eqn. (33) for Exp. 5 and Exp. 8 respectively:

$$h = \sqrt[3]{\frac{|M| \cdot 6}{\sigma_{yield}}} = \sqrt[3]{\frac{2.18 \cdot 10^8\ \mathrm{Nm} \cdot 6}{350 \cdot 10^6\ \mathrm{Pa}}} = 1.55\ \mathrm{m} \tag{32}$$

$$h = \sqrt[3]{\frac{|M| \cdot 6}{\sigma_{yield}}} = \sqrt[3]{\frac{1.5 \cdot 10^9\ \mathrm{Nm} \cdot 6}{350 \cdot 10^6\ \mathrm{Pa}}} = 2.95\ \mathrm{m} \tag{33}$$

5.1.3. Discussing the results from the connected, fully drafted experiments

When analysing the normal curve fit for the presented experiments, the data shows a good fit for all experiments. With an RMSE ranging from $1.0 \cdot 10^{-3}\ (\mathrm{Nm})^{-1}$ to $5.4 \cdot 10^{-3}\ (\mathrm{Nm})^{-1}$ and a Chi-squared ranging from $7.2 \cdot 10^{-5}\ (\mathrm{Nm})^{-1}$ to $7.8 \cdot 10^{-4}\ (\mathrm{Nm})^{-1}$ between the eight experiments, as shown in

Table 10 and Table 14, the statistical data from the curve fit may be assumed to be satisfactory accurate. When observing the curve fit from the plots in Figure 43 and Figure 46, all fits looks good, but with Exp. 5, Exp. 7 and Exp. 8 having the least good fit. This seems to correlate when comparing all the RMSE and chi-squared values.

For the 95% confidence interval boundaries, the results show that all the mean values and all the standard deviations found, lies within their respective intervals. However, for the repeatability tests there is only the mean value from Exp.3 and Exp. 3_3 which lies within one another's confidence boundaries.

When comparing the 99.7% probability intervals from experiment 1-4, an increase in the loads are observed as shown in Table 11 and illustrated in Figure 48. From Exp. 1 to Exp. 2, where the wave period is increased from 0.77 s to 1.00 s respectively, the loads increases with a ratio of approximately $\lambda_{r_{1-2}} = 1.79$. From Exp. 2 to Exp. 3, where the wave period is increased from 1.00 s to 1.24 s respectively, the loads increases with a ratio of approximately $\lambda_{r_{2-3}} = 2.59$. When comparing Exp. 3 to Exp. 4, where the wave period is increased from 1.24 s to 1.94 s respectively, the loads increases with a ratio of approximately $\lambda_{r_{3-4}} = 1.82$.

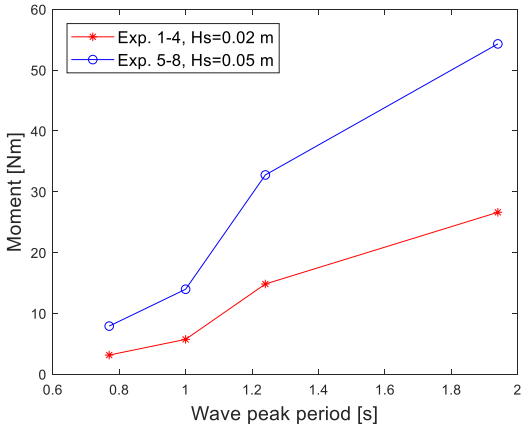

Figure 48 - Bending moments from the 99.7% probability interval plotted against wave period for the fully drafted experiments. As can be observed in the figure, the loads increase with the highest ratio when the peak period is increased from $T_P = 1.0\ s$ to $T_P = 1.24\ s$.

Similar observations are made for the experiment 5-8 comparison as shown in Table 15 and Figure 48. Also, here the load ratio increases with approximately $\lambda_{r_{5-6}} = 1.65$, $\lambda_{r_{6-7}} = 2.34$ and $\lambda_{r_{7-8}} = 1.77$ between experiment 5-6, experiment 6-7, and experiment 7-8 respectively.

As observed from these ratios the loads increase fastest when the peak period is increased from 1.0 s to 1.24 s. This is expected and correlates with the RAO's found for the fully drafted connected system as illustrated in Figure 33. As observed in that figure, the responses from heave and pitch increases rapidly from approximately $t = 0.9$ s and peaks at $t = 1.4$ s before it decreases again. From the decay

tests, the connected bodies indicate an underdamped system which also may explain the rapidly increasing loads as the system are not able to dampen out its motions to a significant degree. This may be due to the simplifications done in the modeling process of the scaled FOWT, where the coned part was left out. It is assumed that the coned geometry would dampen the heave and pitch responses, but as to which degree is uncertain. Another possible solution to control the rapidly increasing loads could be to implement the system with a structure which would increase the damping ratio.

When comparing the experiments with the same wave period, but different wave height the loads increases with a ratio of approximately $\lambda_{r_{1-5}} = 2.51$ between Exp. 1 and Exp. 5, $\lambda_{r_{2-6}} = 2.44$ between Exp. 2 and Exp. 6, $\lambda_{r_{3-7}} = 2.20$ between Exp. 3 and Exp. 7, and finally $\lambda_{r_{4-8}} = 2.03$ between Exp. 4 and Exp. 8. This indicates that, when the wave height is increased from $0.02\ \mathrm{m}$ to $0.05\ \mathrm{m}$, the loads increases more rapidly for the shorter wave periods compared with the longer.

It should be noted that during experiment 5-8, water was observed on the barge deck which may have damped the system's motions and hence, the measured loads from these experiments might be lower than they should be.

Experiment 3 were executed three times to investigate the repeatability in the performed experiments. These three experiments show good similarity with a ratio of $\lambda_{r_{3-3\_2}} = 1.009$, $\lambda_{r_{3-3\_3}} = 1.003$ and $\lambda_{r_{3\_3-3\_2}} = 1.005$ between Exp. 3 and Exp. 3_2, Exp. 3 and Exp. 3_3, and Exp. 3_3 and Exp. 3_2 respectively.

When the 99.7% probability intervals are scaled up to full-scale, the extremities of the bending moments range from $8.68 \cdot 10^7\ \mathrm{Nm}$ to $1.50 \cdot 10^9\ \mathrm{Nm}$. These values are only meant as an indication of which loads might be expected by the full-scale constructions, due to the wave loads in the given sea-states. This is because the geometric similarity between the scaled FOWT and the full-scale structure is not completely obtained and that the viscous effects are scaled using the Froude scaling, which may give an incorrect viscous magnitude, as explained in chapter 2.1.

To get an indication of which size a support structure would need to be to withstand the bending stresses caused by the full-scale bending moments, a single solid square cross-sectional steel beam thickness was found for the extremities of the experiments. The thickness ranges from $1.14\ \mathrm{m}$ to $2.32\ \mathrm{m}$ between experiment 1-4 and $1.55\ \mathrm{m}$ to $2.95\ \mathrm{m}$ between experiment 5-8. This indicates that the needed thickness of the support structure is more exposed to the overall change in the peak period than to the change in wave height, which are both increased by a factor of approximately 2.5.

It should be noted that a full-size support structure would also need to compensate other environmental loads such as current and wind loads where, especially the latter, is assumed to contribute significantly to the bending moment.

5.2. Connected experiment with the scaled FOWT at a reduced draft

The results from the connected experiment with the scaled floating offshore wind turbine at a reduced draft are presented here. This includes the experiments from experiment 1-8, all which uses a JONSWAP wave spectra with wave parameters as given in Table 7. All values presented before the results are discussed.

5.2.1. Reduced draft experiment 1-4

The measurements from the connected, reduced draft experiments using a JONSWAP wave spectra with wave height $H_S = 0.02$ m and wave periods $T_P = 0.77$ s, 1.0 s, 1.24 s, 1.94 s are calculated and plotted as shown in Figure 49.

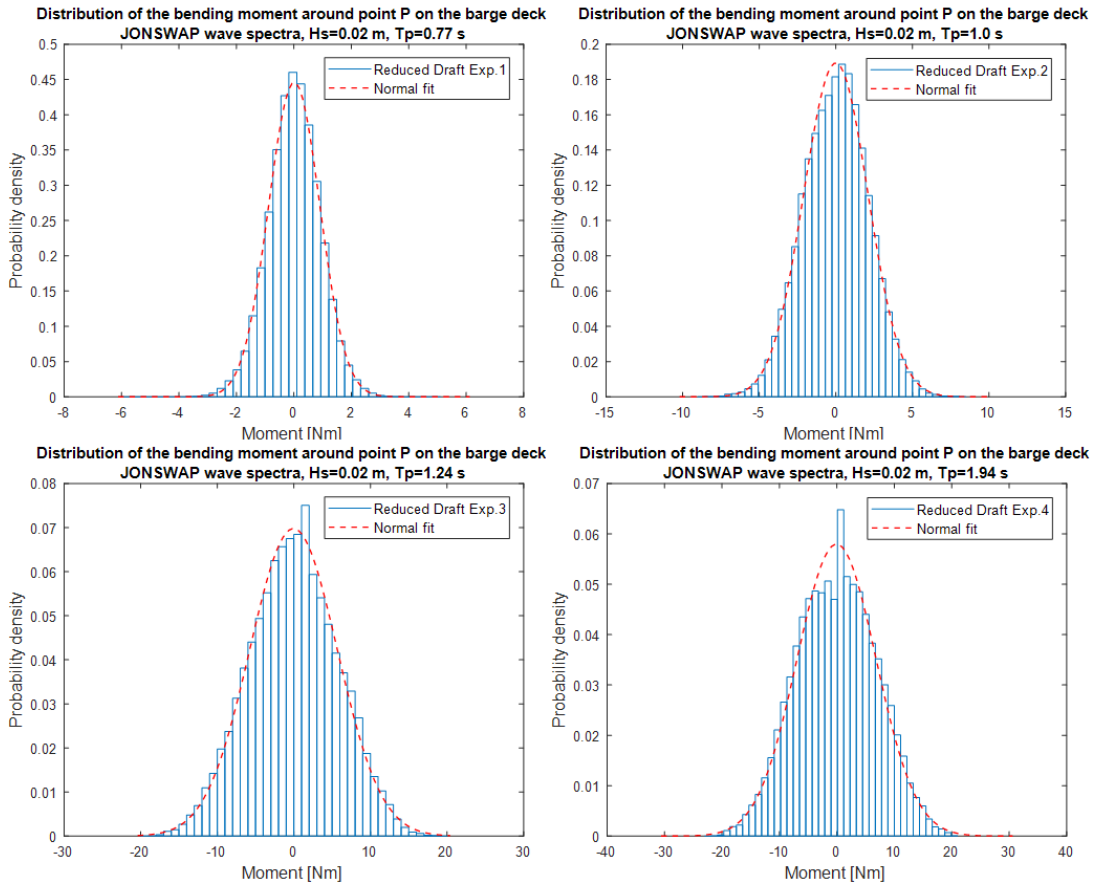

Figure 49 - Bending moment distribution plot from the connected, reduced draft experiment 1-4. The experimental data is plotted in a 40-bin histogram and fitted with a normal distribution curve.

A normal distribution curve is fitted the experimental data which gives a mean value and a standard deviation as presented in Table 17 next to their respective standard errors and confidence interval

boundaries. The goodness of the normal distribution fit is also presented in the table as RMSE and chi-squared.

Table 17 - Statistical parameters from the normal distribution curve fit from the connected, reduced draft experiment 1-4.

Statistical parameters from the normal distribution fits from the connected, reduced draft experiment 1-4				
Exp. 1 Hs=0.02 m, Tp=0.77 s			**95% confidence interval boundaries**	
$RMSE = 5.2e-03\ (\mathrm{Nm})^{-1}$	$\chi^2 = 2.7e-04\ (\mathrm{Nm})^{-1}$		**Lower**	**Upper**
Mean [Nm]	$\mu = 0.0133$	$std.error = 0.0006$	0.0121	0.0144
Standard Deviation [Nm]	$\sigma = 0.8942$	$std.error = 0.0004$	0.8934	0.8950
Exp. 2 Hs=0.02 m, Tp=1.0 s			**95% confidence interval boundaries**	
$RMSE = 4.0e-03\ (\mathrm{Nm})^{-1}$	$\chi^2 = 3.4e-04\ (\mathrm{Nm})^{-1}$		**Lower**	**Upper**
Mean [Nm]	$\mu = -0.0007$	$std.error = 0.0014$	-0.0034	0.0020
Standard Deviation [Nm]	$\sigma = 2.1061$	$std.error = 0.0010$	2.1042	2.1080
Exp. 3 Hs=0.02 m, Tp=1.24 s			**95% confidence interval boundaries**	
$RMSE = 2.4e-03\ (\mathrm{Nm})^{-1}$	$\chi^2 = 2.6e-04\ (\mathrm{Nm})^{-1}$		**Lower**	**Upper**
Mean [Nm]	$\mu = -0.0472$	$std.error = 0.0038$	-0.0546	-0.0398
Standard Deviation [Nm]	$\sigma = 5.7183$	$std.error = 0.0027$	5.7131	5.7236
Exp. 4 Hs=0.02 m, Tp=1.94 s			**95% confidence interval boundaries**	
$RMSE = 3.7e-03\ (\mathrm{Nm})^{-1}$	$\chi^2 = 7.3e-04\ (\mathrm{Nm})^{-1}$		**Lower**	**Upper**
Mean [Nm]	$\mu = -0.0538$	$std.error = 0.0045$	-0.0627	-0.0449
Standard Deviation [Nm]	$\sigma = 6.8831$	$std.error = 0.0032$	6.8768	6.8894

A comparison of the normal fit for the four experiments is shown in Figure 50.

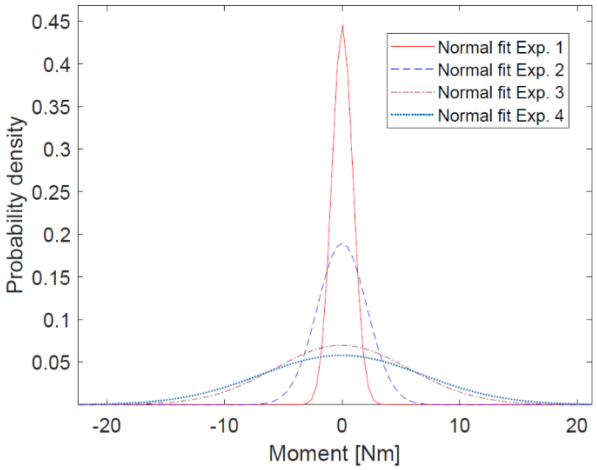

Figure 50 - Comparison of the normal distribution fit from the reduced draft experiment 1-4.

The 99.7% probability intervals are calculated using the empirical rule shown in Figure 15. The results from these calculations are shown in Table 18.

Table 18 - The 99.7% probability intervals from the connected, reduced draft experiment 1-4.

The 99.7% probability load intervals from the reduced draft experiment 1-4	
Experiment	**Probability interval [Nm]** $\boldsymbol{\mu \pm 3\sigma}$
Exp. 1 **Hs=0.02 m, Tp=0.77 s**	$[-2.67\,, 2.70]$
Exp. 2 **Hs=0.02 m, Tp=1.0 s**	$[-6.32\,, 6.32]$
Exp. 3 **Hs=0.02 m, Tp=1.24 s**	$[-17.20\,, 17.11]$
Exp. 4 **Hs=0.02 m, Tp=1.94 s**	$[-20.70\,, 20.60]$

From the 99.7% probability interval in Table 18, the results are scaled up to full-scale magnitude using the relevant Froude scaling relationship as given in Table 1. The full-scale 99.7% probability intervals are presented in Table 19.

Table 19 - The full-scale 99.7% probability intervals from the connected, reduced draft experiment 1-4. The magnitudes are scaled up using the relevant Froude scaling relationship given in Table 1.

The full-scale 99.7% probability load intervals from the reduced draft experiment 1-4	
Experiment	**Probability interval [Nm]** $\boldsymbol{\mu \pm 3\sigma}$
Exp. 1	$[-7.35e+07\,, 7.43e+07]$
Exp. 2	$[-1.74+08\,, 1.74e+08]$
Exp. 3	$[-4.74e+08\,, 4.71e+08]$
Exp. 4	$[-5.70e+08\,, 5.67e+08]$

The needed thickness of a single solid squared cross-sectional support beam to withstand the full-scale force moments is calculated for Exp. 1 and Exp. 4, using the Eqn. (20), derived for the cross-sectional height h when $h = w$ and $\sigma = \sigma_{yield}$, assuming a steel with yield strength of $350\ \mathrm{MPa}$. The results from these calculations are shown in Eqn. (34) and Eqn. (35) for Exp. 1 and Exp. 4 respectively:

$$h = \sqrt[3]{\frac{|M| \cdot 6}{\sigma_{yield}}} = \sqrt[3]{\frac{7.43 \cdot 10^7\ \mathrm{Nm} \cdot 6}{350 \cdot 10^6\ \mathrm{Pa}}} = 1.08\ \mathrm{m} \tag{34}$$

$$h = \sqrt[3]{\frac{|M| \cdot 6}{\sigma_{yield}}} = \sqrt[3]{\frac{5.70 \cdot 10^8\ \mathrm{Nm} \cdot 6}{350 \cdot 10^6\ \mathrm{Pa}}} = 2.14\ \mathrm{m} \tag{35}$$

5.2.5. Reduced draft experiment 5-8

The measurements from the connected, reduced draft experiments using a JONSWAP wave spectra with wave height $H_S = 0.05\ \mathrm{m}$ and wave periods $T_P = 0.77\ \mathrm{s}, 1.0\ \mathrm{s}, 1.24\ \mathrm{s}, 1.94\ \mathrm{s}$ are calculated and plotted as shown in Figure 51.

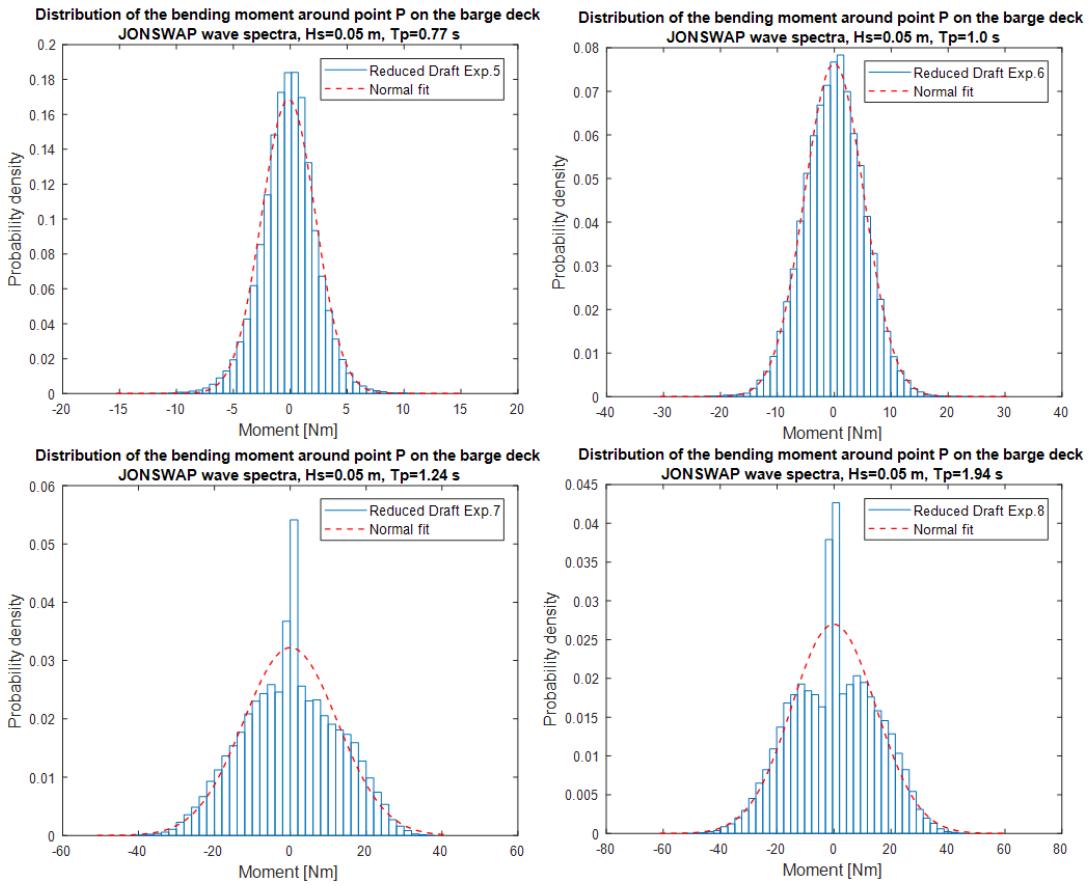

Figure 51 - Bending moment distribution plot from the connected, reduced draft experiment 5-8. The experimental data is plotted in a 40-bin histogram and fitted with a normal distribution curve.

A normal distribution curve is fitted the experimental data which gives a mean value and a standard deviation as presented in Table 20 next to their respective standard errors and confidence interval boundaries. The goodness of the normal distribution fit is also presented in the table as RMSE and chi-squared.

Table 20 - Statistical parameters from the normal distribution curve fit from the connected, reduced draft experiment 5-8.

Statistical parameters from the normal distribution fits from the connected, reduced draft experiment 5-8				
Exp. 5 Hs=0.05 m, Tp=0.77 s			**95% confidence interval boundaries**	
$RMSE = 7.0e-03 (\mathrm{Nm})^{-1}$	$\chi^2 = 1.2e-03\ (\mathrm{Nm})^{-1}$		**Lower**	**Upper**
Mean [Nm]	$\mu = -0.1504$	$std.error = 0.0016$	-0.1535	-0.1472
Standard Deviation [Nm]	$\sigma = 2.3634$	$std.error = 0.0011$	2.3612	2.3656
Exp. 6 Hs=0.05 m, Tp=1.0 s			**95% confidence interval boundaries**	
$RMSE = 1.0e-03\ (\mathrm{Nm})^{-1}$	$\chi^2 = 5.2e-05\ (\mathrm{Nm})^{-1}$		**Lower**	**Upper**
Mean [Nm]	$\mu = -0.0171$	$std.error = 0.0034$	-0.0239	-0.0104
Standard Deviation [Nm]	$\sigma = 5.2175$	$std.error = 0.0024$	5.2128	5.2223
Exp. 7 Hs=0.05 m, Tp=1.24 s			**95% confidence interval boundaries**	
$RMSE = 4.4e-03\ (\mathrm{Nm})^{-1}$	$\chi^2 = 2.0e-03\ (\mathrm{Nm})^{-1}$		**Lower**	**Upper**
Mean [Nm]	$\mu = 0.0496$	$std.error = 0.0082$	0.0336	0.0656
Standard Deviation [Nm]	$\sigma = 12.3777$	$std.error = 0.0058$	12.3664	12.3890
Exp. 8 Hs=0.05 m, Tp=1.94 s			**95% confidence interval boundaries**	
$RMSE = 4.1e-03\ (\mathrm{Nm})^{-1}$	$\chi^2 = 2.2e-03\ (\mathrm{Nm})^{-1}$		**Lower**	**Upper**
Mean [Nm]	$\mu = -0.1266$	$std.error = 0.0097$	-0.1457	-0.1075
Standard Deviation [Nm]	$\sigma = 14.7763$	$std.error = 0.0069$	14.7628	14.7898

A comparison of the normal fit for the four experiments is shown in Figure 52.

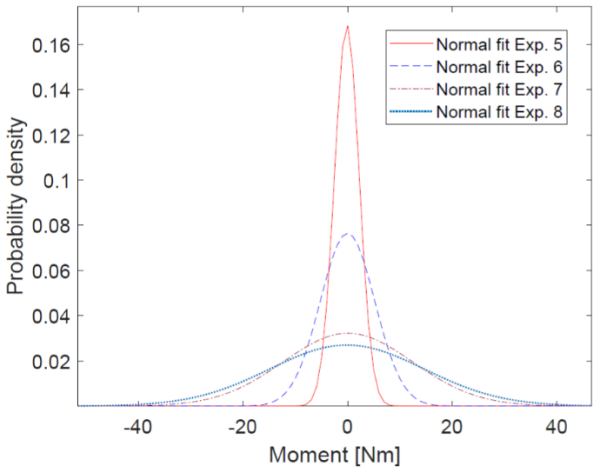

Figure 52 - Comparison of the normal distribution fit from the reduced draft experiment 5-8.

The 99.7% probability intervals are calculated using the empirical rule shown in Table 21. The results from these calculations are shown in Table 15.

Table 21 - The 99.7% probability intervals from the connected, reduced draft experiment 5-8.

The 99.7% probability load intervals the reduced draft experiment 5-8	
Experiment	**Probability interval [Nm]** $\boldsymbol{\mu \pm 3\sigma}$
Exp. 5 Hs=0.05 m, Tp=0.77 s	$[-7.24\,, 6.94]$
Exp. 6 Hs=0.05 m, Tp=1.0 s	$[-15.67\,, 15.64]$
Exp. 7 Hs=0.05 m, Tp=1.24 s	$[-37.08\,, 37.18]$
Exp. 8 Hs=0.05 m, Tp=1.94 s	$[-44.46\,, 44.20]$

From the 99.7% probability interval in Table 21, the results are scaled up to full-scale magnitude using the relevant Froude scaling relationship as given in Table 1. The full-scale 99.7% probability intervals are presented in Table 23.

Table 22 - The full-scale 99.7% probability intervals from the connected, reduced draft experiment 5-8. The magnitudes are scaled up using the relevant Froude scaling relationship given in Table 1.

The full-scale 99.7% probability load intervals from the reduced draft experiment 5-8	
Experiment	**Probability interval [Nm]** $\boldsymbol{\mu \pm 3\sigma}$
Exp. 5	$[-1.99e+08\,, 1.91e+08]$
Exp. 6	$[-4.32e+08\,, 4.31e+08]$
Exp. 7	$[-1.02e+09\,, 1.02e+09]$
Exp. 8	$[-1.22e+09\,, 1.22e+09]$

The needed thickness of a single solid squared cross-sectional support beam to withstand the full-scale force moments is calculated for Exp. 5 and Exp. 8, using the Eqn. (20), derived for the cross-sectional height h when $h = w$ and $\sigma = \sigma_{yield}$, assuming a steel with yield strength of $350\ \mathrm{MPa}$. The results from these calculations are shown in Eqn. (36) and Eqn. (37) for Exp. 5 and Exp. 8 respectively:

$$h = \sqrt[3]{\frac{|M| \cdot 6}{\sigma_{yield}}} = \sqrt[3]{\frac{1.99 \cdot 10^{8}\ \mathrm{Nm} \cdot 6}{350 \cdot 10^{6}\ \mathrm{Pa}}} = 1.51\ \mathrm{m} \tag{36}$$

$$h = \sqrt[3]{\frac{|M| \cdot 6}{\sigma_{yield}}} = \sqrt[3]{\frac{1.22 \cdot 10^{9}\ \mathrm{Nm} \cdot 6}{350 \cdot 10^{6}\ \mathrm{Pa}}} = 2.76\ \mathrm{m} \tag{37}$$

5.2.3. Discussing the results from the connected, reduced draft experiments

When analysing the normal curve fit for the presented experiments, the data shows a good fit for all experiments. With an RMSE ranging from $1.0 \cdot 10^{-3}\ (\mathrm{Nm})^{-1}$ to $7.0 \cdot 10^{-3}\ (\mathrm{Nm})^{-1}$ and a chi-squared ranging from $5.2 \cdot 10^{-5}\ (\mathrm{Nm})^{-1}$to $2.2 \cdot 10^{-3}\ (\mathrm{Nm})^{-1}$between the eight experiments, as shown in

Table 17 and Table 20, the statistical data from the curve fit may be assumed to be satisfactory accurate. When observing the curve fit from the plotted data in Figure 49 and Figure 51 the fit does look good for most of the experiments, however it can be observed that some of the histograms plotted have bins with a much higher probability close to zero then the rest of the data i.e., Exp. 3 and Exp. 4, but especially Exp. 7 and Exp. 8. This may be due to the system being exposed to a wave train which equalize and cancel out the motions for a short amount of time, as was observed during the experiments. From the observations of the figures, Exp. 5, Exp. 7 and Exp. 8 seems to have the least good fit. This correlates when comparing all the RMSE and chi-squared values.

For the 95% confidence interval boundaries, the results show that all the mean values and all the standard deviations found, lies within their respective intervals.

When comparing the 99.7% probability intervals from experiment 1-4, an increase in the loads are observed as shown in Table 18 and illustrated in Figure 53. From Exp. 1 to Exp. 2, where the wave period is increased from $0.77\ s$ to $1.0\ s$ respectively, the loads increases with a ratio of approximately $\lambda_{r_{1-2}} = 2.36$. From Exp. 2 to Exp. 3, where the wave period is increased from $1.0\ s$ to $1.24\ s$ respectively, the loads increases with a ratio of approximately $\lambda_{r_{2-3}} = 2.72$. When comparing Exp. 3 to Exp. 4, where the wave period is increased from $1.24\ s$ to $1.94\ s$ respectively, the loads increases with a ratio of approximately $\lambda_{r_{3-4}} = 1.20$.

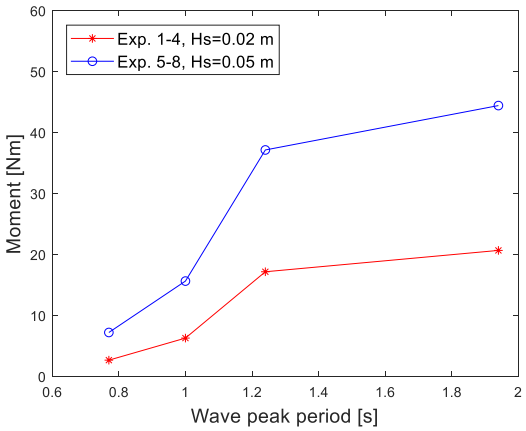

Figure 53 - Bending moments from the 99.7% probability interval plotted against wave period for the fully drafted experiments. As can be observed in the figure, the loads increase with the highest ratio when the peak period is increased from $T_P = 1.0\ s$ to $T_P = 1.24\ s$.

Similar observations are made for the experiment 5-8 comparison as shown in Table 21 and Figure 53. Also here the load ratio increases with approximately $\lambda_{r_{5-6}} = 2.21$, $\lambda_{r_{6-7}} = 2.37$ and $\lambda_{r_{7-8}} = 1.19$ between experiment 5-6, experiment 6-7, and experiment 7-8 respectively.

As in the fully drafted experiments, so does the loads in this case also increase fastest when the peak period is increased from 1.0 s to 1.24 s, and which correlates with the RAO's found for the connected

system for the reduced draft case as illustrated in Figure 33, which peaks at $t = 1.3\ \mathrm{s}$ for both the heave and pitch responses. It also correlates to the fact that the system in underdamped. The simplifications in the scaled FOWT design will however not matter in this case, as the coned part would be out of the water in a full-scale situation where the FOWT is at a reduced draft. This strengthen the proposed solution, where the system could be implemented with a structure to increase the damping.

When comparing the experiments with the same wave period, but different wave height the loads increases with a ratio of approximately $\lambda_{r_{1-5}} = 2.64$ between Exp. 1 and Exp. 5, $\lambda_{r_{2-6}} = 2.48$ between Exp. 2 and Exp. 6, $\lambda_{r_{3-7}} = 2.16$ between Exp. 3 and Exp. 7, and finally $\lambda_{r_{4-8}} = 2.15$ between Exp. 4 and Exp. 8. This indicates that, when the wave height is increased from $0.02\ \mathrm{m}$ to $0.05\ \mathrm{m}$, the loads increases more rapidly for the shorter peak periods compared with the longer.

It should be noted that during experiment 5-8, water was observed on the barge deck which may have damped the system's motions and hence, the measured loads from these experiments might be lower than they should be.

When the 99.7% probability intervals are scaled up to full-scale, the extremities of the bending moments range from approximately $7.43 \cdot 10^7\ \mathrm{Nm}$ to $1.22 \cdot 10^9\ \mathrm{Nm}$. These values are only meant as an indication of which loads might be expected by the full-scale constructions, due to the wave loads in the given sea-states. This is because the geometric similarity between the scaled FOWT and the full-scale structure is not completely obtained and that the viscous effects are scaled using the Froude scaling, which may give an incorrect viscous magnitude, as explained in chapter 2.1.

To get an indication of which size a support structure would need to be to withstand the bending stresses caused by the full-scale bending moments, a single solid square cross-sectional steel beam thickness was found for the extremities of the experiments. The thickness ranges from $1.08\ \mathrm{m}$ to $2.14\ \mathrm{m}$ between experiment 1-4 and $1.51\ \mathrm{m}$ to $2.76\ \mathrm{m}$ between experiment 5-8. This indicates that the needed thickness of the support structure is more exposed to the overall change in the peak period than to the change in wave height, which are both increased by a factor of approximately 2.5.

It should be noted that a full-size support structure would also need to compensate other environmental loads such as current and wind loads where, especially the latter, is assumed to contribute significantly to the bending moment, and even more so in the reduced draft case where more of the FOWT area is exposed to the wind.

5.2.4. Comparing and discussing the results from the fully drafted and reduced draft experiments

When comparing the two previous experiments up against each other, i.e., the experiments with the same wave period and the same wave height, a pattern is observed as shown in Table 23 and Figure 54. This shows that for Exp. 1 and Exp. 4, the reduced draft experiments measure a lower magnitude on the loads when compared with the fully drafted experiments. The reduction ratio is calculated to approximately $\lambda_{r_1} = 0.85$ and $\lambda_{r_4} = 0.78$ for Exp. 1 and Exp. 4 respectively. For Exp. 2 and Exp. 3 however, the results show the opposite. These experiments show a greater load magnitude for the reduced draft experiments compared with the fully drafted experiments. These experiments increase with a ratio of approximately $\lambda_{r_2} = 1.10$ and $\lambda_{r_3} = 1.16$ for Exp. 2 and Exp. 3 respectively.

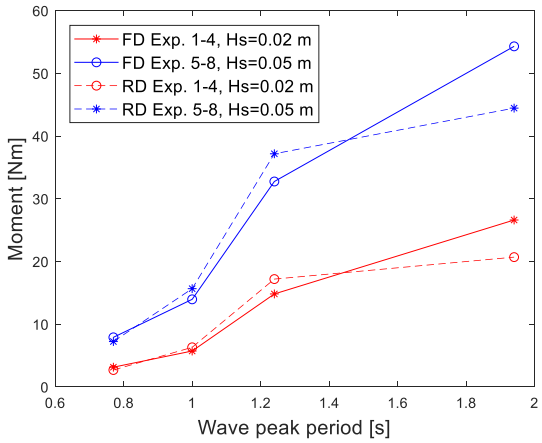

Figure 54 - Bending moments from the 99.7% probability interval plotted against wave period for the fully drafted (FD) and the reduced draft (RD) experiments. As can be observed in the figure, the loads are higher for the reduced draft experiments at $T_P = 0.77\ s$ and $T_P = 1.94\ s$, and higher for the fully drafted experiments at $T_P = 1.0\ s$ and $T_P = 1.24\ s$.

The pattern repeat itself for the experiments using the same wave period but a greater wave height, as illustrated in the figure. In this case Exp. 5 and Exp. 8 measures a lower load magnitude when comparing the reduced draft with the fully drafted experiments. The reduction ratio is calculated to approximately $\lambda_{r_5} = 0.90$ and $\lambda_{r_8} = 0.82$ for Exp. 5 and Exp. 8 respectively. Exp. 6 and Exp. 7 measures a greater load magnitude for the reduced draft experiments compared to the fully drafted experiments, with an increased ratio of $\lambda_{r_6} = 1.12$ and $\lambda_{r_7} = 1.14$ respectively.

These observations correlate well when comparing with the simulated RAO's found for the connected systems as illustrated in Figure 33. The figure shows that the for the reduced draft case the responses in heave and pitch have a greater magnitude from the wave periods between approximately $t = 0.5$ s to $t = 1.3$ s, and in wave periods between $t = 1.3\ s$ to approximately $t = 2.0$ s, the fully draft case responses are of greatest magnitude. Only in Exp. 1, where the magnitudes of the responses are slightly greater for the reduced draft case, does the simulated RAO's not correlate properly with the calculated

load ratios. It is assumed that if the draft is reduced further, the reduced draft case will measure larger loads than the fully drafted case. For the other cases, the simulated RAO's indicates a good fit with the measured loads.

Table 23 - Comparing the 99.7% probability intervals from the fully drafted and the reduced draft experiments.

Comparing the 99.7% probability load intervals from the fully drafted and the reduced draft experiments		
Experiment	**Fully Drafted interval [Nm]** $\mu \pm 3\sigma$	**Reduced Draft interval [Nm]** $\mu \pm 3\sigma$
Exp. 1 Hs=0.02 m, Tp=0.77 s	$[-3.13\,,3.15]$	$[-2.67\,,2.70]$
Exp. 2 Hs=0.02 m, Tp=1.0 s	$[-5.72\,,5.73]$	$[-6.32\,,6.32]$
Exp. 3 Hs=0.02 m, Tp=1.24 s	$[-14.83\,,14.79]$	$[-17.20\,,17.11]$
Exp. 4 Hs=0.02 m, Tp=1.94 s	$[-26.62\,,26.50]$	$[-20.70\,,20.60]$
Exp. 5 Hs=0.05 m, Tp=0.77 s	$[-7.91\,,7.88]$	$[-7.24\,,6.94]$
Exp. 6 Hs=0.05 m, Tp=1.0 s	$[-13.97\,,13.94]$	$[-15.67\,,15.64]$
Exp. 7 Hs=0.05 m, Tp=1.24 s	$[-32.76\,,32.47]$	$[-37.08\,,37.18]$
Exp. 8 Hs=0.05 m, Tp=1.94 s	$[-54.31\,,53.61]$	$[-44.46\,,44.20]$

5.3. Collision experiment

The results from the collision experiments where the scaled FOWT is released at different phases are presented here. This includes the experiments from experiment 9-11, all which uses regular sine waves with wave parameters as given in Table 8. All values presented before the results are discussed.

When analysing the results from the collision experiments, it is clear that the wave measurements from wave gauge 2, (see Figure 25 for reference) were exposed to reflecting waves by the models. This made the analysing process of the release phases more difficult than what was anticipated. Even so, the release phases were found however, they may not be completely accurate.

The analyses also clearly showed that there is a time lag between the upper load cell and the lower load cell with the latter being approximately 0.0205 seconds behind the former. Due to this the lower load cell data were adjusted 41 data points forwards, which equalized this time lag.

After the release is executed, the impact plate on the loadcell rig is exposed to friction as the scaled FOWT sometimes slides on it before it is completely released. This effect varies between the experiments with different release phases and might be due to a small amount of current still is left in the electromagnets after being turned off, so that the release is not completely constant.

5.3.1. Collision experiment 9

The measurements from the collision experiment 9, using regular waves with $H_S = 0.04$ m and $T_P = 0.77$ s, are calculated and plotted as shown in Figure 55 and Figure 56 for the release set at varying phases. The impact peaks are integrated over the impact time, as described in chapter 4.3.3., and the impulse loads are shown in the figures.

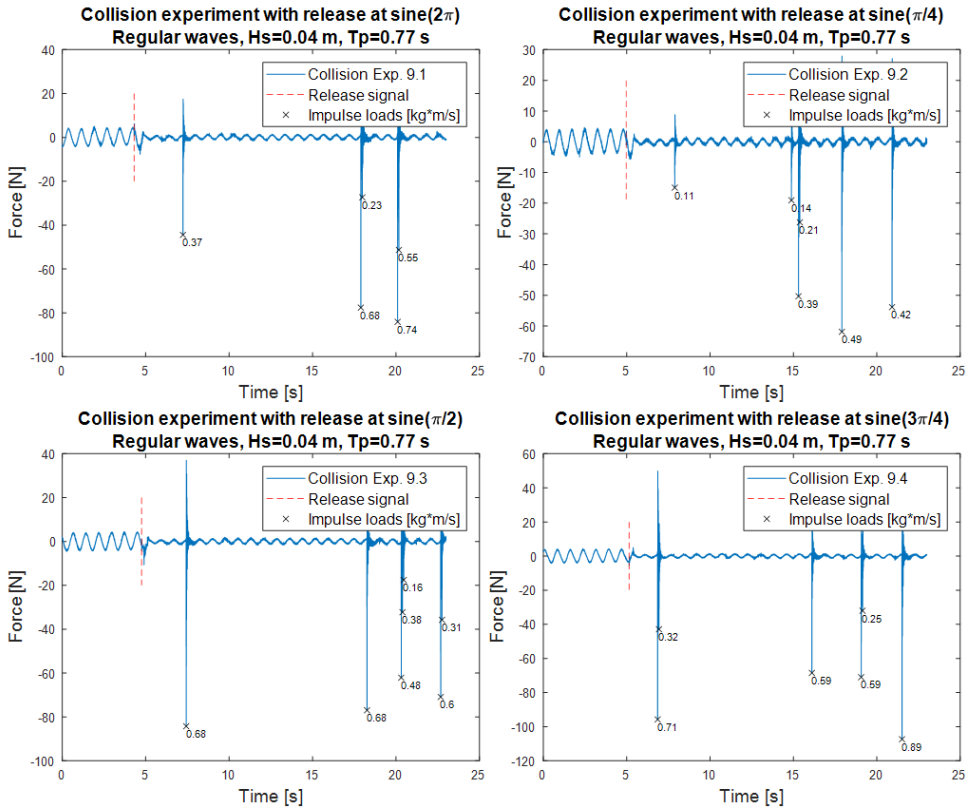

Figure 55 - Collision impacts between the scaled FOWT and the scaled barge for experiment 9 using regular sine waves with Hs=0.04 m *and Tp=0.77* s*. The release is set at varying phases with a 45-degree step. The impulse loads are found by integrating the impact force over the impact time.*

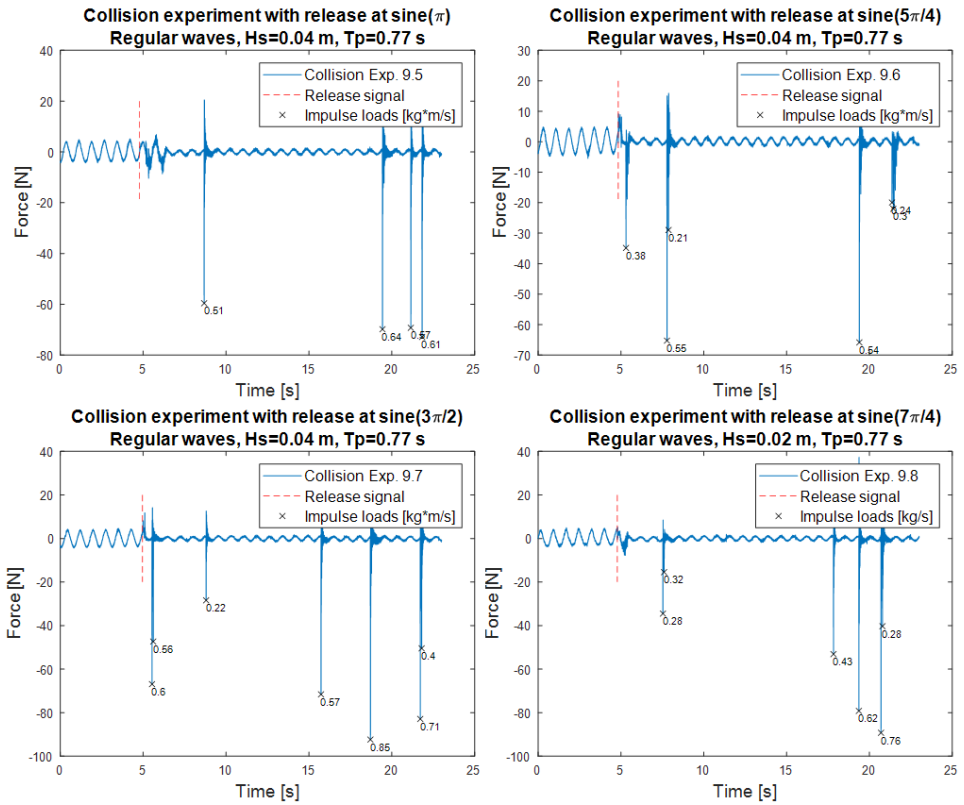

Figure 56 - Collision impacts between the scaled FOWT and the scaled barge for experiment 9 using regular sine waves with Hs=0.04 m *and Tp=0.77* s*. The release is set at varying phases with a 45-degree step. The impulse loads are found by integrating the impact force over the impact time.*

The impulse loads, and their respective impact times from the release, are presented in Table 24 for the experiments with the given release phases. The number of impacts varies from the different experiments as shown in the table.

Table 24 - The impulse loads with their respective impact times from the release at the given phase. Experiment 9.

Impulse loads and impact time from release Exp. 9								
Experiment no. Release phase	**No. 1** Impulse load $\left[\mathrm{kg}\frac{\mathrm{m}}{\mathrm{s}}\right]$ Impact Time [s]	**No. 2** Impulse load $\left[\mathrm{kg}\frac{\mathrm{m}}{\mathrm{s}}\right]$ Impact Time [s]	**No. 3** Impulse load $\left[\mathrm{kg}\frac{\mathrm{m}}{\mathrm{s}}\right]$ Impact Time [s]	**No. 4** Impulse load $\left[\mathrm{kg}\frac{\mathrm{m}}{\mathrm{s}}\right]$ Impact Time [s]	**No. 5** Impulse load $\left[\mathrm{kg}\frac{\mathrm{m}}{\mathrm{s}}\right]$ Impact Time [s]	**No. 6** Impulse load $\left[\mathrm{kg}\frac{\mathrm{m}}{\mathrm{s}}\right]$ Impact Time [s]	**No. 7** Impulse load $\left[\mathrm{kg}\frac{\mathrm{m}}{\mathrm{s}}\right]$ Impact Time [s]	**No. 8** Impulse load $\left[\mathrm{kg}\frac{\mathrm{m}}{\mathrm{s}}\right]$ Impact Time [s]
Exp. 9.1 sine(2π)	0.37 2.93	0.68 13.59	0.23 13.68	0.74 15.79	0.55 15.87	x x	x x	x x
Exp. 9.2 sine(π/4)	0.11 2.92	0.14 9.91	0.39 10.34	0.21 10.41	0.49 12.93	0.42 15.94	x x	x x
Exp. 9.3 sine(π/2)	0.68 2.67	0.68 13.51	0.48 15.56	0.38 15.63	0.16 15.71	0.60 17.92	0.31 18.00	x x
Exp. 9.4 sine(3π/4)	0.71 1.71	0.32 1.80	0.59 10.96	0.59 13.92	0.25 14.00	0.89 16.37	x x	x x
Exp. 9.5 sine(π)	0.51 3.91	0.64 14.66	0.57 16.38	0.61 17.05	x x	x x	x x	x x
Exp. 9.6 sine(5π/4)	0.38 0.47	0.55 2.94	0.21 3.04	0.54 14.55	0.24 16.53	0.30 16.61	x x	x x
Exp. 9.7 sine(3π/2)	0.60 0.57	0.56 0.65	0.22 3.84	0.57 10.77	0.85 13.75	0.71 16.76	0.40 16.84	x x
Exp. 9.8 sine(7π/4)	0.28 2.75	0.32 2.82	0.43 13.05	0.62 14.58	0.76 15.92	0.28 16.01	x x	x x

5.3.2. Discussing the results from collision experiment 9

The results from the collision experiment 9 shows that the impulse loads span from $I_{MIN} = 0.11\ \mathrm{kg \cdot m/s}$ to $I_{MAX} = 0.89\ \mathrm{kg \cdot m/s}$ due to the collision forces in the given sea-state and which occurs at Exp. 9.2 and Exp. 9.4 respectively. Exp. 9.4 is also exposed to the largest undisturbed impact, i.e., the largest impact without any disturbance up front, with an impulse load of approximately $I = 0.71\ \mathrm{kg \cdot m/s}$ and which occur at $t = 1.71\ \mathrm{s}$, as observed in Figure 55 and Table 24. This is the fourth largest impulse load in experiment 9.

The earliest impact after release occur in Exp. 9.6 at $t = 0.47\ \mathrm{s}$, and with an impulse load magnitude of $I = 0.38\ \mathrm{kg \cdot m/s}$, as shown in Table 24. The latest, first impact, after release occurs in Exp. 9.5 at $t = 3.91\ \mathrm{s}$, and with an impulse load magnitude of $I = 0.51\ \mathrm{kg \cdot m/s}$, as shown in Table 24. This may be the best release phase found in experiment 9, however, Exp. 9.5 shows that there is more friction between the models right after the release is set and when comparing with Exp. 9.6, this might also lead to an early first impact. Exp. 9.2 has an earlier first impact compared with Exp. 9.5, but as seen in the plots, it has a smaller magnitude in both impulse and force. Due to this, Exp. 9.2 is assumed to have the best release phase in experiment 9.

Even though the impacts from the different experiments differs in impulse magnitude and impact time, they do not seem to be completely random. A pattern is observed in the plots which shows one to two early impacts at first, then a longer period without impacts before two to three impacts follows in the end of the observed interval. Half of the experiments have their first impact in the time interval $t = 2.67\ \mathrm{s}$ to $t = 2.93\ \mathrm{s}$. There are mainly single and double collision impacts observed, however, there is one experiment which experience a triple impact as shown in Figure 55. This occurs at Exp. 9.3.

5.3.3. Collision experiment 10

The measurements from the collision experiment 10, using regular waves with $H_S = 0.04\ \mathrm{m}$ and $T_P = 1.0\ \mathrm{s}$, are calculated and plotted as shown in Figure 57 and Figure 58 for the release set at varying phases. The impact peaks are integrated over the impact time, as described in chapter 4.3.3., and the impulse loads are shown in the figures.

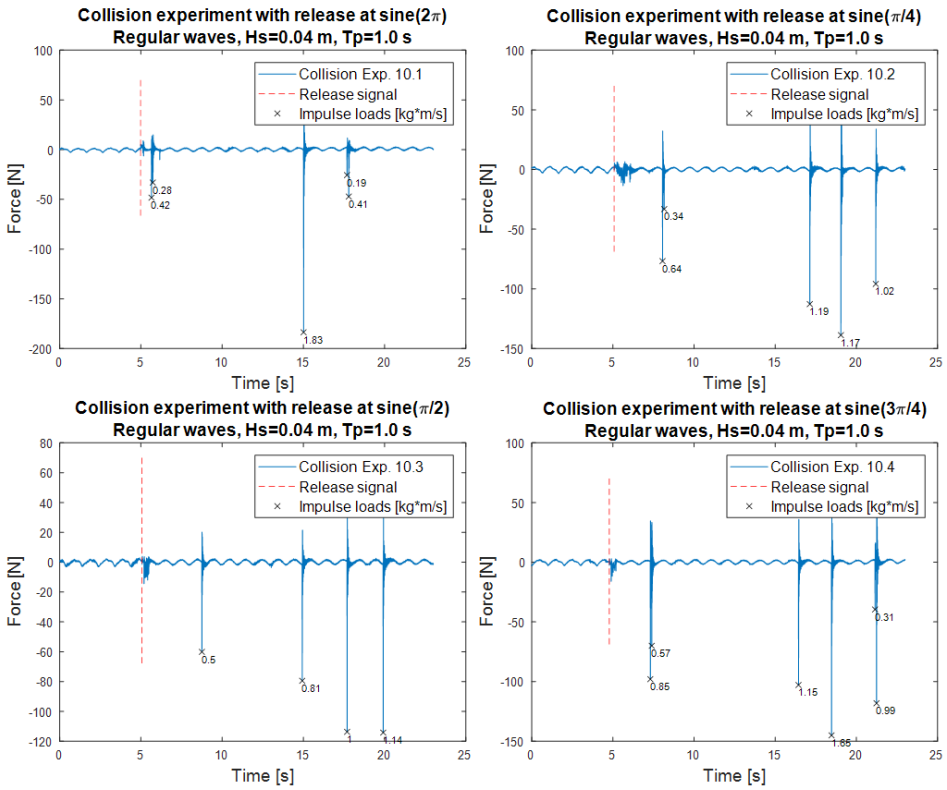

Figure 57 - Collision impacts between the scaled FOWT and the scaled barge for experiment 10 using regular sine waves with Hs=0.04 m *and Tp=1.0* s*. The release is set at varying phases with a 45-degree step. The impulse loads are found by integrating the impact force over the impact time.*

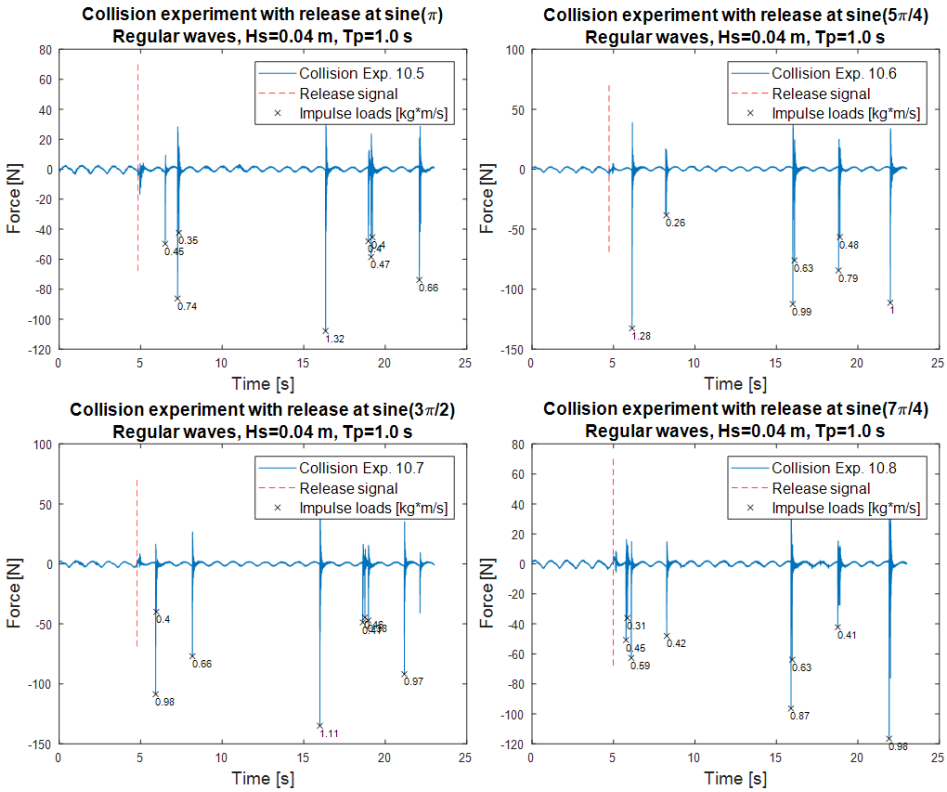

Figure 58 - Collision impacts between the scaled FOWT and the scaled barge for experiment 10 using regular sine waves with Hs=0.04 m *and Tp=1.0* s*. The release is set at varying phases with a 45-degree step. The impulse loads are found by integrating the impact force over the impact time. Exp. 10.7 plot have three overlapping impacts which are not easy to read in the figure. Their values are also shown in Table 25.*

The impulse loads, and their respective impact times from the release, are presented in Table 25 for the experiments with the given release phases. The number of impacts varies from the different experiments as shown in the table. As can be observed in Figure 58 with Exp. 10.7, not all peaks are registered.

Table 25 - The impulse loads with their respective impact times from the release at the given phase. Experiment 10.

Impulse loads and impact time from release Exp. 10								
Experiment no. Release phase	**No. 1** Impulse load $\left[\mathrm{kg}\frac{\mathrm{m}}{\mathrm{s}}\right]$ Impact Time [s]	**No. 2** Impulse load $\left[\mathrm{kg}\frac{\mathrm{m}}{\mathrm{s}}\right]$ Impact Time [s]	**No. 3** Impulse load $\left[\mathrm{kg}\frac{\mathrm{m}}{\mathrm{s}}\right]$ Impact Time [s]	**No. 4** Impulse load $\left[\mathrm{kg}\frac{\mathrm{m}}{\mathrm{s}}\right]$ Impact Time [s]	**No. 5** Impulse load $\left[\mathrm{kg}\frac{\mathrm{m}}{\mathrm{s}}\right]$ Impact Time [s]	**No. 6** Impulse load $\left[\mathrm{kg}\frac{\mathrm{m}}{\mathrm{s}}\right]$ Impact Time [s]	**No. 7** Impulse load $\left[\mathrm{kg}\frac{\mathrm{m}}{\mathrm{s}}\right]$ Impact Time [s]	**No. 8** Impulse load $\left[\mathrm{kg}\frac{\mathrm{m}}{\mathrm{s}}\right]$ Impact Time [s]
Exp. 10.1 sine(2π)	0.42 0.67	0.28 0.75	1.83 10.04	0.19 12.71	0.41 12.82	x x	x x	x x
Exp. 10.2 sine(π/4)	0.64 2.98	0.34 3.08	1.19 12.05	1.17 13.97	1.02 16.12	x x	x x	x x
Exp. 10.3 sine(π/2)	0.50 3.69	0.81 9.86	1.00 12.62	1.14 14.84	x x	x x	x x	x x
Exp. 10.4 sine(3π/4)	0.85 2.53	0.57 2.61	1.15 11.66	1.65 13.69	0.31 16.37	0.99 16.46	x x	x x
Exp. 10.5 sine(π)	0.45 1.68	0.74 2.44	0.35 2.52	1.32 11.51	0.40 14.13	0.47 14.30	0.40 14.38	0.66 17.26
Exp. 10.6 sine(5π/4)	1.28 1.41	0.26 3.52	0.99 11.28	0.63 11.38	0.79 14.08	0.48 14.16	1.00 17.26	x x
Exp. 10.7 sine(3π/2)	0.98 1.15	0.40 1.20	0.66 3.40	1.11 11.22	0.41 13.85	0.46 13.98	0.38 14.20	0.97 16.40
Exp. 10.8 sine(7π/4)	0.45 0.79	0.31 0.87	0.59 1.12	0.42 3.29	0.87 10.92	0.63 10.99	0.41 13.79	0.98 16.94

5.3.4. Discussing the results from collision experiment 10

The results from the collision experiment 10 shows that the impulse loads span from $I_{MIN} = 0.19\ \mathrm{kg} \cdot \mathrm{m/s}$ to $I_{MAX} = 1.83\ \mathrm{kg} \cdot \mathrm{m/s}$ due to the collision forces in the given sea-state. The minimum and maximum loads are both found in Exp. 10.1. Exp. 10.6 is exposed to the largest undisturbed impact with an impulse load of approximately $I = 1.28\ \mathrm{kg} \cdot \mathrm{m/s}$ and which occur at $t = 1.41\ \mathrm{s}$, as shown in Figure 58 and Table 25. This is the fourth largest impulse load observed in experiment 10.

The earliest impact after release occur in Exp. 10.1 at $t = 0.67\ \mathrm{s}$, and with an impulse load magnitude of $I = 0.42\ \mathrm{kg} \cdot \mathrm{m/s}$, as shown in Table 25. The latest, first impact after release, occurs in Exp. 10.3 at $t = 3.69\ \mathrm{s}$, and with an impulse load magnitude of $I = 0.50\ \mathrm{kg} \cdot \mathrm{m/s}$, as shown in Table 25. This may be the best release phase found in experiment 10, however, the earlier impacts in Exp. 10.1 are smaller both in impulse and force and hence, Exp. 10.1 is assumed be the better release phase.

As with experiment 9 so does experiment 10 show a similar pattern. This pattern shows one to two early impacts at first, then a longer period without impacts before two to three impacts follows in the end of the observed interval. Most impacts are single or double, however, also here there is some experiments which experience a triple impact as is observed in Figure 58.

5.3.5. Collision experiment 11

The measurements from the collision experiment 11, using regular waves with $H_S = 0.04$ m and $T_P = 1.24$ s, are calculated and plotted as shown in Figure 59 and Figure 60 for the release set at varying phases. The impact peaks are integrated over the impact time, as described in chapter 4.3.3., and the impulse loads are shown in the figures. Unfortunately, the data from Exp. 11.5 was lost and so this experiment is not included.

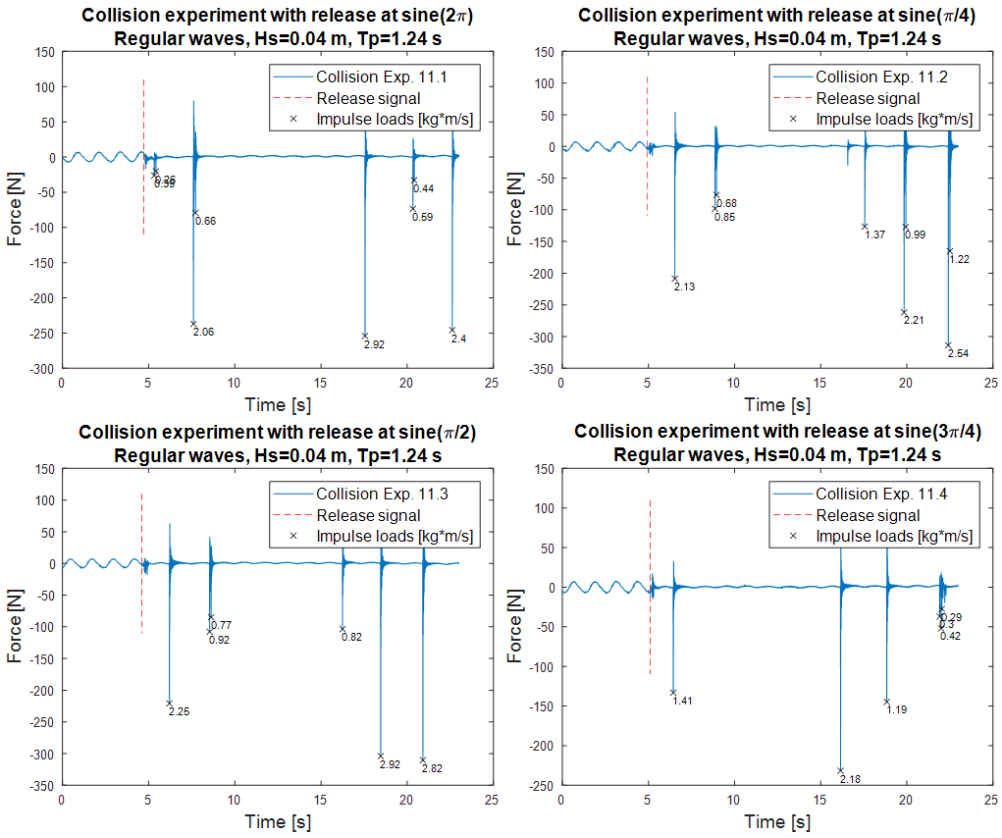

Figure 59 - Collision impacts between the scaled FOWT and the scaled barge for experiment 11 using regular sine waves with Hs=0.04 m *and Tp=1.24* s*. The release is set at varying phases with a 45-degree step. The impulse loads are found by integrating the impact force over the impact time. The Exp. 11.1 plot have two overlapping impacts which are not easy to read in the figure. Their values are also shown in Table 26.*

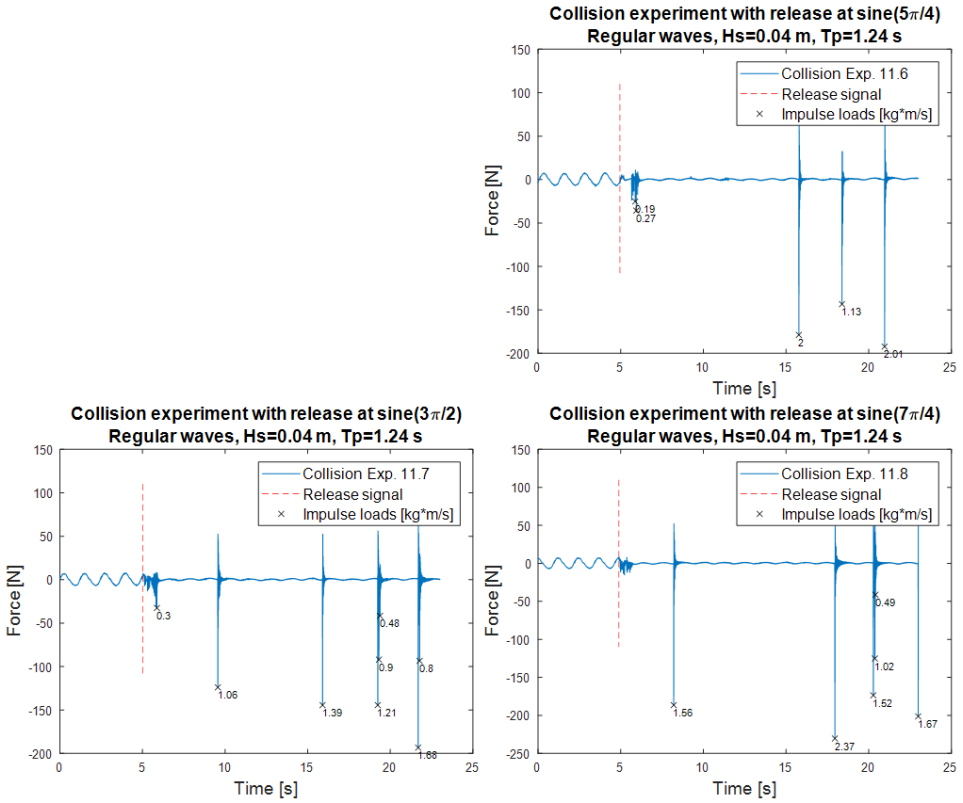

Figure 60 - Collision impacts between the scaled FOWT and the scaled barge for experiment 11 using regular sine waves with Hs=0.04 m *and Tp=1.24* s*. The release is set at varying phases with a 45-degree step. The impulse loads are found by integrating the impact force over the impact time. Unfortunately, the data from Exp. 11.5 was lost.*

The impulse loads, and their respective impact times from the release, are presented in Table 26 for the experiments with the given release phases. The number of impacts varies from the different experiments as shown in the table. As can be observed in Figure 59 with Exp. 11.2, not all peaks are registered.

Table 26 - The impulse loads with their respective impact times from the release at the given phase. Experiment 11.

Impulse loads and impact time from release Exp. 11								
Experiment no. Release phase	**No. 1** Impulse load $\left[\mathrm{kg}\frac{\mathrm{m}}{\mathrm{s}}\right]$ Impact Time [s]	**No. 2** Impulse load $\left[\mathrm{kg}\frac{\mathrm{m}}{\mathrm{s}}\right]$ Impact Time [s]	**No. 3** Impulse load $\left[\mathrm{kg}\frac{\mathrm{m}}{\mathrm{s}}\right]$ Impact Time [s]	**No. 4** Impulse load $\left[\mathrm{kg}\frac{\mathrm{m}}{\mathrm{s}}\right]$ Impact Time [s]	**No. 5** Impulse load $\left[\mathrm{kg}\frac{\mathrm{m}}{\mathrm{s}}\right]$ Impact Time [s]	**No. 6** Impulse load $\left[\mathrm{kg}\frac{\mathrm{m}}{\mathrm{s}}\right]$ Impact Time [s]	**No. 7** Impulse load $\left[\mathrm{kg}\frac{\mathrm{m}}{\mathrm{s}}\right]$ Impact Time [s]	**No. 8** Impulse load $\left[\mathrm{kg}\frac{\mathrm{m}}{\mathrm{s}}\right]$ Impact Time [s]
Exp. 11.1 sine(2π)	0.39 0.60	0.26 0.70	2.06 2.87	0.66 3.00	2.92 12.83	0.59 15.61	0.44 15.68	2.4 17.89
Exp. 11.2 sine(π/4)	2.13 1.61	0.85 3.95	0.68 4.03	1.37 12.64	2.21 14.92	0.99 15.02	2.54 17.49	1.22 17.58
Exp. 11.3 sine(π/2)	2.25 1.60	0.92 3.93	0.77 4.01	0.82 11.63	2.92 13.85	2.82 16.30	x x	x x
Exp. 11.4 sine(3π/4)	1.41 1.33	2.18 11.04	1.19 13.73	0.30 16.80	0.42 16.88	0.29 16.93	x x	x x
Exp. 11.5 sine(π)	x x	x x	x x	x x	x x	x x	x x	x x
Exp. 11.6 sine(5π/4)	0.19 0.92	0.27 0.98	2.00 10.82	1.13 13.42	2.01 16.00	x x	x x	x x
Exp. 11.7 sine(3π/2)	0.30 0.86	1.06 4.55	1.39 10.89	1.21 14.23	0.90 14.30	0.48 14.37	1.68 16.68	0.80 16.76
Exp. 11.8 sine(7π/4)	1.56 3.32	2.37 13.06	1.52 15.39	1.02 15.48	0.49 15.52	1.67 18.10	x x	x x

A repeatability test was also executed four times for experiment 11 with release at sine(π/2). The results from these tests are shown in Figure 61 and Table 27.

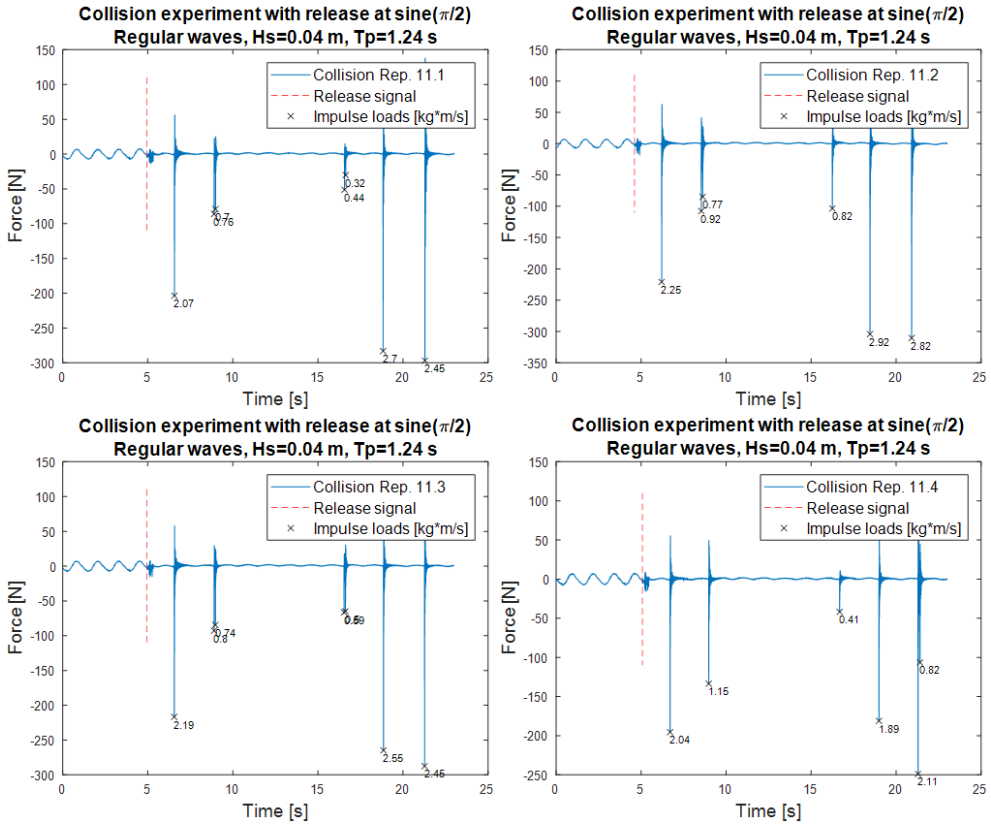

Figure 61 - Repeatability test of experiment 11 with release at sine(π/2). The plots clearly show a pattern in the impact times from release, however the number of impacts and impulse magnitude are slightly different between the experiments. The Rep. 11.1 and Rep. 11.3 plots have some overlapping impacts which are not easy to read in the figure. Their values are also shown in Table 27.

Table 27 - Repeatability test of experiment 11 with release at sine(π/2).

Impulse loads and impact time from release Exp. 11								
Experiment no. Release phase	**No. 1** Impulse load $\left[\mathrm{kg}\frac{\mathrm{m}}{\mathrm{s}}\right]$ Impact Time [s]	**No. 2** Impulse load $\left[\mathrm{kg}\frac{\mathrm{m}}{\mathrm{s}}\right]$ Impact Time [s]	**No. 3** Impulse load $\left[\mathrm{kg}\frac{\mathrm{m}}{\mathrm{s}}\right]$ Impact Time [s]	**No. 4** Impulse load $\left[\mathrm{kg}\frac{\mathrm{m}}{\mathrm{s}}\right]$ Impact Time [s]	**No. 5** Impulse load $\left[\mathrm{kg}\frac{\mathrm{m}}{\mathrm{s}}\right]$ Impact Time [s]	**No. 6** Impulse load $\left[\mathrm{kg}\frac{\mathrm{m}}{\mathrm{s}}\right]$ Impact Time [s]	**No. 7** Impulse load $\left[\mathrm{kg}\frac{\mathrm{m}}{\mathrm{s}}\right]$ Impact Time [s]	**No. 8** Impulse load $\left[\mathrm{kg}\frac{\mathrm{m}}{\mathrm{s}}\right]$ Impact Time [s]
Rep. 11.1 sine(π/2)	2.07 1.61	0.76 3.94	0.70 4.03	0.44 11.60	0.32 11.68	2.7 13.87	2.45 16.33	x x
Rep. 11.2 sine(π/2)	2.25 1.60	0.92 3.93	0.77 4.01	0.82 11.63	2.92 13.85	2.82 16.30	x x	x x
Rep. 11.3 sine(π/2)	2.19 1.60	0.80 3.94	0.74 4.02	0.59 11.58	0.50 11.66	2.55 13.90	2.45 16.31	x x
Rep. 11.4 sine(π/2)	2.04 1.63	1.15 3.90	0.41 11.60	1.89 13.91	2.11 16.21	0.82 16.32	x x	x x

The repeatability test indicates that if other experiments were tested multiple times, they would also show a similar similarity as shown above.

5.3.6. Discussing the results from collision experiment 11

The results from the collision experiment 11 shows that the impulse loads span from $I_{MIN} = 0.19\ \mathrm{kg \cdot m/s}$ to $I_{MAX} = 2.92\ \mathrm{kg \cdot m/s}$ due to the collision forces in the given sea-state. The minimum impulse load is found in Exp. 11.6, and the maximum impulse load are found both in Exp. 11.1 and Exp. 11.3. Exp. 11.3 is also exposed to the largest undisturbed impact with an impulse load of approximately $I = 2.25\ \mathrm{kg \cdot m/s}$ which occur at $t = 1.60\ \mathrm{s}$, as observed in Figure 59 and Table 26. This is the seventh largest impulse load in experiment 11.

The earliest impact after release occur in Exp. 11.1 at $t = 0.60\ \mathrm{s}$, and with an impulse load magnitude of $I = 0.39\ \mathrm{kg \cdot m/s}$, as shown in Table 26. The latest, first impact, after release occurs in Exp. 11.8 at $t = 3.32\ \mathrm{s}$, and with an impulse load magnitude of $I = 1.56\ \mathrm{kg \cdot m/s}$, as shown in Table 26. This may be the best release phase found in experiment 11, however, Exp. 11.6 also seems to be a better alternative as in this case there are two small impacts early after the release, before an approximately 10 seconds period until the next impact.

As with experiment 9 and experiment 10, so does experiment 11 show a similar pattern with one to two early impacts at first, then a longer period without impacts before two to three impacts follows in the end of the observed interval. Also here, most impacts are single or double, however, there are some experiments which experience a triple impact as is observed in Figure 59.

The repeatability test which was executed shows a clear pattern, as observed in Figure 61, and clearly indicates that the test can be performed multiple times with quite similar results. Even though some of the magnitude of the impulse loads are slightly different, there are also some that are quite similar. The number of impacts also differs slightly between each experiment, but still shows a good similarity.

From Table 27, when observing the repeatability test's impact times, there is a very good similarity between the different experiments and a pattern is clearly shown. The larges difference in impact time between corresponding impacts is 0.12 seconds, and which occurs between the experiments Rep. 11.1 and Rep. 11.4 with impact no. 7 and impact no. 5 respectively. The repeatability test indicates that if other experiments were tested multiple times, they would also show a similar similarity as with this case.

5.3.7. Comparing and discussing the maximum loads and the largest undisturbed impulse loads from collision experiment 9, 10 and 11.

When comparing the maximum impulse loads between the three experiments, the maximum loads increases with the increasing wave period. When the period is increased from 0.77 seconds to 1.0 seconds between experiment 9 and experiment 10 respectively, the maximum impulse loads increase

with a ratio of $\lambda_{9-10} = 2.06$. When the period is increased from 1.0 seconds to 1.24 seconds between experiment 10 and experiment 11 respectively, the maximum impulse loads increase with a ratio of $\lambda_{10-11} = 1.60$. When analyzing the maximum impulse loads from the plots, they show that they all occurs in the later part of the observed interval.

For the largest undisturbed impulse loads, these increases with a ratio of $\lambda_{9-10} = 1.80$ between experiment 9 and experiment 10, and $\lambda_{10-11} = 1.76$ between experiment 10 and experiment 11. These impacts occur at $t = 1.71$ s, $t = 1.41$ sand $t = 1.60$ s for experiment 9, 10 and 11 respectively. Even though these are from experiment with different release phases, they show a good similarity in time of occurrence.

In a real situation, the full-scale barge and FOWT, or their interfacing system, would need to be designed to withstand or compensate for the impact loads. From the experiments, the measured impact forces are quite large and their respective impact durations low. This is due to an elastic collision where no energy is lost to the deformation of the structures or no impact force is damped other than by the surrounding water.

The maximum impulse load and the larges undisturbed impulse load from experiment 9 are found from impacts with absolute force magnitudes of $F_{MAX} = 107.4$ N and $F = 95.8$ N with impact durations of $\tau_{MAX} = 0.015$ s and $\tau = 0.013$ s respectively. Scaling these values up to full-scale magnitudes, using the relevant Froude scaling relationship given in Table 1 gives $F_{F_{MAX}} = 4.11 \cdot 10^7$ N and $F_F = 3.67 \cdot 10^7$ N with impact durations of $\tau_{F_{MAX}} = 0.13$ s and $\tau_F = 0.11$ s respectively.

The maximum impulse load and the larges undisturbed impulse load from experiment 10 are found from impacts with absolute force magnitudes of $F_{MAX} = 183.7$ N and $F = 132.7$ N with impact durations of $\tau_{MAX} = 0.024$ s and $\tau = 0.022$ s respectively. Scaling these values up to full-scale magnitudes, using the relevant Froude scaling relationship given in Table 1 gives $F_{F_{MAX}} = 7.03 \cdot 10^7$ N and $F_F = 5.08 \cdot 10^7$ N with impact durations of $\tau_{F_{MAX}} = 0.20$ s and $\tau_F = 0.19$ s respectively.

The maximum impulse load and the larges undisturbed impulse load from experiment 11 are found from impacts with absolute force magnitudes of $F_{MAX_1} = 254.3$ N, $F_{MAX_2} = 304.2$ N and $F = 221$ N with impact durations of $\tau_{MAX_1} = 0.025$ s, $\tau_{MAX_2} = 0.021$ s and $\tau = 0.023$ s respectively. Scaling these values up to full-scale magnitudes, using the relevant Froude scaling relationship given in Table 1 gives $F_{F_{MAX_1}} = 9.73 \cdot 10^7$ N, $F_{F_{MAX_2}} = 1.16 \cdot 10^8$ N and $F_F = 8.46 \cdot 10^7$ N with impact durations of $\tau_{F_{MAX_1}} = 0.21$ s, $\tau_{F_{MAX_2}} = 0.18$ s and $\tau_F = 0.20$ s respectively.

The time interval which has been investigated is approximately 18 seconds after release, which would equal an approximately 153 seconds time interval in a full-scale case.

In [17], when no specified loads are given, the contact area exposed to a collision force may be designed assuming an impact force from a boat impact against a hard structure using Eqn. (23). In this case the calculation is done using the barge's displacement found in Table 3 as Δ', as shown in Eqn. (38):

$$F' = 2.5 \cdot \Delta' = 2.5 \cdot 1.295 \cdot 10^7 \text{ kg} \approx 3.24 \cdot 10^7 \text{ N} \quad (38)$$

It should be noted that the barge and the FOWT displacement is quite similar, hence, the design load when using the FOWT's displacement would only be slightly lesser than the design load calculated above.

When comparing the full-scale magnitudes with the magnitude calculated in Eqn. (38) it is clear that all the magnitudes from the measured maximum and undisturbed impacts exceeds this calculated impact force, with the loads from experiment 9 close by. A way of reducing the impact forces would be to increase the impact duration by using e.g. fenders to dampen the impact. The effects from a different impact duration is clearly shown in $F_{F_{MAX_1}}$ and $F_{F_{MAX_2}}$ which have the same impulse load, but a different impact duration where the latter is shorter and hence, the impact force approximately 20% larger.

When comparing the three experiments, the measured impact loads indicate that releases in waves with shorter wave periods gives smaller load magnitudes compared with release in waves with longer wave periods.

The upscaled values are only meant as an indication of which impact loads might be expected by the full-scale constructions, due to the wave loads in the given sea-states. This is because the geometric similarity between the scaled FOWT and the full-scale structure is not completely obtained and that the viscous effects are scaled using the Froude scaling, which may give an incorrect viscous magnitude, as explained in chapter 2.1.

It should be noted that, in a full-scale case, the collision impacts will also include the effects from wind and current loads, which are assumed to contribute significantly to the impact loads.

6. Conclusion

The objective of this thesis was to perform an experiment to measure the bending moments and collision loads between a model scaled floating offshore wind turbine and a barge, to investigate the feasibility of a method which purpose is to reduce the spar-buoy draft by using a barge to support and maintain the stability of the floating wind turbine during the installation. The following conclusions are made based on the results from the performed experiments in their given sea-states.

From the experiment where the scaled FOWT is connected to the barge in a fully drafted and a reduced draft case, the measurements shows rapidly increasing bending moments as the wave period is increased, and further as the wave height is increased. The largest increase in the bending moments occurs when the wave period is increased from 1.0 seconds to 1.24 seconds, which correlates with the simulated RAO's found for the connected systems. The ratio the loads increases with is largest for the lower wave periods. This is also the case when the wave height is increased, but the wave period is held the same, making the system highly exposed to rapidly increasing loads when the wave period and wave height increases from the lower region. The conclusion is made that the method is best fitted for operations in waves with wave periods up to 1.0 seconds, equal to a full-scale magnitude of approximately 8.5 seconds, (to set the maximum wave height, more experiments should be performed together with the collision tests in waves with wave heights between 0.02 and 0.04 meters). This constrain keeps the system in the region where the loads are manageable and before the RAO's exponential growth. However, safety measures need to be included to make the system able to withstand rapidly increasing loads if the wave peak and wave height increases. It is also advised to consider measures to reduce the underdamped systems motions by increasing the damping.

The collision experiments clearly show that collision will occur when using this setup. In the 18 second time interval observed after release, between 4 and 8 collisions were registered for each experiment. Calculations show that releases in waves with shorter wave periods gives smaller collision loads compared with release in waves with longer wave periods. There is no matching release phase agreeing as the best suited for all experiments, and so the best release phases are concluded to be sine($\pi/4$), sine(2π) and sine($5\pi/4$) for experiment 9, 10 and 11 respectively. The repeatability test proves that releases in the same phases will cause similar results. The number of impacts and their magnitude seems arbitrary throughout the experiments however, a pattern does seem to repeat itself concerning the impact's time of occurrence. When the maximum impulse loads and the largest undisturbed impulse loads were scaled up to full-scale magnitude, the magnitudes indicate that all the impact loads exceed what a full-size structure would be designed to withstand, with experiment 9 being close by. A damper or spring devise such as a fender could be included in the design to reduce

the impact force by increasing the impact time. However, the conclusion is made that in waves of this magnitude, the collision loads are too large to maintain the integrity of both the barge and the FOWT. It is advised that more experiments with lower wave heights are performed, to investigate if the magnitudes of the impact forces will decrease to a satisfying degree, before the method may be considered for approval.

7. Further work

In the experiments executed, more data were collected than what have been presented above. Of these data, further processing could give answer to more relevant questions regarding the presented method and the experiments executed.

Of these data, there is the data captured by the Qualisys motion capturing system, which could give more answers to which forces and accelerations the tower head mass is exposed to due to the wave loads. This could be used to compare the loads between the fully drafted and the reduced draft experiments, where the latter is assumed to see an increased acceleration as the tower head is higher up and hence, has larger motions than in the fully drafted case.

There is also more data captured by the wave gauges which could give interesting information about the wave reflections between the two bodies in the given sea-states. Further processing of these data could give a better understanding of the hydrodynamic interactions between a FOWT using a spar-buoy substructure, and a floating working platform.

Testing the same experiments with changed direction could also be interesting, to investigate if the loads would be reduced in both the connected and the collision cases, if the barge was set towards the waves and the FOWT in its wake. Further, tests with more turbines could be performed to investigate if, e.g., four FOWT would reduce the motions between the floating bodies compared with the performed experiments where only one FOWT was used.

Other interesting experiments which could be performed are experiments where the wind and current loads are investigated, and towing experiments to investigate which loads caused by vortex induced shredding may be expected between the floating bodies.

8. Error sources

In this chapter the error sources from the project are presented and discussed.

When the experiments were executed in MarinLab a few error sources may have affected the experiments to unknown degree. During the connected experiments 5-8, where a JONSWAP wave spectra with a wave height of 0.05 meters were used, water was observed on deck on the barge. This may have dampened the motions of the connected bodies, especially in pitch and heave, causing the measured loads to be lesser than what they really would be if this would not have occurred.

The slender tower section of the scaled FOWT may have been more flexible than intended and it was observed vibrating slightly during impacts in the collision experiments. This may have transformed some of the impact energy into vibrations and the load cells might have measured a lower force than what would be the case if the tower was rigid. The slender tower section may also have affected the measurements from the load cells during the connected experiments in a similar way.

The electromagnets were set to release the scaled FOWT at a specified moment, calculated to release in a given phase in the wave profile. Current still left in the coils may have prevented the release from being constant, causing a delay in the release even though a diode was attached to make sure the release happened as quickly as possible. After the two models were attached back together again, small adjustments in height may have given the next experiment a different precondition.

Due to complications with one of the original load cells, two different load cells were used. These two were produced from different manufactures, had a different connection options and had a different capacity, where one could measure twice the amount of the other. This may have caused the hysteresis effect to affect the measurements.

During the calibration of the load cells the loads were applied manually with the available tools. Small errors in the placement of the loads may have affected the calibration results.

During the different experiments, high frequency noise was observed, from time to time, in the plots. Even though these was smoothed in the MATLAB scripts, they might have affected the results slightly.

When building the models, glue, mortar, paint and bolts may have changed the weight distribution of the models. These effects were not included in the 3D-modelling of the models.

References

[1] IRENA, "Nuturing offshore wind markets: Good practices for international standardisation," International Renewable Energy Agency, Abu Dhabi.2018.

[2] IRENA, "Innovation Outlook: Offshore Wind," International Renewable Energy Agency, Abu Dhabi2016.

[3] IRENA, "Floating Foundations: a Game Changer for Offshore Wind Power," International Renewable Energy Agency, Abu Dhabi.2016.

[4] The Explorer. (accessed Apr. 02, 2019). *Harnessing offshore wind in deep waters*. Available: https://www.theexplorer.no/solutions/hywind--harnessing-offshore-wind-in-deep-waters/

[5] Atkins. (accsessed Feb. 5, 2019). *Hywind floating wind Installation Challange*. Available: http://www.atkinsglobal.com/en-GB/projects/hywind-installation-challenge

[6] A. Dewan, M. Asgarpour, and R. Savenije, "Commercial Proof of Innovative Offshore Wind Installation Concepts using ECN Install Tool," ECN Wind Energy.2015.

[7] Principle Power, "Principle renewable energy delivered, WindFloat.," ed.

[8] Equinor. (accesed May 16, 2018). *Photo archive*. Available: https://communicationtoolbox.equinor.com/mars/search_solr.searchobjects?p_com_id=12366&p_ptl_id=16659&p_oty_id=149860&p_lae_id=2&p_qcl_id=1

[9] J.M.J. Journèe and W.W. Massie, *Offshore Hydromechanics*. Delft University of Technology, 2001.

[10] K. Tabri, J. Määttänen, and J. Ranta, "Model-scale experiments of symetric ship collisions," *Journal of Marine Science and Technolog,* vol. 13, no. 1, pp. 71-84, 2008.

[11] *DNVGL-RP-C205 Environmental conditions and environmental loads*, 2017.

[12] A. F. Molland, *The Maritime Engineering Reference Book*. Butterworth-Heinemann, 2008.

[13] J. P. Bentley, *Principles of Measurement Systems*. Pearson Education Limited, 1983.

[14] M. J. Panik, *Statistical Interference*. Hoboken, New Jersey: John Wiley & Sons, Inc.,, 2012.

[15] J.R. Evans and D.L. Olson, *Statistics, Data Analysis, and Desition Modeling*. Pearson Education Limited, 2003.

[16] D.Gross, W. Hauger, J. Schröder, W.A. Wall, and J. Bonet, *Engineering Mechanics 2, Mechanics of Materials*. Germany: Springer-Verlag, 2018.

[17] *DNVGL-ST-0119 Floating wind turbine structures*, 2018.

[18] Western Norway University of Applied Sciences. (accesed Feb. 18, 2019). *MarinLab*. Available: https://www.hvl.no/en/about/marinlab/

[19] DNV-GL. (accessed Nov. 23, 2018). *Software Products Overview*. Available: https://www.dnvgl.com/software/products/sesam-products.html

[20] PTC. (accesed Mar. 24, 2019). *Creo Parametric 3D Modeling Software*. Available: https://www.ptc.com/en/products/cad/creo/parametric

[21] Edinburgh Designs. (accesed Mar. 24, 2019). *Wave Generating Software*. Available: http://www4.edesign.co.uk/product/wave-generating-software/

[22] Qualisys. (accessed Mar. 05, 2019). *We are Qualisys. The Swedish motion capture company.* Available: https://www.qualisys.com/about/

[23] National Instruments. (accesed Mar. 24, 2019). *What is LabVIEW*. Available: http://www.ni.com/cs-cz/shop/labview.html

[24] MathWorks, "MATLAB Primer," The MathWorks Inc, Ed., ed, 2015.

[25] V. Nedrevåg. (accessed Jan. 10, 2019). *Technip operasjonar ved Stord, Hywind Scotland Pilot Park*. Available: https://gammel.fylkesmannen.no/Documents/Dokument%20FMHO/Dokument%20milj%C3%B8%20og%20klima/H%C3%B8ringer/Hywind%20Statoil/Hywind%20-%20Operasjonar%20ved%20Stord.pdf

[26] Equinor. (accessed Jan. 15, 2019). *Hywind Scotland, The World's First Commercial Floating Wind Farm*. Available: https://www.equinor.com/en/news/worlds-first-floating-wind-farm-started-production.html

[27] Siemens. (2011, accessed Jan. 15, 2019). *Siemens 6.0 MW Offshore Wind Turbine*. Available: https://www.energy.siemens.com/br/pool/hq/power-generation/renewables/wind-power/6_MW_Brochure_Jan.2012.pdf

[28] Western Norway University of Applied Sciences. (accessed Apr. 11, 2019). *MAS 121 - Marintekniske Analyser høst 2018 - Prosjektoppgave*. Available: http://home.hib.no/ansatte/tct/ftp/H2018%20Marinteknisk%20Analyse/Oppgaver%20og%20info/Oppgave_H%C3%B8st_2018_rev3.pdf

[29] Equinor, "Hywind Buchan Deep Metocean Design Basis," 2014.